UNIVERSITA' DEGLI STUDI DI ROMA
Tor Vergata
Università

Facoltà di Scienze Matematiche Fisiche e Naturali
Dottorato di Ricerca in Fisica

XXIII ciclo

Giant polaronic effects in polymers: breakdown of the quasiparticle picture

Elena Cannuccia

A.A. 2009/2010

I supervisori	Il coordinatore
Dr. Andrea Marini *Prof. Rodolfo Del Sole*	*Prof. Piergiorgio Picozza*

Contents

Preface

The use of semiconductors in electronic devices has rapidly grown since the 50's. In order to understand the experimental results, a large theoretical effort has been devoted to calculate their electronic and optical properties.

Even if a considerable progress has been made in the field of *ab–initio* calculations of the electronic band structures, most of the standard approaches neglect a crucial ingredient: the effect of the lattice vibrations (i.e. electron–phonon interaction). Electrons and atomic vibrations are commonly decoupled and studied separately, implicitly assuming that the atoms are frozen in their crystallographic positions. This is the well known "adiabatic" or Born–Oppenheimer approximation and it represents a well established starting point to interpret experiments, that instead, are usually carried out at room temperature. Quoting Manuel Cardona[1] "...theorists often do not even bother to compare their calculations with available low temperature measurements, using instead more easily accessible room temperature spectra".

Actually even when $T \to 0\,K$ the one–particle and the two–particle electronic excitations spectra are affected by the zero point motion effect, connected to the quantum–mechanical nature of the atoms. This effect can induce a significant correction to the electronic states that questions the accuracy of the purely electronic theories.

The diamond band gap is a striking example. Diamond has a large Debye temperature ($\sim 1900\,K$). Nevertheless the gap renormalization induced by the electron-phonon interaction, as shown in Fig. 1, was estimated to be 370 meV in one of the first semiempirical calculations. If the zero point motion effect was properly taken into account the gap renormalization would reduce the discrepancy between the experimental value ($5.48\,eV$) and the calculated one[2] ($5.79\,eV$), to $0.06\,eV$.

In quasi one–dimensional materials with a Peierls ground state, like trans–

---

[1] M. Cardona, Solid State Commun. **133**, 3 (2005)

[2] M. Shishkin, M. Marsman, and G. Kresse, Phys. Rev. Lett. **99**, 246403 (2007)

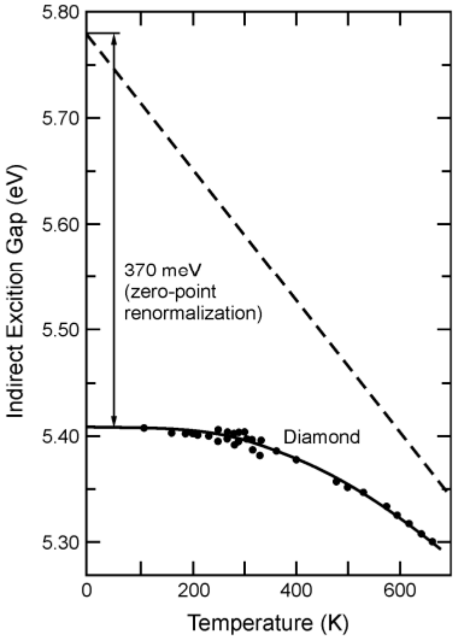

Figure 1: Optical gap of Diamond as a function of temperature.

polyacetylene, the zero–point motion is expected to be comparable with the lattice distortion. The resulting disorder causes the electronic properties, like the density of states, to deviate from those predicted for a rigid undistorted lattice. As a consequence the decoupling between the electronic and atomic degrees of freedom is bound to fail.

In this thesis I will study from first principles the effect of the electron-phonon interaction in polymers.

In Chapter 1 the theoretical tools to describe electrons are introduced: the Density Functional Theory (DFT) and the finite temperature many–body approach.

In Chapter 2 I will illustrate how DFT and the linear response theory of lattice vibrations combine into Density Functional Perturbation Theory (DFPT). Only by taking into account the mutual effects of the electronic correlation and atomic vibrations it is possible to obtain accurate phonon dispersions.

In Chapter 3 I will review the Heine Allen Cardona (HAC) approach to the electron-phonon coupling theory. It still represents a successful and predictive tool to study polaronic effects in an ab–initio manner. I will show how, in polymers, this approach leads to numerical instabilities, mainly due to the adiabatic approximation on which it is based. Then I will extend the HAC approach to a fully dynamical formulation within the many-body perturbation theory. The numerical oscillations of the HAC approach will be therefore connected to the existence of intense poles of the self-energy close to the bare electronic energies, that lead to a striking, as well as unexpected, breakdown of the quasiparticle picture.

In Chapter 4 the many-body formulation will be applied to polymers. Multiple structures will be shown to appear in the spectral functions even at $T = 0\,K$, revealing the key role played by the zero point motion effect. The physical interpretation of these structures will be connected to the existence of complicated polaronic states composed by coherent packets of electron/phonon states. The intrinsic, non perturbative, nature of these states will be disclosed by mapping the many-body problem to the solution of an eigenvalue problem. In this way, I will show how the spatial localization of electrons and atoms is deeply modified in the polaronic state. I will interpret the quasiparticle breakdown in terms of the spatial distribution of the electronic charges and in terms of the isotope effects.

The final picture will be of a coupled electronic and atomic dynamics well beyond the state–of–the–art picture. These results represent a potentially ground–breaking re–interpretation of the electronic dynamics in carbon based nanostructures.

Introduction to polymers: from plastics to optodevices

Natural polymers have been part of humans' life for centuries as natural rubbers for example, or in the cellulose as constituent of paper and wood.

With the growing up of plastic industry a large variety of synthetic polymers have been produced in order to meet the requirements coming from the everyday's life. Today, polymers are commonly used in thousands of products as plastics, elastomers, coatings, and adhesives, as well as children's toys and aircrafts.

The ability to synthesize polymers with a wide range of stiffness, strength, heat resistance, density goes together with an intense scientific research. However many new experimental applications of polymers are still entrusted to experimental evidences, laking of a robust theoretical support.

As far as three decades ago polymers were known and used for their attractive chemical, mechanical, and electrical properties, like *polyethylene*. In 1977 a fortuitous discovery shed light over the possibility to combine the flexibility and low weight of plastics with electric properties of metals. A new type of polymers, the conductive polymers, came in fact to the fore. The first example of conductive organic polymers was *trans-polyacetylene* (see Sec. 2.2) whose electrical conductivity can be tuned over a range of eleven orders of magnitude by iodine doping. H. Shirakawa, A.J. Heeger and A.G. Mc Diarmind were awarded the Nobel Prize in Chemistry in 2000 for this discoveries.

In order to conduct electricity, polymers must be *conjugated*. Polymers are 1D chains made up of repeated structural units linked by chemical covalent bonds. In *conjugated polymers* in particular, the chain is characterized by alternated single and double bonds between the carbon atom. Only the electrons of the double bonds contribute to the electrical conductivity, and their delocalization makes polymers suitable to transport charge. Recently polymers have also been employed as flexible substrates in the development of organic light-emitting diodes for electronic display.

The theoretical description of the conducting properties has been subject of an intense research activity. Especially the relation between electron-electron interaction and the electron-phonon interaction is still under investigation. The polymer chain can undergo local reorganization of the π-electron bonding in the vicinity of an additional charge. As a consequence the charge is trapped in a state that can be described as a soliton, for the particular case of *trans*-polyacetylene, and more generally as a polaron.

The prediction of the solitonic states by the Noble Prize laureate J.R. Schrieffer represents a first theoretical evidence for the strong coupling between the electronic and the atomic degrees of freedom.

Chapter 1

Particles and quasi particles at finite temperature

Electrons and nuclei are the fundamental particles that dictate the nature of the matter, in each of its forms: atoms, molecules or crystals. A typical physical system is constituted by a set of N electrons interacting by means of the Coulomb interaction. Furthermore each electron interacts with the ionic potential and the distribution of the atomic positions characterizes the configuration of the system. Most of the standard approaches, devised to study the electronic properties in the condensed matter field, relies on the assumption that the atomic vibrations only slightly alter the electronic properties. Electrons and atomic vibrations are decoupled and studied separately. This is the well known "adiabatic" or Born–Oppenheimer approximation.

A large theoretical effort is devoted to find accurate and robust methods to treat the electronic ground state. The aim is to provide universal methods that describe real systems in nature. By far the most widespread "first principles" approach designed to permit quantitative calculations of solids is Density Functional Theory (see Section 1.2). The solution of the Kohn–Sham equations of DFT yields a whole spectrum of single particle states. One would be tempted to identify the corresponding eigenvalues with excitation energies. Such an interpretation is not always correct: the Kohn–Sham wave functions and eigenvalues are only mathematical tools and cannot be endowed with a physical meaning. Nevertheless Kohn–Sham eigenvalues can be corrected using Green's functions techniques (see Sec. 1.3 and 1.4) within Many Body Perturbation Theory (MBPT).

By conjugating MBPT with DFT it is possible to devise a powerful first principles method to determine accurately quasi particle excitations in solids. The main ingredient of this approach is the electronic self–energy that contains all many–body exchange and correlation effects beyond the Hartree potential. The great advantage of the Green's functions approach is that it yields directly the most important physical properties of the system. As a consequence the Green's functions technique at *zero temperature* has been widely used to calculate physical quantities to be compared with the experiments even if they are actually carried out at *finite temperatures*.

Since the goal of many-body theory is to explain experiments and to predict them, the aim of this work is to extend the Green's functions technique to a more general framework, including an explicit dependence on temperature. This formalism, originated by Matsubara [1], will be extended and merged with DFT.

In this chapter I will introduce the basic theoretical tools devoted to the description of finite temperature effects on the electronic properties. The starting point of all results shown in this thesis is an accurate description of the electronic ground state. For this reason I will first review the Born–Oppenheimer approximation in Sec. 1.1, then Density Functional Theory in Sec. 1.2, followed by the formulation of the zero and the finite temperature Many Body Perturbation Theory in Secs. 1.3 and 1.4 respectively.

1.1 The Born–Oppenheimer Approximation

Any material, from a small molecule to a crystal is made up of a great number of interacting electrons and nuclei described by the Hamiltonian

$$\begin{aligned} H &= \sum_I -\frac{1}{2}\nabla_I^2 + \sum_i -\frac{1}{2}\nabla_i^2 + \frac{1}{2}\sum_{I\neq J}\frac{Z_I Z_J}{|\mathbf{R}_I-\mathbf{R}_J|} + \frac{1}{2}\sum_{i\neq j}\frac{1}{|\mathbf{r}_i-\mathbf{r}_j|} + \sum_{i,I}\frac{-Z_I}{|\mathbf{r}_i-\mathbf{R}_I|} \\ &= T_N(\mathbf{R}_I) + T_e(\mathbf{r}) + V_{I-I}(\mathbf{R}_I,\mathbf{R}_J) + V_{e-e}(\mathbf{r}_i,\mathbf{r}_j) + V_{e-I}(\mathbf{r},\mathbf{R}_I), \end{aligned} \tag{1.1}$$

where the indices *i,j* refer to the electrons, and the indices *I,J* to the nuclei. The terms appearing in Eq. (1.1) are respectively the kinetic energy of nuclei and electrons, the coulomb interactions between nuclei, between electrons and between nuclei and electrons.

The solution of the related Schrödinger equation is clearly impossible without introducing appropriate approximations. The first one used is based on the fact that electrons and ions have different masses. As a consequence the nuclear motion, in most materials is on a time scale much longer than typical electronic scales. The ionic and electronic degrees of freedom can be then decoupled and treated separately.

If the nuclear masses M_I, much larger than the electron mass m, were actually treated as infinite, the nuclear kinetic energy could be dropped and the nuclei could be thought as "fixed" in some assigned configuration $\{\mathbf{R}\}$. The atomic configuration provides the external potential $V_{e-I}(\mathbf{r},\{\mathbf{R}\})$ and determines the Schrödinger equation for the electrons

$$[T_e + V_{e-e} + V_{e-I}(\mathbf{r},\{\mathbf{R}\})]\,\psi_m(\mathbf{r},\{\mathbf{R}\}) = \epsilon_m(\{\mathbf{R}\})\psi_m(\mathbf{r},\{\mathbf{R}\}). \tag{1.2}$$

The electronic wavefunctions $\psi_m(\mathbf{r},\{\mathbf{R}\})$, as well as the eigenvalues $\epsilon_m(\{\mathbf{R}\})$, depend on the parameters $\{\mathbf{R}\}$; the suffix m summarizes the electronic quantum numbers. As the parameters $\{\mathbf{R}\}$ are varied, the eigenvalues $\epsilon_m(\{\mathbf{R}\})$ define the so called *Born–Oppenheimer surfaces.* Electrons, then, lay on energy surfaces whose minimum is in correspondence of the atomic equilibrium configuration $\{\mathbf{R}_0\}$.

After solving Eq. (1.2), for each fixed $\{\mathbf{R}\}$ the exact many-body wavefunction can be expanded

$$\Psi_n(\mathbf{r},\{\mathbf{R}\}) = \sum_{m=1}^{\infty} \chi_{nm}(\{\mathbf{R}\})\psi_m(\mathbf{r},\{\mathbf{R}\}). \tag{1.3}$$

We obtain a set of expansion coefficients χ_{nm} for each $\{\mathbf{R}\}$. We insert this completely general representation of $\Psi_n(\mathbf{r},\{\mathbf{R}\})$ in the full Schrödinger equation related to the Hamiltonian (1.1) to obtain

$$\begin{aligned}\textstyle\sum_m \psi_m(\mathbf{r},\{\mathbf{R}\})\,[T_N + V_{I-I}]\,\chi_{nm}(\{\mathbf{R}\}) + \sum_m \chi_{nm}(\{\mathbf{R}\})\,[T_N\psi_m(\mathbf{r},\{\mathbf{R}\})] +\\ +\textstyle\sum_m \chi_{nm}(\{\mathbf{R}\})\epsilon_m(\{\mathbf{R}\})\psi_m(\mathbf{r},\{\mathbf{R}\}) = E_n \sum_m \chi_{nm}(\{\mathbf{R}\})\psi_m(\mathbf{r},\{\mathbf{R}\}).\end{aligned} \tag{1.4}$$

If we multiply this equation by $\psi_k(\mathbf{r},\{\mathbf{R}\})$ and integrate over the electron coordinates $d\mathbf{r}$, and use the orthogonality of ψ_m, we arrive at

$$\begin{aligned}[T_N + V_{I-I} + \epsilon_k(\{\mathbf{R}\})] \quad \chi_{nk}(\{\mathbf{R}\}) + \sum_m \chi_{nm}(\{\mathbf{R}\})\langle\psi_k(\mathbf{r},\{\mathbf{R}\}) \mid T_N \mid \psi_m(\mathbf{r},\{\mathbf{R}\})\rangle\\ = E_n\chi_{nk}(\{\mathbf{R}\}).\end{aligned} \tag{1.5}$$

The result is a system of infinitely coupled equations. The Born–Oppenheimer approximation consists of neglecting the *off–diagonal* matrix elements $\langle\psi_k \mid T_N \mid \psi_m\rangle$. In this way the approximate equation is obtained

$$[T_N + V_{I-I} + \epsilon_k(\{\mathbf{R}\}) + \langle\psi_k \mid T_N \mid \psi_k\rangle]\,\chi_{nk}(\{\mathbf{R}\}) = E_n\chi_{nk}(\{\mathbf{R}\}), \tag{1.6}$$

where the electron eigenvalues ϵ_k and the matrix elements $\langle\psi_k \mid T_N \mid \psi_k\rangle$ act as a potential terms for the ionic motions. We can solve the Schrödinger equation (1.6) for the ionic motion and the electron Schrödinger equation (1.2) separately.

This is the Born–Oppenheimer approximation [2] that, by exploiting the mass difference between electrons and nuclei and consequently assuming that the neglected matrix elements are small, describes the interdependence between electronic and nuclear dynamics.

1.2 Density–Functional–Theory

The physics of an interacting electronic system perturbed by an external disturbance can be described writing the Hamiltonian like

$$H_{tot} = H + H_{ext}, \tag{1.7}$$

where H_{tot} is the total Hamiltonian and H_{ext} is an external perturbation.

Although the system is initially at rest, the evolved ground state under the action of the external disturbance acquires components over all the possible excited states of the system.

The calculation of these excited states is, however, a formidable task. Many different approaches are possible but all of them have to restore some reasonable approximations. In Section 1.3 I will introduce the Green's function concept where the excited states are linked to the spectral decomposition of the Green's function .

A completely different approach is devoted to the definition of the best single–particle potential able to reproduce the full spectra of excitations of the system. Clearly in this case everything is described in terms of Fock states, product of these "best" single–particle states. In the Hartree and Hartree–Fock approximations, the "best" single–particle potential is defined by means of a variational principle.

A similar approach is given by the Thomas–Fermi model [3], where the ground state energy is expressed in terms of the density alone. This could appear as a heuristic attempt to cut the chain of many–body correlations contained in the full interacting Hamiltonian.

Moreover the idea that the ground state properties of a quantum many–particle systems can be characterized solely in terms of the one–particle density is not obvious. The Thomas–Fermi model still remains a heuristic model, where the link between ground state energy and density is not formally justified.

In this framework the basic theorem of Hohenberg–Kohn has a fundamental importance. The original theorem states that an exact representation of the ground state properties of a stationary, non relativistic many–particle system in terms of the exact ground state density is possible. This is the basis of Density–Functional–Theory (DFT).

In the following I will describe this basic theorem for a rather simple case. A rigorous foundation of DFT has been extended to cover most of the situations of interest [3].

1.2.1 The Hohenberg–Kohn theorem

The standard approaches to the solution of a so intricate problem require to assume that the electronic problem can be decoupled from the atomic one. Atoms are generally assumed to be frozen in their crystallographic positions. As a consequence the electronic Hamiltonian contains a Coulomb part (the interaction between electrons) and a single–particle contribution (the kinetic energy and the interaction between electrons and nuclei).

The latter term is completely defined if the external potential $\hat{V}(\mathbf{r})$ is given

$$\hat{H} = \hat{T} + \hat{V} + \hat{H}_{coul}. \tag{1.8}$$

In second quantization Eq. (1.8) reads

$$\hat{H} = -\int d\mathbf{r}\,\psi^{\dagger}(\mathbf{r})\frac{\nabla^2}{2}\psi(\mathbf{r}) + \int d\mathbf{r}\,\psi^{\dagger}(\mathbf{r})\hat{V}(\mathbf{r})\psi(\mathbf{r}) + \hat{H}_{coul}. \tag{1.9}$$

To prove the Hohenberg–Kohn theorem [4] we will define a set $\mathcal{V}$ of local one–particle potentials defined in such a way that the solutions of each eigenvalue problem

$$\hat{H}|\Phi\rangle = \left(\hat{T} + \hat{V} + \hat{H}_{coul}\right)|\Phi\rangle = E|\Phi\rangle \quad V \in \mathcal{V}, \tag{1.10}$$

leads to a non–degenerate ground state for the N electrons system:

$$\hat{H}|\Psi\rangle = E_{gs}|\Psi\rangle. \tag{1.11}$$

Collecting the ground states in the set $\boldsymbol{\Psi}$ we have defined, via the solution of Schrödinger Eq. (1.11), a map

$$C : \mathcal{V} \rightarrow \boldsymbol{\Psi}. \tag{1.12}$$

This map is surjective by construction: $\boldsymbol{\Psi}$ contains no element which is not associated with some element of $\mathcal{V}$.

Next, for all ground state wavefunctions contained in $\boldsymbol{\Psi}$, we will calculate the ground state densities

$$n(\mathbf{r}) = \langle\Psi|\psi^{\dagger}(\mathbf{r})\psi(\mathbf{r})|\Psi\rangle, \tag{1.13}$$

establishing a second map:

$$D : \mathbf{\Psi} \rightarrow \mathcal{N}. \tag{1.14}$$

This map of the ground state wavefunctions on the set of ground state densities $\mathcal{N}$ is again surjective.

The Hohenberg–Kohn theorem, demonstrated in Ref. [4], is then: *the map C and D are also injective (one to one) and thus fully invertible.*

From the invertibility of maps C and D, three statements of Hohenberg–Kohn theorem follows:

(1^{st}): having established that a unique inversion of map D is possible

$$D^{-1} : n\left(\mathbf{r}\right) \rightarrow |\Psi\left[n\right]\rangle. \tag{1.15}$$

the first statement of Hohenberg–Kohn theorem can be formulated: *the ground state expectation value of any observable is a unique functional of the exact ground state density*

$$\langle\Psi\left[n\right]|\hat{O}|\Psi\left[n\right]\rangle = O\left[n\right], \tag{1.16}$$

The inverse map

$$\left(CD\right)^{-1} : n\left(\mathbf{r}\right) \rightarrow V\left(\mathbf{r}\right), \tag{1.17}$$

tells us that the knowledge of the ground state density determines the external potential of the system and thus, as the kinetic energy and the Coulomb interaction are specified, the entire Hamiltonian.

(2^{nd}): The Hohenberg–Kohn theorem establishes the variational character of the energy functional

$$E_{V_0}\left[n\right] \equiv \langle\Psi\left[n\right]|\hat{T} + \hat{V_0} + \hat{H}_{coul}|\Psi\left[n\right]\rangle, \tag{1.18}$$

where V_0 is the external potential of a specific system with ground state density $n_0\left(\mathbf{r}\right)$ and ground state energy E_0. The state $|\Psi\left[n\right]\rangle$ is generated from the elements of $\mathbf{N}$ via D^{-1}. $E_{V_0}\left[n\right]$ has the property

$$E_0 < E_{V_0}\left[n\right] \quad \text{for} \quad n \neq n_0, \tag{1.19}$$

and

$$E_0 = E_{V_0}\left[n_0\right]. \tag{1.20}$$

Thus the exact ground state density can be determined by minimization of the functional $E_{V_0}\left[n\right]$, in short

$$E_0 = \min_{n \in \mathcal{N}} E_{V_0}\left[n\right]. \tag{1.21}$$

(3^{rd}): The map D^{-1} does not depend on the potential V_0 of the particular system under consideration. Thus

$$E_{V_0}\left[n\right] = F_{HK}\left[n\right] + \int d\mathbf{r}\, V_0\left(\mathbf{r}\right) n\left(\mathbf{r}\right), \tag{1.22}$$

with

$$F_{HK}\left[n\right] = \langle \Psi\left[n\right] | \hat{T} + \hat{H}_{coul} | \Psi\left[n\right] \rangle. \tag{1.23}$$

The functional $F_{HK}\left[n\right]$ is *universal* in the sense that it does not depend on V_0.

The three statements of *invertibility, variational access* and *universality* constitute the classical formulation of the Hohenberg–Kohn theorem.

1.2.2 Kohn–Sham equations

The Hohenberg–Kohn theorem offers no practical guide to the explicit construction of the F_{HK} universal functional. For this purpose one still has to face the full intricacies of the many–body problem.

Although there are some energy functionals for Coulomb systems derived with the theory of the homogeneous electron gas or in other, more elaborated approaches, the situation cannot be considered satisfactory. Only thanks to the approach introduced by Kohn and Sham [5] it is possible to calculate the ground state properties of many–particles Coulomb systems with great accuracy.

Consider an auxiliary system of N non–interacting particles described by the Hamiltonian

$$\hat{H}_s = \hat{T} + \hat{V}_s, \tag{1.24}$$

According to the theorem of Hohenberg–Kohn, there exists a unique energy functional

$$E_s\left[n\right] = T_s\left[n\right] + \int d\mathbf{r}\, V_s\left(\mathbf{r}\right) n\left(\mathbf{r}\right), \tag{1.25}$$

for which the variational principle yields the exact ground state density $n_s(\mathbf{r})$ corresponding to $\hat{H}_s$. $T_s[n]$ denotes the universal kinetic energy functional of non–interacting particles.

The central assertion of the Kohn–Sham scheme is: *for any interacting system, there exists a local single–particle potential $V_s(\mathbf{r})$ such that the exact ground state density $n(\mathbf{r})$ of the interacting system equals the ground state density of the auxiliary problem,*

$$n(\mathbf{r}) = n_s(\mathbf{r}) . \tag{1.26}$$

Thus the ground state density $n(\mathbf{r})$ possesses a unique representation

$$n(\mathbf{r}) = \sum_{i=1\ldots N} |\phi_i(\mathbf{r})|^2 , \tag{1.27}$$

in terms of the lowest N single–particle orbitals obtained from the Schrödinger equation

$$\left[-\frac{\nabla^2}{2} + V_s(\mathbf{r})\right] \phi_i(\mathbf{r}) = \epsilon_i \phi_i(\mathbf{r}) . \tag{1.28}$$

Now consider a particular interacting system with external potential $V_0(\mathbf{r})$ and ground state density $n_0(\mathbf{r})$. To determine the auxiliary potential $V_{s,0}(\mathbf{r})$ which generates $n_0(\mathbf{r})$ via

$$n_0(\mathbf{r}) = \sum_{i=1\ldots N} |\phi_{i,0}(\mathbf{r})|^2 , \tag{1.29}$$

$$\left[-\frac{\nabla^2}{2} + V_{s,0}(\mathbf{r})\right] \phi_{i,0}(\mathbf{r}) = \epsilon_{i,0} \phi_{i,0}(\mathbf{r}) , \tag{1.30}$$

the exchange–correlation function $E_{xc}[n]$ is introduced as

$$E_{V_0}[n] = T_s[n] + \int d\mathbf{r}\, V_0(\mathbf{r})\, n(\mathbf{r}) + 1/2 \int d\mathbf{r} \int d\mathbf{r}'\, n(\mathbf{r})\, v(\mathbf{r},\mathbf{r}')\, n(\mathbf{r}') + E_{xc}[n] , \tag{1.31}$$

$$E_{xc}[n] = F_{HK}[n] - 1/2 \int d\mathbf{r} \int d\mathbf{r}'\, n(\mathbf{r})\, v(\mathbf{r},\mathbf{r}')\, n(\mathbf{r}') - T_s[n] ; \tag{1.32}$$

with $v(\mathbf{r},\mathbf{r}')$ the Coulomb interaction. Now the Hohenberg–Kohn variational principle ensures that $E_{V_0}[n]$ is stationary for small variations $\delta n(\mathbf{r})$ around the minimum density $n_0(\mathbf{r})$. If we define

$$V_{xc}([n_0],\mathbf{r}) = \left.\frac{\delta E_{xc}[n]}{\delta n(\mathbf{r})}\right|_{n_0} , \tag{1.33}$$

the assumption that the system is non–interacting representable (the KS ansatz) also for small deviations around the $[n_0(\mathbf{r}) + \delta n_0(\mathbf{r})]$ allows to write, by neglecting second order terms,

$$\delta T_s = -\int d\mathbf{r}\, V_{s,0}(\mathbf{r})\,\delta n(\mathbf{r})\,. \tag{1.34}$$

Thus one is left with the final expression

$$V_{s,0}(\mathbf{r}) = V_0(\mathbf{r}) + \int d\mathbf{r}'\, v(\mathbf{r},\mathbf{r}')\, n_0(\mathbf{r}') + V_{xc}([n_0],\mathbf{r})\,. \tag{1.35}$$

Eqs. (1.29–1.30) and the potential defined in Eq. (1.35) represents the classical Kohn–Sham scheme.

1.2.3 Local Density Approximation

In principle, the solution of the Kohn–Sham Eqs. (1.29–1.30) with the *exact* exchange–correlation potential, would give a set of fictitious single particle eigenstates whose density of states equals that one of the fully interacting system. Unluckily the exact exchange–correlation potential is not known and one has to find reasonable approximations for V_{xc}.

One of the most widely used is the *Local Density Approximation* (LDA). Introducing the exchange–correlation energy density $\epsilon_{xc}([n];\mathbf{r})$ as

$$E_{xc}[n] = \int d\mathbf{r}\, n(\mathbf{r})\,\epsilon_{xc}([n];\mathbf{r})\,, \tag{1.36}$$

in the LDA it is assumed that the system *locally* appears as an homogeneous electron gas. For the latter We split $\epsilon_{xc}([n];\mathbf{r})$ as composed of

$$\epsilon_{xc}^{hom}(n) = \epsilon_x^{hom}(n) + \epsilon_c^{hom}(n)\,, \tag{1.37}$$

with $\epsilon_x^{hom}(n)$ bare exchange and $\epsilon_c^{hom}(n)$ correlation energy density. While $\epsilon_x^{hom}(n)$ is an analytic function of n [6]

$$\epsilon_x^{hom}(n) = -\frac{3}{4}\left[\frac{3n}{\pi}\right]^{1/3}\,, \tag{1.38}$$

the correlation part can be calculated approximately using Many–Body perturbation theory [7] or via quantum Monte Carlo methods [8]. The first method gives an analytic function of n while the results from numerical Monte Carlo has been parametrized by, e.g., Perdew and Zunger [9].

1.3 The Zero Temperature Green's function approach

In the last section I have introduced a theoretical framework to describe a fully interacting system in terms of a free particles system.

Although these Kohn–Sham (KS) particles appear as fictitious quantities in the mathematical approach, they have allowed a successful starting point in the description of experimental photoemission data, as well as optical spectra [10]. Nevertheless the residual discrepancies between theory and experiment are due to the approximate inclusion of correlation effects and to the fact that DFT is a ground state theory.

A proper way of calculating single–particle excitation energies or quasi–particle energies is provided by the Green's functions technique. These functions describe the single–particle evolution governed by the full many body Hamiltonian. For this reason Green's functions include all correlation effects.

At zero temperature the one–particle Green's function is defined as

$$G(\mathbf{k}; t-t') = -i\langle \Psi_0 \mid \hat{T}\{c_{\mathbf{k}}(t)c^{\dagger}_{\mathbf{k}}(t')\} \mid \Psi_0\rangle, \tag{1.39}$$

where $\mid \Psi_0\rangle$ is the interacting ground state of the many-body system. As we do not know the exact eigenstates of the Hamiltonian, we write $H = H_0 + V$, where H_0 is the unperturbed part, and V is the interaction. We can solve exactly H_0, so we know its eigenstates. For simplicity we label these eigenstates with the wave vector **k** only. Although band indices are not considered their inclusion is straightforward.

In Eq. (1.39) $c_{\mathbf{k}}(t)$ and $c^{\dagger}_{\mathbf{k}}(t)$ are the operators in the Heisenberg picture which annihilate (create) at time t an electron on the state **k**. A generic operator in the Heisenberg picture is defined as

$$\mathcal{O}(t) = e^{itH}\mathcal{O}e^{-itH}, \tag{1.40}$$

while the wavefunction is independent of time. In Eq. (1.39) $\hat{T}$ is the time–ordering operator which orders c and $c^{\dagger}$ so that time decreases from left to right. For the two possible time orderings the Green's function reads

$$G(\mathbf{k}; t-t') = \begin{cases} -i\ \langle \Psi_0 \mid c_{\mathbf{k}}(t)c^{\dagger}_{\mathbf{k}}(t') \mid \Psi_0\rangle, & \text{if } t > t' \\ \ \ i\ \langle \Psi_0 \mid c^{\dagger}_{\mathbf{k}}(t')c_{\mathbf{k}}(t) \mid \Psi_0\rangle, & \text{if } t' > t \end{cases}. \tag{1.41}$$

An interchange of the position of two fermion operators causes a change of sign. The physical interpretation of the Green's function for $t > t'$ is the probability amplitude that an electron created on state $\mathbf{k}$ at time t' propagates to time t in the state $\mathbf{k}$. For $t' > t$ instead, it is the probability amplitude that a hole created on state $\mathbf{k}$ at time t propagates to time t' in the state $\mathbf{k}$. Since $\mathbf{k}$ is not usually eigenstates of H, the particle in the state $\mathbf{k}$ gets scattered, shifted in energy, etc., during the time interval $t - t'$. Thus by measuring at a later time t how much amplitude is left in the state $\mathbf{k}$, one can get information about the electron excitation. Similarly in the $t' > t$ time ordering an electron is destroyed from the ground state at time t. This destruction creates a vacancy, called a hole, and the hole can interact and scatter in the interval $t' - t$.

We want to convert the Green's function from the Heisenberg representation to the interaction representation, in which both the wavefunctions and the operators are time dependent. In order to do that we introduce an adiabatic "switching on" of the interaction

$$H = H_0 + e^{-\epsilon|t|}V, \tag{1.42}$$

in such a way a relationship between Ψ_0 at t=0 and the ground state of H_0, Φ_0, can be established:

$$\mid \Psi_0(0)\rangle = S(0, -\infty) \mid \Phi_0\rangle. \tag{1.43}$$

It means that in the past ($t = -\infty$) the ground state of the system was the unperturbed ground state Φ_0. The S matrix, brings the wavefunction adiabatically up to the present, at t=0. The result is a wavefunction, eigenstate of H and containing the effects of the interaction V.

Next we change the operators in the interaction picture:

$$\begin{aligned} c_{\mathbf{k}}(t) &= e^{itH}e^{-itH_0}\hat{c}_{\mathbf{k}}(t)e^{itH_0}e^{-itH} = U^{\dagger}(t)\,\hat{c}_{\mathbf{k}}(t)\,U(t) \\ &= S(0,t)\,\hat{c}_{\mathbf{k}}(t)\,S(t,0), \end{aligned} \tag{1.44}$$

where

$$\hat{c}_{\mathbf{k}}(t) = e^{itH_0}c_{\mathbf{k}}(t)e^{-itH_0}. \tag{1.45}$$

An analogous expression can be evaluated for the creation operator $\hat{c}^{\dagger}_{\mathbf{k}}(t)$. Using these definitions and invoking the S matrix properties, We get to the final expression for Green's function :

$$G(\mathbf{k}, t - t') = \frac{-i\langle\Phi_0 \mid \hat{T}\left\{\hat{c}_{\mathbf{k}}(t)\hat{c}^{\dagger}_{\mathbf{k}}(t')S(\infty, -\infty)\right\} \mid \Phi_0\rangle}{\langle\Phi_0 \mid S(\infty, -\infty) \mid \Phi_0\rangle}. \tag{1.46}$$

The operator $S(\infty, -\infty)$ contains an arbitrary number of operators which act in the three time intervals $(-\infty, t')$, (t', t) and (t, ∞). The $\hat{T}$ operator orders these operators in such a way all the time arguments decrease moving from left to right. When the interaction $V = 0$, the S matrix is the unity and G, Eq. (1.46) reduces to the unperturbed Green's function or free propagator

$$G^{(0)}(\mathbf{k}, t - t') = -i\langle\Phi_0 \mid \hat{T}\left\{\hat{c}_{\mathbf{k}}(t)\hat{c}^\dagger_{\mathbf{k}}(t')\right\} \mid \Phi_0\rangle. \tag{1.47}$$

In this case, the probability amplitude to find the particle in the state $\mathbf{k}$ at time t (or t') is given by

$$G^{(0)}(\mathbf{k}, t - t') = \begin{cases} -i\ \theta(\epsilon_{\mathbf{k}} - \epsilon_F)e^{i\epsilon_{\mathbf{k}}(t-t')}, & \text{if } t > t' \\ i\ \theta(\epsilon_F - \epsilon_{\mathbf{k}})e^{-i\epsilon_{\mathbf{k}}(t-t')}, & \text{if } t' > t \end{cases}, \tag{1.48}$$

which is the well known expression for the time evolution of a free electron.

We now want to explicitly evaluate the perturbed Green's function (Eq. (1.46)), inserting the expansion of the S matrix in powers of $\hat{V}$

$$S(\infty, -\infty) = 1 + \sum_{n=1}^{\infty} \frac{(-i)^n}{n!} \int_{-\infty}^{\infty} dt' \int_{-\infty}^{\infty} dt_1 ... \int_{-\infty}^{\infty} dt_n \hat{T}\left\{\hat{V}(t_1)\hat{V}(t_2)...\hat{V}(t_n)\right\}, \tag{1.49}$$

which contains time ordered products of the interaction $\hat{V}$.

By expanding the electron–electron interaction $\hat{V}$ in the basis of the H_0 eigenstates we get

$$\hat{V}(t) = \frac{1}{2} \sum_{\mathbf{k}_1, \mathbf{k}_2, \mathbf{q}} \frac{4\pi e^2}{\mathbf{q}^2} \hat{c}^\dagger_{\mathbf{k}_1+\mathbf{q}}(t)\hat{c}^\dagger_{\mathbf{k}_2+\mathbf{q}}(t)\hat{c}_{\mathbf{k}_2}(t)\hat{c}_{\mathbf{k}_1}(t). \tag{1.50}$$

The calculation of the n^{th} order Green's function requires the evaluation of time ordered brackets like

$$\langle\hat{T}\left\{\hat{c}_{\mathbf{k}}(t)\hat{V}(t_1)\hat{V}(t_2)...\hat{V}(t_n)\hat{c}_{\mathbf{k}}(t')\right\}\rangle. \tag{1.51}$$

Each n^{th} order term yields $n!$ contributions corresponding to all possible time orderings. Nevertheless many contributions vanish. For example

$$\langle\hat{T}\left\{\hat{c}_\alpha(t)\hat{c}^\dagger_\beta(t')\right\}\rangle, \tag{1.52}$$

equals zero unless $\alpha = \beta$, while

$$\langle\hat{T}\left\{\hat{c}_\alpha(t)\hat{c}^\dagger_\beta(t')\hat{c}_\gamma(t)\hat{c}^\dagger_\delta(t')\right\}\rangle, \tag{1.53}$$

equals zero unless $\alpha = \beta$ and $\gamma = \delta$ or unless $\alpha = \delta$ and $\beta = \lambda$. More generally the Wick's theorem [6] is the instrument to take care of the time ordering in a simple way. It expands a generic T–ordered product, Eq. (1.51), as a sum of completely contracted products of operators weighted by a factor phase $(-1)^P$. As a the single particle Green's function is defined as a contraction of two operators

$$\langle \hat{T}\left\{\hat{c}_{\mathbf{k}}(t)\hat{c}^{\dagger}_{\mathbf{k}}(t')\right\}\rangle \equiv iG^{(0)}(\mathbf{k};t-t'), \tag{1.54}$$

a completely contracted products of operators is such that all pairs of creation–annihilation operators have been contracted to form Green's functions . The number of permutation of the c and $c^{\dagger}$ operators needed to reach the final ordering defines the phase factor $(-1)^P$.

A few simple rules should be kept in mind when making the contractions. When two operators occur at the same time, the destruction operator always goes to the right, and the term is just the number operator which is independent of time. When instead two operators have different time arguments, we conventionally put the creation operator to the right (see Eq. 1.54), thus obtaining the unperturbed Green's function $iG^{(0)}(\mathbf{k};t-t')$.

We now consider the n=1 term in the S matrix expansion in Eq. (1.49), $G^{(1)}$

$$G^{(1)}(\mathbf{k};t-t') = -i\int_{-\infty}^{\infty} dt_1 \frac{\langle \Phi_0 \mid \hat{T}\left\{\hat{c}_{\mathbf{k}}(t)\hat{V}(t_1)\hat{c}^{\dagger}_{\mathbf{k}'}(t')\right\} \mid \Phi_0\rangle}{\langle \Phi_0 \mid S(\infty,-\infty) \mid \Phi_0\rangle}. \tag{1.55}$$

In this case the $\hat{T}$–product produces six possible fully contracted contributions. After having applied Wick's theorem we turn each contraction into either $G^{(0)}$ functions or number operators.

Feynman introduced the idea of representing the terms we get from the evaluation of the Green's function by drawings. The idea of Feynman's diagrams is to associate a line to each single particle Green's function corresponding to a contraction in the $\hat{T}$–product. A more detailed introduction to Feynman diagrams can be found, for example, in [6].

The diagrams are extremely useful to provide an insight into the physical process that these terms represent. These diagrams can be drawn both for the time dependent Green's function $G^{(0)}(\mathbf{k};t-t')$ as well as for the Fourier transformed Green's function $G^{(0)}(\mathbf{k};\omega)$. The diagrams obtained for the n=1 expansion of Green's function are depicted in Fig. 1.1.

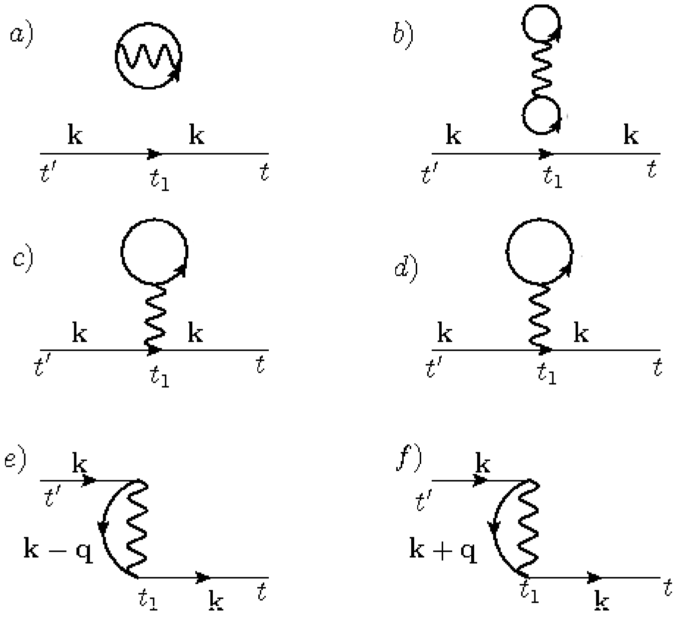

Figure 1.1: The six diagrams originated by the expansion of the perturbed Green's function at the first order in the electron–electron interaction.

The non connected diagrams (a and b) are cancelled out by the normalization factor appearing at the denominator of Eq. (1.55). They provide, in fact, just a constant which multiplies the contribution coming from the connected parts. Diagrams *c*), *e*) are equivalent to *d*), *f*) respectively, as they differ only in the variables labeling. But these are just the integration variables that can be interchanged.

The link between the n^{th} order Green's function and the Feynman's diagram can be performed following some general rules:

- Draw all topologically distinct connected diagrams with n interaction lines and 2n+1 directed Green's function .
- Each line represents a Green's function , $G^{(0)}(\mathbf{k}, t - t')$, running from t' to t.
- Label each line with a variable.
- Impose momentum conservation to each vertex.
- Each wavy line represents an unretarded Coulomb interaction.
- Integrate internal variables over all intermediate times.
- Multiply by an overall sign $(-1)^F$ where F is the number of Fermion loops.
- Assign a factor $(i)^n$ to each n^{th} order term.

- Green's function with equal time arguments should be interpreted as $G(\mathbf{k},t,t^+)$ where t^+ is infinitesimally ahead of t.

Taking the Fourier transform with respect to the time variable we get Green's function as a function of the energy:

$$G(\mathbf{k};\omega)=\int_{-\infty}^{\infty}d\,t\;\;e^{i\omega(t-t')}G(\mathbf{k};t-t'). \tag{1.56}$$

In the case of the unperturbed Green's function the time integral can be analytically performed to yield

$$G^{(0)}(\mathbf{k};\omega)=\frac{\theta(\mathbf{k}-\mathbf{k}_F)}{\omega-\epsilon_{\mathbf{k}}+i\delta}+\frac{\theta(\mathbf{k}_F-\mathbf{k})}{\omega-\epsilon_{\mathbf{k}}-i\delta}. \tag{1.57}$$

The free propagator has poles at energies $\omega=\epsilon_{\mathbf{k}}\mp i\delta$, where $\epsilon_{\mathbf{k}}$ is the energy of the particle added (or removed) to (from) the system depending on the sign of its imaginary part. In order to deal with well defined integrals, the free propagator (Eq. 1.48) is multiplied by the exponential $e^{-\delta(t-t')}$ (where δ is a positive infinitesimal).

We consider the 1^{st} order Green's function introduced above, whose diagrammatic expansion is depicted in Fig. 1.1. Translating diagrams *c*), *d*), *e*) and *f*) into functions using the rules introduced above we get

$$iG^{(1)}(\mathbf{k};t-t')=\int_{-\infty}^{\infty}dt_1\;\left[iG^{(0)}(\mathbf{k},t-t_1)\right](-i)\Sigma(\mathbf{k},t_1-t_1)\left[iG^{(0)}(\mathbf{k},t_1-t')\right]. \tag{1.58}$$

$\Sigma(\mathbf{k},t_1-t_1)$ represents a time–independent "effective potential" which the particle in the state $\mathbf{k}$ feels because of its interaction with all the other particles in the system. This 'effective potential' represents, at the 1^{st} order, the Hartree–Fock (HF) approximation, which is the lowest order approximation for the self-energy.

The full expansion of the propagator involves the evaluation of high–orders $\hat{T}$–products which produce a growing variety of diagrams. The series is usually evaluated approximately by selecting the most important types of terms and summing them to infinity. In the HF approximation the partial sum of diagrams is performed taking into account only *c*), *d*), *e*) and *f*) diagrams. The HF approximation neglects correlations, which means that it neglects the rearrangement of the other particles which "follow" the movement of the bare particle. The correlation would have the effect, for example, of "shielding" the interaction between quasi–particles. The proper evaluation of the screened interaction proceeds by the inclusion of polarization diagrams and it introduces a frequency dependent self-energy.

By using the diagrammatic analysis of the single particle Green's function expansion it is possible to derive a close and exact expression for the propagator

$$\begin{aligned} iG(\mathbf{k}; t-t') &= iG^{(0)}(\mathbf{k}; t-t') + \\ = \int_{-\infty}^{\infty}\int_{-\infty}^{\infty} dt_1\, dt_2\ & \left[iG^{(0)}(\mathbf{k}, t-t_2)\right](-i)\Sigma(\mathbf{k}, t_2-t_1)\left[iG^{(0)}(\mathbf{k}, t_1-t')\right], \end{aligned} \quad (1.59)$$

which is known as Dyson's equation. The Fourier transform of the series expansion allows to write it in an algebraic form

$$G(\mathbf{k},\omega) = G^{(0)}(\mathbf{k},\omega) + G^{(0)}(\mathbf{k},\omega)\Sigma(\mathbf{k},\omega)G(\mathbf{k},\omega). \quad (1.60)$$

In the diagrammatic representation Dyson's equation acquires the shape depicted in Fig. 1.2 where by the short notation Σ is meant all the proper (irreducible) self-energy parts.

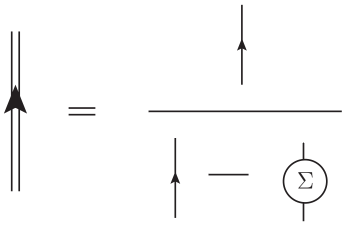

Figure 1.2: Diagrammatic representation of the Dyson's equation.

1.4 The Finite Temperature Green's function approach

As I discussed in the preface, most experiments are carried out at finite temperature. Consequently I need to extend the zero temperature formalism described in the previous section to the finite temperature regime. A many body system at finite temperature is defined as a statistical average over all its excited levels. Therefore the ground state average used to calculate the $T = 0\,K$ propagator (Eq. (1.39)), must be replaced by an average over a *grand canonical ensemble*,

$$G^T(\mathbf{k}, t-t') = -i\,\frac{Tr\ \rho\ \hat{T}\{c_{\mathbf{k}}(t)c^{\dagger}_{\mathbf{k}}(t')\}}{Z} \quad (1.61)$$

where $\rho = e^{-\beta(H-\mu N)}$ is the *grand distribution function*, μ is the chemical potential i.e. the energy required to remove one particle from the system. N is the number of particles, $\beta = 1/kT$ (k is the Boltzmann factor), and $Z = tr\{\rho\}$ is the *grand partition function*, T is the temperature of the system and $H = H_0 + V$, as in the $T = 0\,K$ case.

We now convert the Green's function (Eq. (1.61)) from the Heisenberg representation to the interaction one, using the S matrix and its properties

$$G^T(\mathbf{k}, t-t') = -\frac{1}{Z} Tr \left\{ \rho\, S(t)\, \hat{c}_{\mathbf{k}}(t)\, S(t,t')\, \hat{c}^{\dagger}_{\mathbf{k}}(t')\, S(t') \right\}. \tag{1.62}$$

The perturbation V enters in $e^{\pm iHt}$, which can be expanded using the S matrix. Notice that H also appears in the thermodynamic weighting factor $e^{-\beta H}$. If on one hand $S(t)$ satisfies the Schrödinger equation

$$\frac{\partial S(t)}{\partial t} = HS(t), \tag{1.63}$$

on the other ρ is the solution of the Bloch equation

$$\frac{\partial \rho}{\partial \beta} = -(H-\mu N)\rho, \tag{1.64}$$

as can be verified by differentiating $\rho = e^{-\beta(H-\mu N)}$. This analogy suggests that the *grand distribution function* should be also expanded in powers of the interaction as it was done for the S matrix. In order to treat both $S(t)$ and ρ in just only one S matrix expansion in terms of V, the trick is to treat t and β as the real and the imaginary parts of a complex variable. Time is treated as a complex temperature, rotating the time argument in the complex plane

$$it \to \tau, \quad \tau \in \Re, \tag{1.65}$$

τ has the time dimension. The imaginary time formalism is particularly useful when we want to perform perturbation theory as it introduces the finite temperature Feynman diagrams. This formalism leads us directly to physical results. Matsubara Green's function are, in fact, retarded correlation functions, that can be physically connected to measurable quantities.

Definition of the Matsubara Green's function

The *imaginary time Green's Function*, also called Matsubara Green's function, is defined in the following way

$$\mathcal{G}(\mathbf{k}, \tau_2, \tau_1) = -\frac{Tr\ \rho\ \hat{T}\{c_{\mathbf{k}}(\tau_2) c^{\dagger}_{\mathbf{k}}(\tau_1)\}}{Z}, \tag{1.66}$$

where the time ordering operator $\hat{T}$ orders operators according to the history, older times are arranged on the right. The i factor of Eq. (1.61) is dropped to agree with the convention in [6]. Analogously for real time we can define an imaginary time Heisenberg picture,

$$\mathcal{O}(\tau) = e^{\tau(H-\mu N)}\mathcal{O}e^{-\tau(H-\mu N)}. \tag{1.67}$$

Comparing Eq. (1.67) with the $T = 0\,K$ counterpart (Eq. (1.40)) we can summarize that in the finite temperature formalism

- it is replaced by a real time τ,
- H is substituted with $\rightarrow \bar{H} = H - \mu N$.

thus we can build up a finite temperature theory based on the Bloch equation in the same way the zero temperature theory was based on the Schrödinger equation. In particular it turns out that if these replacements are made in G, the resulting $\mathcal{G}$ can be expanded in a perturbation series which is nearly identical to the zero temperature case. Despite the introduction of an imaginary time, it is easy to get physical information out of $\mathcal{G}$. This is because the only effect of the $H \rightarrow H - \mu N$ replacement, is to shift the single particle energies by μ, since

$$H_0 - \mu N = \sum_k (\epsilon_k - \mu) c_k^\dagger c_k.$$

Starting from Eq. (1.66) we now analyze the imaginary time Green's function properties. First, $\mathcal{G}$ is a function of the time difference. It can be easily inferred for $\tau_2 > \tau_1$, using the theorem that the trace is unchanged by a cyclic variation of the operators,

$$\begin{aligned}
\mathcal{G}(\mathbf{k};\tau_2,\tau_1) &= -\frac{1}{Z} tr\left[\rho e^{\tau_2\bar{H}} c_{\mathbf{k}} e^{-\tau_2\bar{H}} e^{\tau_1\bar{H}} c_{\mathbf{k}}^\dagger e^{-\tau_1\bar{H}}\right] \\
&= -\frac{1}{Z} tr\left[\rho e^{\tau_2\bar{H}} e^{-\tau_1\bar{H}} c_{\mathbf{k}} e^{-\tau_2\bar{H}} e^{\tau_1\bar{H}} c_{\mathbf{k}}^\dagger\right] \\
&= -\frac{1}{Z} tr\left[\rho e^{(\tau_2-\tau_1)\bar{H}} c_{\mathbf{k}} e^{-(\tau_2-\tau_1)\bar{H}} c_{\mathbf{k}}^\dagger\right] \\
&= \mathcal{G}(\mathbf{k};\tau_2-\tau_1),
\end{aligned} \tag{1.68}$$

and likewise for $\tau_2 < \tau_1$. It enables us to drop one of the time variables since it is not unnecessary.

Second, the imaginary time Green's Function is a function of τ with domain

$$-\beta < \tau < \beta, \quad \tau = \tau_2 - \tau_1. \tag{1.69}$$

This is the interval over which $\mathcal{G}$ converges. This can be easily seen starting from Eq. (1.66) and considering first the case $\tau > 0$,

$$\mathcal{G}(\mathbf{k},\tau) = -\frac{1}{Z} tr\ \rho\ c_{\mathbf{k}}(\tau) c_{\mathbf{k}}^\dagger(0) = -\frac{1}{Z}\sum_i \langle \Psi_i \mid e^{-\beta\bar{H}} e^{\tau\bar{H}} c_{\mathbf{k}} e^{-\tau\bar{H}} c_{\mathbf{k}}^\dagger(0) \mid \Psi_i\rangle. \tag{1.70}$$

Now inserting a complete set $\sum_j \mid \Psi_j\rangle\langle\Psi_j \mid$ and defining $\bar{E}_i = E_i - \mu N_i$ we have

$$\mathcal{G}(\mathbf{k},\tau) = -\frac{1}{Z}\sum_{i,j} e^{-(\beta-\tau)\bar{E}_i}\langle\Psi_i \mid c_{\mathbf{k}} \mid \Psi_j\rangle e^{-\tau\bar{E}_j}\langle\Psi_j \mid c^{\dagger}_{\mathbf{k}} \mid \Psi_i\rangle. \tag{1.71}$$

The sum converges if the exponents are negative. Since $\bar{E}_i, \bar{E}_j$ can be arbitrarily large positive quantities, the exponents τ and $\beta-\tau$ must be positive. It means that $0 < \tau < \beta$. Analogously when $\tau < 0$, the condition $-\beta < \tau < 0$ follows.

The imaginary time propagator satisfies quasi–periodic boundary conditions. Applying the condition $tr(AB) = tr(BA)$ on Eq. (1.66) when $-\beta < \tau < 0$ we get:

$$\begin{aligned}
\mathcal{G}(\mathbf{k},\tau) &= \frac{1}{Z}tr\ \rho\ c^{\dagger}_{\mathbf{k}}(0)\ c_{\mathbf{k}}(\tau) \\
&= \frac{1}{Z}tr\ c_{\mathbf{k}}(\tau)\ \rho\ c^{\dagger}_{\mathbf{k}}(0) \\
&= \frac{1}{Z}tr\ e^{-\beta\bar{H}}\ \underbrace{e^{\beta\bar{H}}c_{\mathbf{k}}(\tau)e^{-\beta\bar{H}}}_{=c_{\mathbf{k}}(\tau+\beta)}\ c^{\dagger}_{\mathbf{k}}(0) \\
&= -\mathcal{G}(\mathbf{k},\tau+\beta),
\end{aligned} \tag{1.72}$$

and for $0 < \tau < \beta$ we get

$$\mathcal{G}(\mathbf{k},\tau) = -\mathcal{G}(\mathbf{k},\tau-\beta). \tag{1.73}$$

Fourier transform of the Matsubara Green's function

We previously observed that $\mathcal{G}(\mathbf{k},\tau)$ is defined over the interval $-\beta < \tau < \beta$. According to the theory of Fourier transformations, the Fourier expansion of a function defined over this interval is

$$\mathcal{G}(\mathbf{k},\omega_n) \equiv \frac{1}{2}\int_{-\beta}^{\beta} d\tau\ e^{i\omega_n\tau}\mathcal{G}(\mathbf{k},\tau), \tag{1.74}$$

where

$$\omega_n = \frac{\pi n}{\beta},\quad n = 0,\ \pm 1,\ \pm 2,\ \dots\ .$$

Now we introduce a function $\mathcal{G}_{per}(\mathbf{k},\tau)$ defined to be equal to $\mathcal{G}(\mathbf{k},\tau)$ on the interval $(-\beta,\beta)$ and then repeated on $(\beta,3\beta)$, $(3\beta,5\beta)$, ..., $(-3\beta,-\beta)$, ...

$$\mathcal{G}_{per}(\mathbf{k},\tau) = \frac{1}{\beta}\sum_{n=-\infty}^{+\infty} e^{-i\omega_n\tau}\mathcal{G}(\mathbf{k},\omega_n). \tag{1.75}$$

This trick eliminates the difficulty of defining the Fourier transform of $\mathcal{G}(\mathbf{k},\tau)$ on $(\mathbf{k},\omega)$ space. In order to do that $\mathcal{G}(\mathbf{k},\tau)$ is assumed to be defined over the whole interval $-\infty < \tau < \infty$.

In Eq. (1.74) a further simplification can be achieved by dividing the integral into its negative and positive regions, then applying quasi–periodic boundary conditions (Eq. (1.73)),

$$\begin{aligned}
\mathcal{G}(\mathbf{k},\omega_n) &= \frac{1}{2}\int_0^\beta d\tau\; e^{i\omega_n\tau}\mathcal{G}(\mathbf{k},\tau) + \frac{1}{2}\int_{-\beta}^0 d\tau\; e^{i\omega_n\tau}\mathcal{G}(\mathbf{k},\tau) \\
&= \frac{1}{2}\int_0^\beta d\tau\; e^{i\omega_n\tau}\mathcal{G}(\mathbf{k},\tau) + \frac{1}{2}e^{-i\omega_n\beta}\int_0^\beta d\tau\; e^{i\omega_n\tau}\underbrace{\mathcal{G}(\mathbf{k},\tau-\beta)}_{-\mathcal{G}(\mathbf{k},\tau)} \\
&= \frac{1}{2}(1-e^{-i\omega_n\beta})\int_0^\beta d\tau\; e^{i\omega_n\tau}\mathcal{G}(\mathbf{k},\tau).
\end{aligned} \tag{1.76}$$

$\mathcal{G}(\mathbf{k},\omega_n)$ vanishes when the factor $(1-e^{-i\omega_n\beta})$ is equal to zero. It happens for $\omega_n = \frac{n\pi}{\beta}$, whenever n is even. As a consequence the Fourier transform satisfies the following expression

$$\mathcal{G}(\mathbf{k},\omega_n) = \int_0^\beta d\tau\; e^{i\omega_n\tau}\mathcal{G}(\mathbf{k},\tau), \tag{1.77}$$

with ω_n as Matsubara frequencies

$$\omega_n = \frac{(2n+1)\pi}{\beta}, \quad n = 0,\ \ \pm 1,\ \ \pm 2,\ \ldots\ . \tag{1.78}$$

Note that the temperature is explicitly included in the ω_n frequencies through β.

The Matsubara Green's function for non interacting electrons

The Matsubara Green's functions can be easily evaluated in the case of a non-interacting system of particles. The Hamiltonian and its eigenstates are

$$H_0 = \sum_{\mathbf{k}} \epsilon_{\mathbf{k}} c^\dagger_{\mathbf{k}} c_{\mathbf{k}}, \qquad \mid \Phi_i\rangle = \mid n^i_1, n^i_2, ..., n^i_{\mathbf{k}}, ...\rangle. \tag{1.79}$$

Using Eq. (1.66) and the definition of the statistical factors f^+_k, f^-_k given in the Appendix A.5, the expression for the free propagator is given by

$$\mathcal{G}^{(0)}(\mathbf{k},\tau-\tau') = \begin{cases} -\ f^+_k\ e^{(\epsilon_{\mathbf{k}}-\mu)(\tau-\tau')}, & \text{if } \tau > \tau' \\ \quad f^-_k\ e^{-(\epsilon_{\mathbf{k}}-\mu)(\tau-\tau')}, & \text{if } \tau' > \tau \end{cases}, \tag{1.80}$$

Comparing this expression with the free propagator at zero temperature (Eq. 1.48), we observe that

- statistical factors appear instead of the θ–functions $\theta(\epsilon_{\mathbf{k}} - \epsilon_F)$ and $\theta(\epsilon_F - \epsilon_{\mathbf{k}})$,

- energies are shifted by μ,
- the *it* factor is replaced by τ.

Once $\mathcal{G}^{(0)}$ is periodically repeated by Eq. (1.75), the Fourier transform is obtained substituting Eq. (1.80) in Eq. (1.77), obtaining

$$\mathcal{G}^{(0)}(\mathbf{k},\omega_n) = \frac{1}{i\omega_n - \epsilon_{\mathbf{k}} + \mu}. \tag{1.81}$$

Because of the complex energy $i\omega_n$ appearing in the denominator $\mathcal{G}^{(0)}(\mathbf{k},\omega_n)$ and $\mathcal{G}(\mathbf{k},\omega_n)$ are also called *'imaginary frequency propagators'*. The temperature is still contained in this expression but now only in the imaginary frequency. I will show later how the occupation factors explicitly appear in the expressions when diagrams and correlation functions are actually evaluated.

Dyson's equation

The Matsubara Green's functions are evaluated by using the same Feynman diagram technique that was introduced in Sec. 1.3 in the case of zero temperature. Feynman diagrams rules are slightly modified to account for complex times and frequencies. The new definition of $\mathcal{G}$ through the Eq. (1.66) can be expanded in a perturbation series, equal to that one for G in the $T = 0\,K$, by following some simple rules

- Associate a Green's function $\mathcal{G}^{(0)}(\mathbf{k},\omega_n)$ to each internal electron line.
- Associate $V_{\mathbf{q}}$ to each internal coulomb line.
- Conserve momentum and complex frequency at each vertex. Keep in mind that fermion frequencies are odd integers $(2n+1)\pi/\beta$ and boson frequencies are even integers $2n\pi/\beta$. Their oddness and evenness will be maintained in the energy conservation.
- Sum over all internal variables.
- Multiply the expression by

  $$\frac{(-1)^{m+F}}{(\nu\beta)^m}, \tag{1.82}$$

  where F is the number of closed fermion loops. The integer m is the order of the diagram, as defined in Sec. 1.3.

A remarkable property of the finite temperature formalism is that the structure of the diagrams does not change compared to the $T = 0\,K$ case. The Dyson's equation, for example, has the same form

$$\mathcal{G}(\mathbf{k}, \omega_n) = \frac{1}{i\omega_n - \epsilon_{\mathbf{k}} + \mu - \Sigma(\mathbf{k}, \omega_n)}. \tag{1.83}$$

Similarly the equation of motion for higher orders Green's functions .

1.4.1 The free electron polarizability

In this paragraph the polarizability of free electrons at finite temperature will be evaluated. It is a simple example showing how the principle of the imaginary time formalism works. The Feynman diagram of the free polarizability is drawn in Fig. 1.3

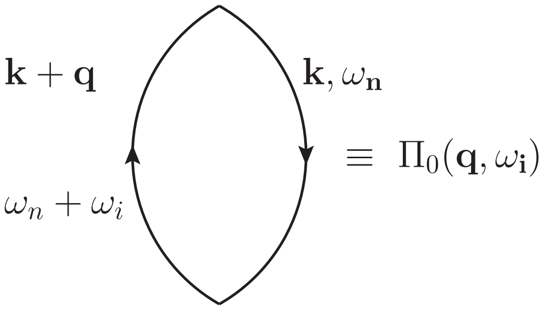

Figure 1.3: Polarizability diagram of non–interacting electrons.

By using the diagrammatic rules it is straightforward to show that $\Pi_0(\mathbf{q}, \omega_i)$ is given by the convolution of free imaginary Green's functions on the frequency axis

$$\begin{aligned}\Pi_0(\mathbf{q}, \omega_i) &= -2\int \frac{d\,\mathbf{k}}{(2\pi)^3}\frac{1}{\beta}\sum_{n=-\infty}^{+\infty} \mathcal{G}^{(0)}(\mathbf{k}, \omega_n)\mathcal{G}^{(0)}(\mathbf{k}+\mathbf{q}, \omega_n + \omega_i) \\ &= -2\int \frac{d\,\mathbf{k}}{(2\pi)^3}\frac{1}{\beta}\sum_{n=-\infty}^{+\infty} \frac{1}{i\omega_n - \epsilon_{\mathbf{k}} + \mu}\cdot\frac{1}{i\omega_n + i\omega_i - \epsilon_{\mathbf{k+q}} + \mu}. \end{aligned} \tag{1.84}$$

Usually, the use of Matsubara Green's functions leads to the appearance of sums over Matsubara frequencies, like in Eq. (1.84). The trick to evaluate those sums is to convert them into integrals and to apply the residuals theory. In order to do that, we just need a function having poles on the imaginary axis at frequencies $i\omega_n$. That function turns out to be the well known Fermi function distribution

$$f(\omega) = \frac{1}{e^{\beta\omega} + 1}, \tag{1.85}$$

with poles at the frequencies

$$\omega = i\frac{(2n+1)\pi}{\beta} = i\omega_n, \quad n = 0, \ \pm 1, \ \pm 2, \ \ldots \,. \tag{1.86}$$

The residue at one of these frequencies is, indeed

$$\mathrm{Res}\,[f(\omega)]\big|_{\omega=i\omega_n} = \lim_{\omega\to i\omega_n}(\omega - i\omega_n)f(\omega) = -\frac{1}{\beta}. \tag{1.87}$$

We consider now a contour $\mathcal{C}$ surrounding one of these poles. According to the theory of analytic functions we have that

$$\oint_{\mathcal{C}} d\omega\ F(\omega)f(\omega) = -\frac{2\pi i}{\beta}F(i\omega_n), \tag{1.88}$$

where $F(\omega)$ is a function without poles on the imaginary axis.

If the contour $\mathcal{C}$ is extended in order to define a region which encloses all poles laying on the imaginary axis (Fig. 1.4) where $F(\omega)$ is analytic, we can write

$$\oint_{\mathcal{C}} d\omega F(\omega)f(\omega) = -\frac{2\pi i}{\beta}\sum_{n=-\infty}^{+\infty} F(i\omega_n). \tag{1.89}$$

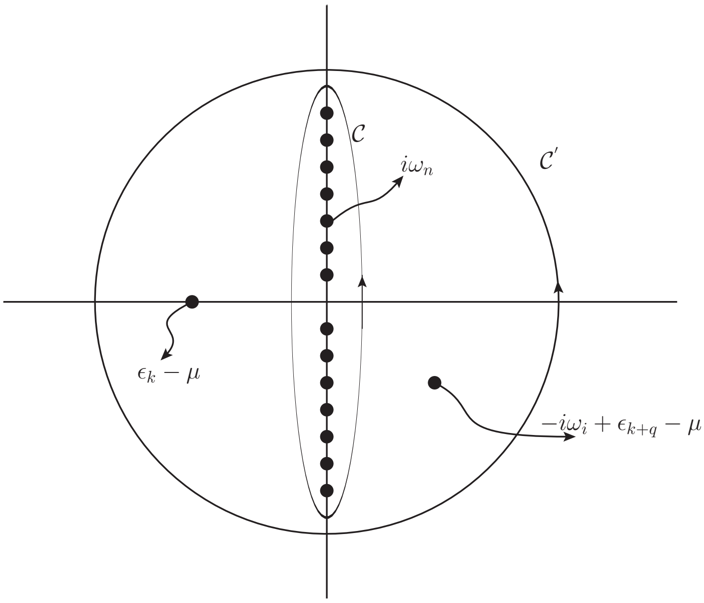

Figure 1.4: The contour used to perform the Matsubara sum for a function with known poles on the imaginary axis, $i\omega_n$.

If we take as $F(i\omega_n)$ the summand appearing in Eq. (1.84), the function $F(\omega)$ will be

$$F(\omega) = \frac{1}{\omega - \epsilon_{\mathbf{k}} + \mu}\cdot\frac{1}{\omega + i\omega_i - \epsilon_{\mathbf{k+q}} + \mu}. \tag{1.90}$$

Consider now an extended contour covering the entire complex plane $\mathcal{C}' : Re^{i\theta}$, where $R \to \infty$, see Fig. 1.4. This contour would give us the contributions coming from poles of $f(\omega)$, Eq. (1.86), and from poles of $F(\omega)$: $\omega = \epsilon_{\mathbf{k}} - \mu$ and $\omega = \epsilon_{\mathbf{k+q}} -$

$\mu - i\omega_i$. Furthermore the contour integral itself gives zero because the integrand goes to zero exponentially as $\omega \in \mathcal{C}'$. Therefore

$$\begin{aligned} \oint_{\mathcal{C}'} d\omega F(\omega) f(\omega) &= 0 \\ &= \frac{2\pi i}{-\beta} \sum_{n=-\infty}^{+\infty} F(i\omega_n) + \\ &+ 2\pi i \sum \text{Residues of } F(\omega) f(\omega)\Big|_{\omega=\text{“poles of } F(\omega)\text{”}} . \end{aligned} \tag{1.91}$$

This means that

$$\begin{aligned} \frac{1}{\beta} \sum_{n=-\infty}^{+\infty} F(i\omega_n) &= \sum \text{Residues of } F(\omega) f(\omega)\Big|_{\omega=\text{“poles of } F(\omega)\text{”}} \\ &= \left[\frac{f(\epsilon_{\mathbf{k}} - \mu)}{\epsilon_{\mathbf{k}} + i\omega_i - \epsilon_{\mathbf{k+q}}} + \frac{f(\epsilon_{\mathbf{k+q}} - \mu - i\omega_i)}{\epsilon_{\mathbf{k+q}} - i\omega_i - \epsilon_{\mathbf{k}}} \right] . \end{aligned} \tag{1.92}$$

Note that $\omega_n + \omega_i = (n+i)\frac{\pi}{\beta}$, with $n+i$ odd. Therefore $\omega_i = i\frac{\pi}{\beta}$, with index i even. As a consequence

$$f(\epsilon_{\mathbf{k+q}} - \mu - i\omega_i) = f(\epsilon_{\mathbf{k+q}} - \mu). \tag{1.93}$$

Putting together Eq. (1.92) and Eq. (1.84) we have

$$\Pi_0(\mathbf{q}, \omega_i) = -2 \int \frac{d\,\mathbf{k}}{(2\pi)^3} \left[\frac{f(\epsilon_{\mathbf{k}} - \mu)}{\epsilon_{\mathbf{k}} + i\omega_i - \epsilon_{\mathbf{k+q}}} + \frac{f(\epsilon_{\mathbf{k+q}} - \mu)}{\epsilon_{\mathbf{k+q}} - i\omega_i - \epsilon_{\mathbf{k}}} \right] . \tag{1.94}$$

Now we add and subtract $f_{\mathbf{k+q}} f_{\mathbf{k}}$ (using the simplified notation $f_{\mathbf{k}} = f(\epsilon_{\mathbf{k}} - \mu)$)

$$\Pi_0(\mathbf{q}, \omega_i) = 2 \int \frac{d\,\mathbf{k}}{(2\pi)^3} \left[\frac{f_{\mathbf{k+q}}(1 - f_{\mathbf{k}}) - f_{\mathbf{k}}(1 - f_{\mathbf{k+q}})}{i\omega_i + \epsilon_{\mathbf{k}} - \epsilon_{\mathbf{k+q}}} \right] . \tag{1.95}$$

Let's change $\mathbf{k} + \mathbf{q} \to -\mathbf{k}$ in the first term of the sum in the square brackets. This substitution implies $\epsilon_{-\mathbf{k}} = \epsilon_{\mathbf{k}}$ and that $f_{-\mathbf{k}} = f_{\mathbf{k}}$, so we get

$$\Pi_0(\mathbf{q}, \omega_i) = 2 \int \frac{d\,\mathbf{k}}{(2\pi)^3} f_{\mathbf{k}}(1 - f_{\mathbf{k+q}}) \left[\frac{1}{i\omega_i + \epsilon_{\mathbf{k+q}} - \epsilon_{\mathbf{k}}} - \frac{1}{i\omega_i + \epsilon_{\mathbf{k}} - \epsilon_{\mathbf{k+q}}} \right] . \tag{1.96}$$

This is the *'imaginary frequency pair bubble'*.

Since the experiments are done at real frequencies, we need to perform an analytic continuation [11] in order to calculate theoretical physical quantities to compare with finite–temperature experiments. In order to move on the real axis we need to replace

$$i\omega_i \to \omega + i\delta, \tag{1.97}$$

in the first term in the square brackets of Eq. (1.96), with δ an infinitesimal positive quantity. Similarly we need to replace

$$i\omega_i \to \omega - i\delta, \tag{1.98}$$

in the second term in the square brackets of Eq. (1.96). The result is a finite temperature polarization function written on the real axis, $\Pi_0^T(\mathbf{q},\omega)$

$$\Pi_0^T(\mathbf{q},\omega) = f^+(\omega)\Pi_0(\mathbf{q},\omega+i\delta) + f^-(\omega)\Pi_0(\mathbf{q},\omega-i\delta). \tag{1.99}$$

In the limit of $T \to 0$ we should find the expression of $T = 0\,K$ pair bubble. That's just what happens

$$\begin{aligned}\Pi_0^{T\to 0}(\mathbf{q},\omega) &= 2\int_{\substack{\epsilon_{\mathbf{k}}<\mu,\\ \epsilon_{\mathbf{k+q}}>\mu}} \frac{d\mathbf{k}}{(2\pi)^3}\cdot\theta(\omega)\left[\frac{1}{\omega-\epsilon_{\mathbf{k}}+\epsilon_{\mathbf{k+q}}+i\delta} - \frac{1}{\omega+\epsilon_{\mathbf{k}}-\epsilon_{\mathbf{k+q}}+i\delta}\right] + \\ &+ \theta(-\omega)\left[\frac{1}{\omega-\epsilon_{\mathbf{k}}+\epsilon_{\mathbf{k+q}}-i\delta} - \frac{1}{\omega+\epsilon_{\mathbf{k}}-\epsilon_{\mathbf{k+q}}-i\delta}\right].\end{aligned} \tag{1.100}$$

Comparing the real and the imaginary part of the above expression we can conclude that Eq. (1.100) is equivalently re–written in the form

$$\Pi_0^{T\to 0}(\mathbf{q},\omega) = 2\int_{\substack{\epsilon_{\mathbf{k}}<\mu,\\ \epsilon_{\mathbf{k+q}}>\mu}} \frac{d\mathbf{k}}{(2\pi)^3}\left[\frac{1}{\omega-\epsilon_{\mathbf{k}}+\epsilon_{\mathbf{k+q}}-i\delta} - \frac{1}{\omega+\epsilon_{\mathbf{k}}-\epsilon_{\mathbf{k+q}}+i\delta}\right], \tag{1.101}$$

having the same real and imaginary parts as Eq. (1.100).

1.4.2 The *GW* approximation

The lowest order self-energy in the screened interaction W is the GW approximation. In this approximation one plasmon (the quanta of W) is virtually scattered. The diagram representing the GW self-energy is shown in Fig. 1.5. In this paragraph I will explicitly write the band indexes.

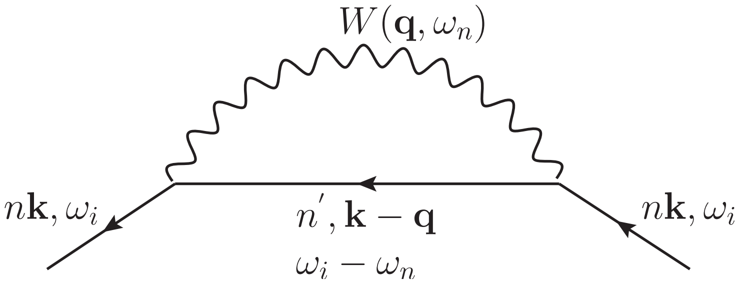

Figure 1.5: The *GW* self-energy diagram.

By using the standard diagrammatic rules [6] we can define the proper self-energy to be

$$\Sigma_{n\mathbf{k}}(\omega_i) = -\int \frac{d\,\mathbf{q}}{(2\pi)^3} \sum_{n'} \sum_{G_1 G_2} \rho_{nn'}(\mathbf{k},\mathbf{q},\mathbf{G_1}) \rho^*_{nn'}(\mathbf{k},\mathbf{q},\mathbf{G_2}) \\ \frac{1}{\beta} \sum_{n=-\infty}^{+\infty} \mathcal{G}^{(0)}_{n'}(\mathbf{k}-\mathbf{q},\omega_i-\omega_n) W_{\mathbf{G_1 G_2}}(\mathbf{q},\omega_n). \quad (1.102)$$

In Eq. (1.102) we have introduced several quantities. $\rho_{nn'}(\mathbf{k},\mathbf{q},\mathbf{G})$ are the scattering amplitudes defined as

$$\rho_{nn'}(\mathbf{k},\mathbf{q},\mathbf{G}) = \int d\mathbf{r}\, \phi^*_{n\mathbf{k}}(\mathbf{r}) e^{i(\mathbf{q}+\mathbf{G})\cdot\mathbf{r}} \phi_{n'\mathbf{k}-\mathbf{q}}(\mathbf{r}), \quad (1.103)$$

with $\mathbf{G}$ a reciprocal space vector. The screened interaction W is defined in terms of the dielectric function $\epsilon^{-1}(\mathbf{q},\omega_n)$

$$\hat{W}(\mathbf{q},\omega_n) = \hat{v}_{\mathbf{q}} \hat{\epsilon}^{-1}(\mathbf{q},\omega_n), \quad (1.104)$$

with

$$\epsilon^{-1}_{\mathbf{G_1 G_2}}(\mathbf{q},\omega_n) = \int d\mathbf{r} \int d\mathbf{r'}\, e^{-i(\mathbf{q}+\mathbf{G}_1)\cdot\mathbf{r}} e^{i(\mathbf{q}+\mathbf{G}_2)\cdot\mathbf{r'}} \epsilon^{-1}(\mathbf{r}\mathbf{r'},\omega_n). \quad (1.105)$$

The dielectric function is the key quantity of the GW approximation. It is indeed assumed that, in contrast to the bare interaction, W is much weaker. Consequently only the finite order in the expansion of the self-energy in W is retained. We also introduce the spectral representation of ϵ^{-1} defined as

$$\epsilon^{-1}_{\mathbf{G_1 G_2}}(\mathbf{q},\omega_n) = \delta_{\mathbf{G}_1,\mathbf{G}_2} + \frac{1}{\pi} \int dE\, \Gamma_{\mathbf{G_1 G_2}}(\mathbf{q},E) \left[\frac{1}{i\omega_n + E} - \frac{1}{i\omega_n - E} \right], \quad (1.106)$$

where

$$\Gamma_{\mathbf{G_1 G_2}}(\mathbf{q},E) = -\frac{1}{\pi} \epsilon^{-1,\delta}_{G_1,G_2}(\mathbf{q},E)\theta(E), \quad (1.107)$$

is the $\Gamma_{\mathbf{G_1 G_2}}$ definition in the $T = 0\,K$ limit.

The two terms appearing in ϵ^{-1} allows to split the self-energy in exchange and correlation terms

$$\Sigma_{n\mathbf{k}}(\omega_i) = \Sigma^X_{n\mathbf{k}} + \Sigma^C_{n\mathbf{k}}(\omega_i). \quad (1.108)$$

In order to do that we first note that the screened interaction acquires the form

$$W_{\mathbf{G_1 G_2}}(\mathbf{q},\omega_n) = v_{\mathbf{q}}(\mathbf{G_1}) \delta_{\mathbf{G_1 G_2}} + \\ + \int dE\, \Gamma_{\mathbf{G_1 G_2}}(\mathbf{q},E) \left[\frac{1}{i\omega_n - E} - \frac{1}{i\omega_n + E} \right] \frac{4\pi}{|\mathbf{q}+\mathbf{G_1}||\mathbf{q}+\mathbf{G_2}|}, \quad (1.109)$$

thanks to spectral representation of ϵ^{-1}.

If we plug Eq. (1.109) into Eq. (1.102) we have to evaluate the following sum

$$\sum_{n=-\infty}^{+\infty} \frac{1}{i\omega_i - i\omega_n - \epsilon_{n'\mathbf{k}-\mathbf{q}} + \mu} \cdot \left[\frac{1}{i\omega_n + E} - \frac{1}{i\omega_n - E}\right]. \tag{1.110}$$

We define the function

$$F(\omega) = \frac{1}{i\omega_i - \omega - \epsilon_{n'\mathbf{k}-\mathbf{q}} + \mu} \cdot \left[\frac{1}{\omega + E} - \frac{1}{\omega - E}\right], \tag{1.111}$$

recognizing $F(i\omega_n)$ as the summand in Eq. (1.110).

By following the same procedure outlined in Sec. 1.4.1, we convert the sum into an integral along the contour $\mathcal{C}'$ shown in Fig. 1.6. $\mathcal{C}'$ edges a region on the complex plane in which poles both of $F(\omega)$ and $B(\omega)$ fall. $B(\omega) = (e^{\beta\omega} - 1)^{-1}$ is the Bose function distribution having poles at the frequencies

$$\omega = i\frac{2n\pi}{\beta} = i\omega_n, \quad n = 0, \ \pm 1, \ \pm 2, \ \dots \ . \tag{1.112}$$

Applying the residuals theorem, the contour integral can be evaluated as follows

$$\begin{aligned} \underbrace{\oint_{\mathcal{C}'} d\omega F(\omega) B(\omega)}_{I} &= 2\pi i \sum \text{Residues of} \, F(\omega)B(\omega)\Big|_{\omega=\text{``poles of } F(\omega)\text{''}} + \\ &+ \underbrace{\oint_{\mathcal{C}} d\omega F(\omega) B(\omega)}_{J}, \end{aligned} \tag{1.113}$$

where poles of $F(\omega)$ are $\omega = \pm E$ and $\omega = i\omega_i - \epsilon_{n'\mathbf{k}-\mathbf{q}} + \mu$. J is the integral evaluated over the contour $\mathcal{C}$ enclosing all poles of the Bose function distribution. The residuals theorem leads to the result for the integral J

$$J = 2\pi i \frac{1}{\beta} \sum_{n=-\infty}^{+\infty} F(i\omega_n). \tag{1.114}$$

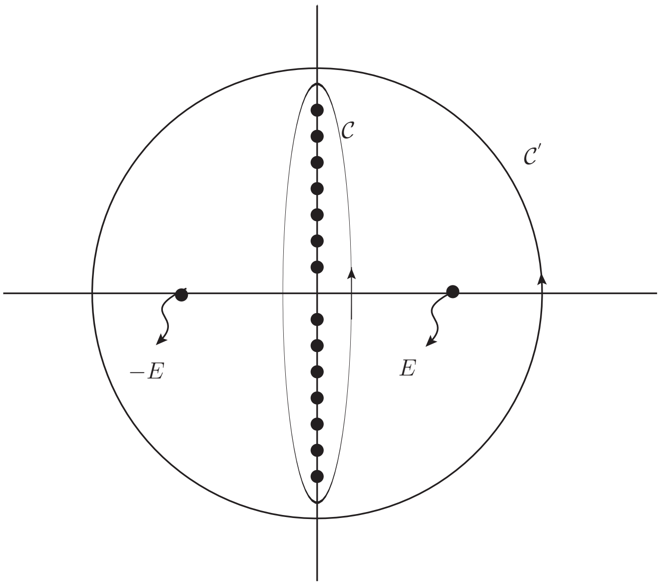

Figure 1.6: The contour on the complex plane used to integrate the GW electronic self-energy.

If we consider now a contour $\mathcal{C}' : Re^{i\theta}$ covering the entire complex plane ($R \to \infty$), the contour integral I is doomed to vanish. The integrand, indeed, goes to zero exponentially as $\omega \in \mathcal{C}'$. Therefore an explicit expression for the Matsubara sum can be set in terms of a more accessible sum of residues of the integrand $F(\omega)B(\omega)$

$$-\frac{1}{\beta}\sum_{n=-\infty}^{+\infty} F(i\omega_n) = \text{Res}\left[F(\omega)B(\omega)\right]\big|_{\omega=\pm E} + \text{Res}\left[F(\omega)B(\omega)\right]\big|_{\omega=i\omega_i-\epsilon_{n'\mathbf{k}-\mathbf{q}}+\mu} . \tag{1.115}$$

The residues evaluated at each pole are shown as follows

$$\omega = E \qquad \text{Res}_1 = -\frac{B(E)}{i\omega_i - E - \epsilon_{n'\mathbf{k}-\mathbf{q}} + \mu}, \tag{1.116}$$

$$\omega = -E \qquad \text{Res}_2 = \frac{B(-E)}{i\omega_i + E - \epsilon_{n'\mathbf{k}-\mathbf{q}} + \mu}, \tag{1.117}$$

$$\omega = i\omega_i - \epsilon_{n'\mathbf{k}-\mathbf{q}} + \mu \qquad \text{Res}_3 = \frac{2EB(i\omega_i - \epsilon_{n'\mathbf{k}-\mathbf{q}} + \mu)}{[(i\omega_i - \epsilon_{n'\mathbf{k}-\mathbf{q}} + \mu)^2 - E^2]}. \tag{1.118}$$

Finally, we use the Bose function properties and the frequencies ω_i as odd multiples of $\frac{\pi}{\beta}$ to observe that $B(-E) = -1 - B(E)$ and $B(i\omega_i - \epsilon_{n'\mathbf{k}-\mathbf{q}} + \mu) = -1 + f_{n'\mathbf{k}-\mathbf{q}}$. These expressions can be readily exploited to re–write Eq. (1.115) in a more compact form

$$\frac{1}{\beta}\sum_{n=-\infty}^{+\infty} F(i\omega_n) = \frac{B(E) + 1 - f_{n'\mathbf{k}-\mathbf{q}}}{i\omega_i - E - \epsilon_{n'\mathbf{k}-\mathbf{q}} + \mu} + \frac{B(E) + f_{n'\mathbf{k}-\mathbf{q}}}{i\omega_i + E - \epsilon_{n'\mathbf{k}-\mathbf{q}} + \mu}. \tag{1.119}$$

Once the summation has been explicitly evaluated the final expression for $\Sigma^{C}_{n\mathbf{k}}(\omega_i)$

is given by the following equation

$$\Sigma^C_{n\mathbf{k}}(\omega_i) = \int \frac{d\,\mathbf{q}}{(2\pi)^3} \sum_{n'} \sum_{G_1 G_2} \rho_{nn'}(\mathbf{k},\mathbf{q},\mathbf{G_1}) \rho^*_{nn'}(\mathbf{k},\mathbf{q},\mathbf{G_2}) \cdot \\ \int_{-\infty}^{\infty} dE \; \Gamma_{\mathbf{G_1 G_2}}(\mathbf{q},E) \frac{4\pi}{|\mathbf{q}+\mathbf{G_1}||\mathbf{q}+\mathbf{G_2}|} \left[\frac{B(E)+1-f_{n'\mathbf{k}-\mathbf{q}}}{i\omega_i - E - \epsilon_{n'\mathbf{k}-\mathbf{q}} + \mu} + \right. \\ \left. + \frac{B(E)+f_{n'\mathbf{k}-\mathbf{q}}}{i\omega_i + E - \epsilon_{n'\mathbf{k}-\mathbf{q}} + \mu} \right]. \quad (1.120)$$

In order to move on the real axis we need to perform the analytic continuation, which allows to re–write $\Sigma^C_{n\mathbf{k}}(\omega_i)$ on the real axis

$$\Sigma^C_{n\mathbf{k}}(\omega - i\delta) = \int \frac{d\,\mathbf{q}}{(2\pi)^3} \sum_{n'} \sum_{G_1 G_2} \rho_{nn'}(\mathbf{k},\mathbf{q},\mathbf{G_1}) \rho^*_{nn'}(\mathbf{k},\mathbf{q},\mathbf{G_2}) \cdot \\ \int_{\infty}^{\infty} dE \; \Gamma_{\mathbf{G_1 G_2}}(\mathbf{q},E) \frac{4\pi}{|\mathbf{q}+\mathbf{G_1}||\mathbf{q}+\mathbf{G_2}|} \left[\frac{B(E)+1-f_{n'\mathbf{k}-\mathbf{q}}}{i\omega_i - E - \epsilon_{n'\mathbf{k}-\mathbf{q}} + \mu} + \right. \\ \left. + \frac{B(E)+f_{n'\mathbf{k}-\mathbf{q}}}{i\omega_i + E - \epsilon_{n'\mathbf{k}-\mathbf{q}} + \mu} \right]. \quad (1.121)$$

The exchange self-energy, instead, follows the standard expression

$$\Sigma^X_{n\mathbf{k}} = -\int \frac{d\,\mathbf{q}}{(2\pi)^3} \sum_{n'} \sum_{G} |\rho_{nn'}(\mathbf{k},\mathbf{q},\mathbf{G})|^2 f_{n'\mathbf{k}-\mathbf{q}} \frac{4\pi}{|\mathbf{q}+\mathbf{G}|^{\mathbf{2}}}. \quad (1.122)$$

By comparing Eq. (1.120) with its zero temperature limit we see that the Bose factor $B(E)$ dictates the occupation of the poles of W. For systems with a gap the lowest energy excitation of W is at the gap. As the temperature corresponding to the gap is huge (thousands of K), in these systems electrons live at zero temperature, regardless of the external temperature.

In Chap. 3 I will show, instead, as the picture changes completely when the scattering with phonons are included in the GW self-energy. The key point is that phonons have energies three orders of magnitude smaller than plasmons, the poles of W. Consequently the phonon temperature (the Debye temperature) is, in general, of the same order of the experimental temperatures. Therefore, although the temperature effect on the electron–electron scattering can be neglected, this is not true for the electron–phonon scattering.

Bibliography

[1] G.D. Mahan Many–Particle Physics (New York: Plenum) 1998

[2] G. Grosso and G. Pastori Parravicini *Solid State Physics*, Elsevier Academic Press (2004)

[3] R. M. Dreizler and E. K. U. Gross *Density Functional Theory*, Springer Verlag Heidelberg (1990)

[4] P. Hohenberg and W. Kohn, Phys. Rev. **136**, B864 (1964).

[5] W. Kohn and L. J. Sham, Phys. Rev. **140**, A1113 (1965).

[6] L. Fetter and J.D. Walecka *Quantum theory of Many–Body Systems*, McGraw–Hill, New York, N.Y. 1981.

[7] L. Hedin and B. I. Lundqvist, J. Phys. C **4**, 2064 (1971).

[8] D.M. Ceperley and B.I. Alder, Phys. Rev. Lett. **45**, 566 (1980).

[9] J. P. Perdew and A. Zunger, Phys. Rev. B **23**, 5048 (1981).

[10] R. O. Jones and I. Gunnarson, Rev. Mod. Phys. **61**, 689 (1989).

[11] L. Fetter and J.D. Walecka Chap.9, *Quantum theory of Many–Body Systems*

Chapter 2

Phonons: beyond the rigid ions approximation

Many crucial phenomena in modern solid-state physics are deeply linked to the theory of the lattice vibrations. A wide range of physical properties depends on the lattice-dynamics: for example specific heats, thermal expansion and heat conduction. On the other side resistivity of metals, superconductivity and thermal dependence of optical spectra are related to the electron-phonon interaction. Moreover, vibrational spectroscopy is a very important tool for the characterization of materials. Vibrational frequencies are measured mainly using infrared and Raman spectroscopy, as well as in neutron-diffraction spectra.

As it will be clear in the following the screening of the atoms built-up by electrons plays an essential role in the devise of an accurate theory of lattice vibrations. Only by taking into account the mutual effects of the electronic correlation and atomic vibrations it is possible to be predictive and accurate.

A systematic study of the lattice dynamics in several systems was then performed since 1970's [1, 2]; a large number of ab-initio calculations based on the linear response (LR) theory of lattice vibrations followed the increasing success of density-functional theory (DFT) [3, 4]. LR and DFT are naturally merged fusion in Density Functional Perturbation Theory (DFPT), a method to conjugate DFT and lattice dynamics in the LR regime. The availability of efficient numerical codes and the state-of-the-art tools used in theoretical condensed-matter physics is such that nowadays the lattice dynamics of specific materials can be obtained using *ab-initio* QM techniques starting from the chemical composition of the material. In this way it is possible to obtain accurate phonon dispersions on a fine grid of wave vectors covering the Brillouin Zone (BZ), which can be directly compared with neutron diffraction data, and from which several physical properties (heat capacities, thermal expansion coefficient, temperature dependence of the band gap) can be calculated.

The purpose of the present chapter is to illustrate the key concepts of DFPT (Sec. 2.1). I will then apply DFPT to the *trans*-polyacetylene (Sec. 2.2) and polyethylene (Sec. 2.3) obtaining phonon dispersion curves. In Sec. 2.4 I will motivate the reason to discard the acoustic modes responsible for bending of the chain. I will conclude this chapter with a first simplified approach to the electronic instabilities induced by the atomic motion. By using a Monte Carlo algorithm (Sec. 2.5) I will show how electrons are strongly influenced by the atomic motion.

2.1 Density Functional Perturbation Theory

The Born-Oppenheimer approximation is widely used and most of the *ab-initio* calculations are performed assuming nuclei frozen in their equilibrium positions. The equilibrium geometry is determined by the condition that the forces acting on all nuclei vanish:

$$\mathbf{F}_I \equiv -\frac{\partial E(\{\mathbf{R}\})}{\partial \mathbf{R}_I} = 0, \tag{2.1}$$

where $E(\{\mathbf{R}\})$ is the ground state energy of the Hamiltonian of a system of N interacting electrons moving in the field of fixed nuclei with coordinates $\{\mathbf{R}\}$.

The computation of the first and the second derivative of the *Born Oppenheimer surface* are accomplished using the Hellmann-Feynman theorem [5, 6]. This states that if the Hamiltonian H_λ depends on a parameter λ the first derivative of the eigenvalues of H_λ, with respect to the parameter λ, is given by the expectation value of the derivative of H_λ, on its ground state wavefunction $\mid \Psi_\lambda\rangle$:

$$\frac{\partial E_\lambda}{\partial \lambda} = \langle \Psi_\lambda \mid \frac{\partial H_\lambda}{\partial \lambda} \mid \Psi_\lambda\rangle. \tag{2.2}$$

In the BO approximation the parameter λ represents the nuclear coordinates of the Ith nucleus $\mathbf{R}_I$. The forces on the nucleus are evaluated in the electronic ground state $\mid \Psi\,(\mathbf{r},\mathbf{R})\rangle$ of the Hamiltonian $H_{BO}(\mathbf{R})$:

$$\mathbf{F}_I = -\frac{\partial E(\{\mathbf{R}\})}{\partial \mathbf{R}_I} = -\langle \Psi\,(\mathbf{r},\mathbf{R}) \mid \frac{\partial H_{BO}(\{\mathbf{R}\})}{\partial \mathbf{R}_I} \mid \Psi\,(\mathbf{r},\mathbf{R})\rangle. \tag{2.3}$$

The dependence of $H_{BO}(\mathbf{R})$ on the nuclear coordinates is through the electron-nucleus and the nucleus-nucleus interaction. The Hellmann-Feynman theorem states in this case that:

$$\mathbf{F}_I = -\int d\mathbf{r}\, n_{\mathbf{R}}(\mathbf{r}) \frac{\partial V_{\mathbf{R}}(\mathbf{r})}{\partial \mathbf{R}_I} - \frac{\partial E_N(\{\mathbf{R}\})}{\partial \mathbf{R}_I}, \tag{2.4}$$

where $n_{\mathbf{R}}(\mathbf{r})$ is the electron charge density for the nuclear configuration $\{\mathbf{R}\}$.

For a system near its equilibrium geometry, the harmonic approximation holds and the nuclear Hamiltonian

$$\mathcal{H} = -\sum_I \frac{\hbar^2}{2M_I}\frac{\partial^2}{\partial \mathbf{R}_I^2} + E(\{\mathbf{R}\}), \tag{2.5}$$

reduces to the Hamiltonian of a system of independent harmonic oscillators, called *normal modes*. Normal mode frequencies, ω, and displacement patterns, $u_{\alpha I}$ for the α^{th} Cartesian component of the *Ith* atom are determined by the secular equation:

$$\sum_{J,\beta}(C_{IJ}^{\alpha\beta} - M_I\omega^2\delta_{IJ}\delta_{\alpha\beta})u_{\beta J} = 0, \tag{2.6}$$

where $C_{IJ}^{\alpha\beta}$ is the matrix of the *interatomic force constants (IFC's)*:

$$C_{IJ}^{\alpha\beta} \equiv \frac{\partial^2 E(\{\mathbf{R}\})}{\partial \mathbf{R}_{I,\alpha}\partial \mathbf{R}_{J,\beta}} = -\frac{\partial F_I^\alpha}{\partial \mathbf{R}_J,\beta}. \tag{2.7}$$

The vibrational frequencies are linked to the Hessian of the *Born Oppenheimer surface* rescaled by the square root of the masses product:

$$det\left|\frac{1}{\sqrt{M_I M_J}}\frac{\partial^2 E(\{\mathbf{R}\})}{\partial \mathbf{R}_I \partial \mathbf{R}_J} - \omega^2\right| = 0. \tag{2.8}$$

Now the evaluation of the Hessian of the *Born Oppenheimer surface* can be easily done by evaluating the derivative of Eq. (2.4) with respect to $\mathbf{R}_J$:

$$\frac{\partial^2 E(\mathbf{R})}{\partial \mathbf{R}_I \partial \mathbf{R}_J} = \int d\mathbf{r}\,\frac{\partial n_{\mathbf{R}}(\mathbf{r})}{\partial \mathbf{R}_J}\frac{\partial V_{\mathbf{R}}(\mathbf{r})}{\partial \mathbf{R}_I} + \int d\mathbf{r}\,n_{\mathbf{R}}(\mathbf{r})\frac{\partial^2 V_{\mathbf{R}}(\mathbf{r})}{\partial \mathbf{R}_I \partial \mathbf{R}_J} + \frac{\partial^2 E_N(\mathbf{R})}{\partial \mathbf{R}_I \partial \mathbf{R}_J}. \tag{2.9}$$

IFC's can be calculated as finite differences of Hellmann-Feynman forces for small finite displacements of atoms around the equilibrium positions. This is the *frozen phonon technique* often used to calculate IFC's in solid state physics. The evaluation of the IFC's matrix needs indeed the density and its linear response to a nuclear geometry distortion. Within DFT not only the ground density but also the electron density linear response can be obtained. The following procedure is known as *density functional perturbation theory* (DFPT).

The electron-density response appearing in Eq. (2.9) can be evaluated linearizing the equation for the density with respect to derivatives of KS orbitals

$$\Delta n_{\mathbf{R}}(\mathbf{r}) = 4\Re\sum_{n=1}^{N/2}\psi_m^*\Delta\psi_m. \tag{2.10}$$

Since the external potential is a real function, each KS wavefunction is degenerate to its complex conjugate. The variation of ψ_m is obtained from the linearization of the Kohn-Sham equation with respect to the derivatives of the density

$$(H_{scf} - \epsilon_n) \mid \Delta\psi_n\rangle = -(\Delta V_{scf} - \Delta\epsilon_n) \mid \psi_n\rangle, \tag{2.11}$$

where H_{scf} is the unperturbed Hamiltonian

$$H_{scf} = -\frac{\hbar^2}{2m}\frac{\partial^2}{\partial \mathbf{r}^2} + V_{scf}(\mathbf{r}), \tag{2.12}$$

and

$$\frac{\partial\epsilon_n}{\partial \mathbf{R}_I} = \langle\phi_n \mid \frac{\partial V_{scf}(\mathbf{r})}{\partial \mathbf{R}_I} \mid \phi_n\rangle, \tag{2.13}$$

is the first-order derivative of the KS eigenvalue.

The Kohn-Sham equations define a self-consistent potential including the Hartree, the exchange-correlation and the ionic potentials

$$V_{scf}(\mathbf{r}) = V_{\mathbf{R}}(\mathbf{r}) + V_H(\mathbf{r}) + V_{xc}(\mathbf{r}). \tag{2.14}$$

The first order derivative of V_{scf} reads

$$\Delta V_{scf}(\mathbf{r}) = \Delta V_{\mathbf{R}}(\mathbf{r}) + e^2 \int d\mathbf{r}' \, \frac{\Delta n_{\mathbf{R}}(\mathbf{r}')}{|\mathbf{r}-\mathbf{r}'|} + \left.\frac{dv_{xc}(n)}{dn}\right|_{n=n(\mathbf{r})} \Delta n_{\mathbf{R}}(\mathbf{r}). \tag{2.15}$$

ΔV_{scf} represents the change of the self-consistent potential due to a rearrangement of the electronic density. In the case of phonon calculation the change in $n(\mathbf{r})$ reflects the screening of the ionic potential.

Eqs. (2.10), (2.11) and (2.15) constitute a set of linear equations to be solved self-consistently, analogously to the KS equations in the unperturbed case Eq. (1.29–1.30). In this case the self consistency is explicit in the second member of Eq. (2.11) as it depends in fact on the solution of the linear system itself. Moreover all equations that compose the DFPT scheme are coupled to each other because of the dependence of $\Delta n(\mathbf{r})$ on all $\Delta\psi_n$. The first order correction to ψ_n is expressed by the sum over all the eigenstates of H_{SCF}

$$\Delta\psi_n(\mathbf{r}) = \sum_{n_{occ}=1}^{N/2} \sum_{m\neq n} \psi_m(\mathbf{r}) \frac{\langle\psi_m \mid \Delta V_{scf} \mid \psi_n\rangle}{\epsilon_n - \epsilon_m}. \tag{2.16}$$

If Eq. (2.16) is used to calculate the electron charge-density linear response we get, from Eq. (2.10)

$$\Delta n(\mathbf{r}) = 4 \sum_{n_{occ}=1}^{N/2} \sum_{m\neq n} \psi_n^*(\mathbf{r})\psi_m(\mathbf{r}) \frac{\langle\psi_m \mid \Delta V_{scf} \mid \psi_n\rangle}{\epsilon_n - \epsilon_m}, \tag{2.17}$$

where products of occupied states cancel each other. As a consequence, the contribution to the electron-density response comes from a sum over empty states. Eq. (2.17) shows that the electron density responds to a perturbation exciting virtual empty states.

The theory of lattice dynamics can be equivalently formulated in terms of the dielectric matrix $\epsilon^{-1}(\mathbf{r},\mathbf{r}')$ which links the perturbation of the external potential to the total potential experienced by a test charge

$$\Delta V_{test}(\mathbf{r}) = \int d\mathbf{r}'\,\epsilon^{-1}(\mathbf{r},\mathbf{r}')\Delta V_{\mathbf{R}}(\mathbf{r}'). \tag{2.18}$$

$\Delta n(\mathbf{r})$ can also be expressed in terms of electron polarizability $\chi(\mathbf{r},\mathbf{r}')$, as, in the linear response regime,

$$\Delta n(\mathbf{r}) = \int d\mathbf{r}'\,\chi(\mathbf{r},\mathbf{r}')\Delta V_{\mathbf{R}}(\mathbf{r}'). \tag{2.19}$$

$\chi(\mathbf{r},\mathbf{r}')$ and $\epsilon^{-1}(\mathbf{r},\mathbf{r}')$ are linked together by the relation

$$\epsilon^{-1}(\mathbf{r},\mathbf{r}') = \delta(\mathbf{r}-\mathbf{r}') + \int d\mathbf{r}''\,\frac{e^2}{|\mathbf{r}-\mathbf{r}''|}\chi(\mathbf{r}'',\mathbf{r}'). \tag{2.20}$$

The static approximation to the screening of the self-consistent potential is reliable when the plasma frequency of the system is greater then the typical phononic frequencies. Lazzeri and Mauri [7] studied and explained the Kohn anomaly (KA) appearing in the phonon dispersion of doped graphene within a time dependent perturbation theory. Only by considering a phonon as a dynamical perturbation it is possible to describe the KA. Even if the adiabatic BOA is considered valid in most of materials and it's commonly used for phonon calculations, doped graphene is an example where this approximation fails.

Within DFT the linear response of the charge distribution is related to the variation of the self consistent field through the independent electron polarizability

$$\Delta n(\mathbf{r}) = \int d\mathbf{r}'\,\chi_0(\mathbf{r},\mathbf{r}')\Delta V_{scf}(\mathbf{r}'). \tag{2.21}$$

Combining Eq. (2.19) and Eq. (2.21) we get a matrix equation for χ

$$\chi(\mathbf{r},\mathbf{r}') = \chi_0(\mathbf{r},\mathbf{r}') + \int d\mathbf{r}_1 \int d\mathbf{r}_2\,\chi_0(\mathbf{r},\mathbf{r}_1)K(\mathbf{r}_1,\mathbf{r}_2)\chi(\mathbf{r}_2,\mathbf{r}'). \tag{2.22}$$

This is the Time Dependent Density Functional Theory (TDDFT) equation for the response function related to the Kohn-Sham response function $\chi_0(\mathbf{r},\mathbf{r}')$. The kernel $K(\mathbf{r}_1,\mathbf{r}_2)$ is defined as

$$K(\mathbf{r}_1,\mathbf{r}_2) = v_H(\mathbf{r}_1,\mathbf{r}_2) + f_{xc}(\mathbf{r}_1,\mathbf{r}_2), \tag{2.23}$$

where f_{xc} is the static exchange-correlation kernel

$$f_{xc}(\mathbf{r}_1, \mathbf{r}_2) = \frac{\delta v_{xc}\left[n(\mathbf{r}_1)\right]}{\delta n(\mathbf{r}_2)}. \tag{2.24}$$

2.2 Trans-Polyacetylene

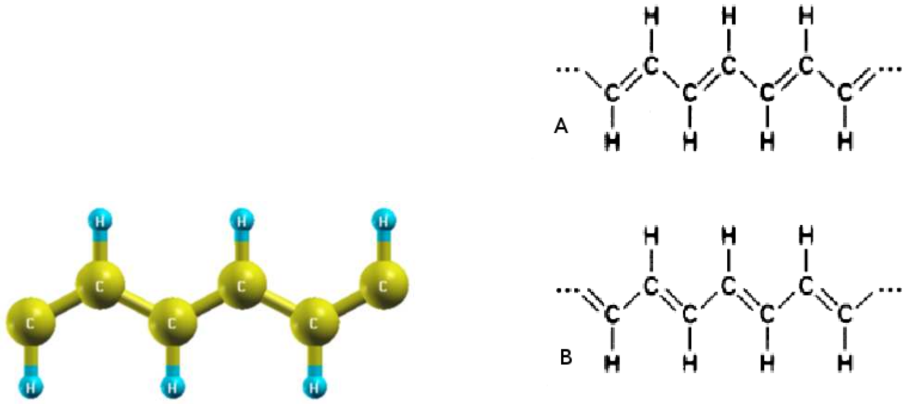

Figure 2.1: Segment of the *trans*-polyacetylene chain (left figure) and the two possible atomic configurations corresponding to the distorted chain (right figure). Both configurations have the same energy.

As mentioned above, one of the two systems studied in this work is *trans*-polyacetylene, the simplest conjugated polymer.

Polyacetylene is a linear polymer. Since carbon electronic structure is $1s^2 2s^2 2p^2$, each atom forms four nearest-neighbour bonds. Three of the four carbon valence electrons are in sp^2 hybridized orbitals; two of the σ-type bonds connect neighbouring carbons along the one-dimensional (1D) backbone, while the third forms a bond with the hydrogen side group. The remaining valence electron has the symmetry of a p_z orbital with its charge density lobes perpendicular to the plane defined by the other three bonds. In terms of an energy-band description, the σ-bonds form completely filled bands, while the π bond leads to the partially filled energy band responsible for the important electronic properties.

If all the bond lengths were equal, pure *trans*-polyacetylene would be a quasi-1D metal with a half filled band. Such a system is unstable with respect to a dimerization distortion, the Peierls instability [8], which induce adjacent $C - H$ groups to move toward each other forming alternated short and double bonds. In this way the energy of the system is lowered. Clearly one could interchange the double and the single bonds without changing the ground state total energy. Since there are two lowest-energy states, A and B (see Fig. 2.1), having two distinct bonding structures but the same energy, *trans*-polyacetylene is termed as a "degenerate ground state" system.

2.2.1 The ground state and electrons

The ground state wavefunctions and the phonon frequencies of all studied systems have been performed using `Quantum Espresso` [9] (Q/E). Q/E is an integrated suite of computer codes for electronic-structure and phonons calculations [3], implementing Density-Functional Theory (see Sec. 1.2) and Density-Functional Perturbation Theory (see Sec. 2.1) in a plane-wave basis set. The exchange-correlation energy and potential are taken from Ref. [10]. For the description of the electron ion interaction instead, a scheme proposed by Von Barth and Car has been used [11].

The planar structure of *trans*-polyacetylene (*trans*-PA) is sketched in Fig. 2.2 (left panel) together with the lattice constant in the direction of the polymer axis and the bonding alternation between carbon atoms. That geometry has been taken from Ref. [12].

The isolated chain can be simulated in an orthorhombic cell with primitive lattice vectors **a**, **b**, **c**, whose lengths are 4.643, 25, 25 a.u. respectively (see right panel Fig. 2.2). The unit cell contains 4 atoms, i.e. 2 $C-H$ groups.

I performed convergence tests to find the most accurate kinetic energy cutoff (E_{cut}) and volume to describe the ground state. E_{cut} was varied from 30 Ry to 60 Ry in steps of 5 Ry. The total energy and the DFT electronic gap converge respectively to -24.93 eV and 0.883 eV, at E_{cut} equals to 40 Ry. In order to reduce the number of plane waves, I also checked the optimal vacuum size by reducing both sides **b** and **c** of the simulation cell. Convergence tests involving total energy and the electronic gap, lead us to conclude that a kinetic energy cutoff of 40 Ry, with primitive cell vectors 4.643, 15, 15 a.u. can be used.

Since the phonon frequencies are almost independent on the unit cell volume, I fixed it to have **a**=4.643 a.u., **b**=15 a.u., **c**=15 a.u. . Then I looked at the phonon frequencies at the Γ point, i.e. at the wavevector $\mathbf{q} = (0, 0, 0)$, both at $E_{cut} = 30$ Ry and $E_{cut} = 40$ Ry.

The Q/E code performs 3·(#atoms) linear response calculations, one per atomic displacement. As the unit cell is made up of 4 atoms, the number of phononic branches is 12.

Increasing the kinetic energy cutoff, optical frequencies approach to the corresponding observed values in the infrared and Raman spectra [13, 14, 15] (see Tab. 2.1) even if the Debye frequency is still too large.

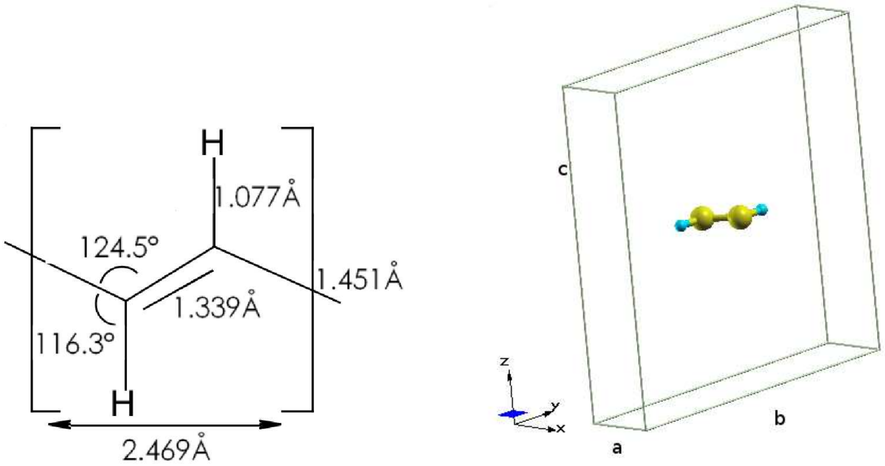

Figure 2.2: The *trans*-polyacetylene monomer geometry (left panel). The single and double bond alternation is a typical feature of conjugated polymers. Simulation cell (right panel). The bond alternation imposes the lattice constant **a** to be on the $\hat{x}$ direction. The other two, **b** and **c** are chosen large enough in order to simulate an isolated chain.

Optical Modes $[cm^{-1}]$								
Experimental freq.^{a}	3013	2990	1457	1294	1170	1066	1012	884
LDA ($E_{cut} = 40\,\mathrm{Ry}$)	3304	3289	1587	1253	1120	1055	910	834
LDA ($E_{cut} = 30\,\mathrm{Ry}$)	3502	3487	1764	1273	1091	982	814	764

Table 2.1: Comparison between the experimental and calculated optical phonons frequencies of a *trans*-polyacetylene chain at Γ point. ^{a}References [13, 14, 15].

The four lowest frequencies (the acoustic ones) I obtained at the Γ point with $E_{cut} = 30\,\mathrm{Ry}$ are all negative, in the range $-430\,cm^{-1} \div 40\,cm^{-1}$, instead of being zero due to the acoustic sum rule (ASR), i.e. the translational invariance and the rotational invariance with respect to the polymer axis.

Unlikely in approximated calculations the ASR is violated. In plane waves calculations the most irreducible violation comes from the discreteness of the FFT grid, as a consequence of the chosen E_{cut}. Indeed the same calculation performed with a denser FFT grid (E_{cut}=40 Ry) leads to a smaller range of energies spanned by the acoustic frequencies: $-320\,cm^{-1} \div 60\,cm^{-1}$. Frequencies, however, are partially still negative which points to a real instability, i.e. atoms are not in the configuration which minimizes the total energy.

To confirm the geometric instability, I first moved carbon atoms keeping fixed

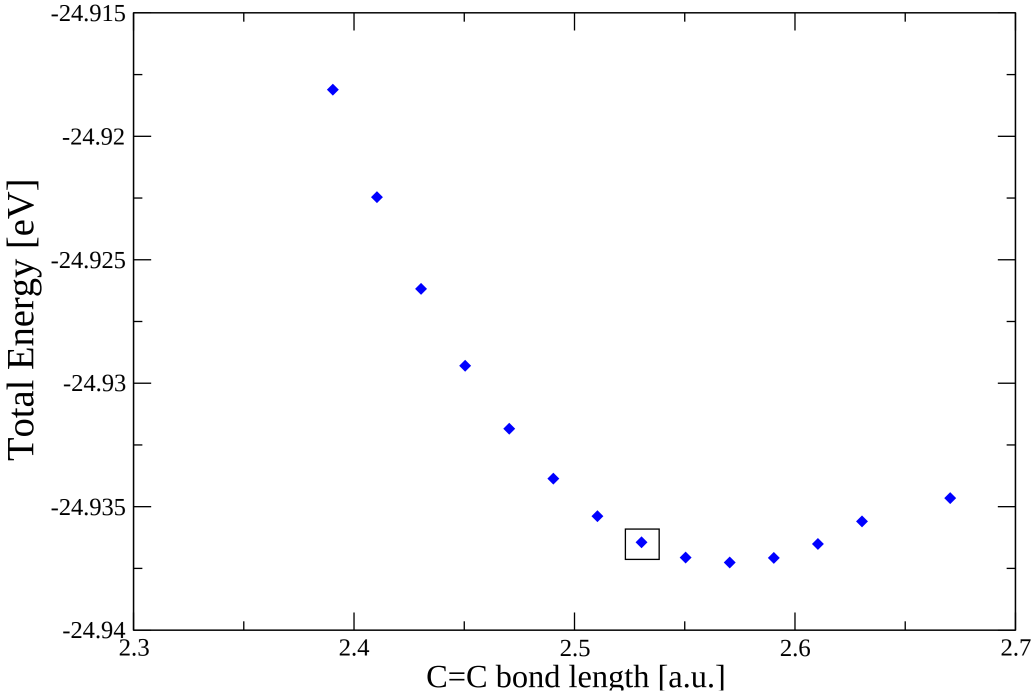

Figure 2.3: Calculated total energy versus C=C bond length. A parabolic fit shows that the minimum is located at a C=C bond length equal to $\sim$ 2.58 a.u.

the monomer centre of mass. By changing the double bond length I obtain several configurations whose total energy is computed by means of a ground state calculation. The total energy as a function of the double bond $C = C$ length value is shown in Fig. 2.3. The most striking result is that the total energy has a minimum when carbon atoms are $\sim$ 2.58 a.u. far apart. In the experimental geometry instead the double bond length is 2.53 a.u.; the corresponding total energy is that highlighted by a small square in Fig. 2.3.

This means that the chosen geometric structure is not the equilibrium one and it should be relaxed. Consequently I optimized the atomic positions (bond lengths and bond angles) by means of a standard minimization algorithm, in an orthorhombic cell (a=4.643 a.u., b=23 a.u., c=23 a.u.) and E_{cut}=40 Ry. The new structure is sketched in Fig. 2.4 and it corresponds to a total energy equal to -24.938 eV. The difference in length between double and single bonds is an important structural parameter and it was object of a long experimental debate. The double bond length I obtain turns out to be very similar to that one observed in NMR experiment [16]. Fixing the optimized monomer geometry, I calculated the lattice constant in the direction of the polymer axis in order to get a $C - C$ length equal to the experimental value 1.44 Å [16].

With the optimized geometry I finally calculated the electronic band structure,

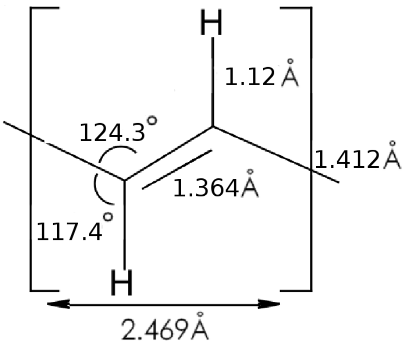

Figure 2.4: Calculated geometry of *trans*-polyacetylene, obtained by a minimization of the total energy.

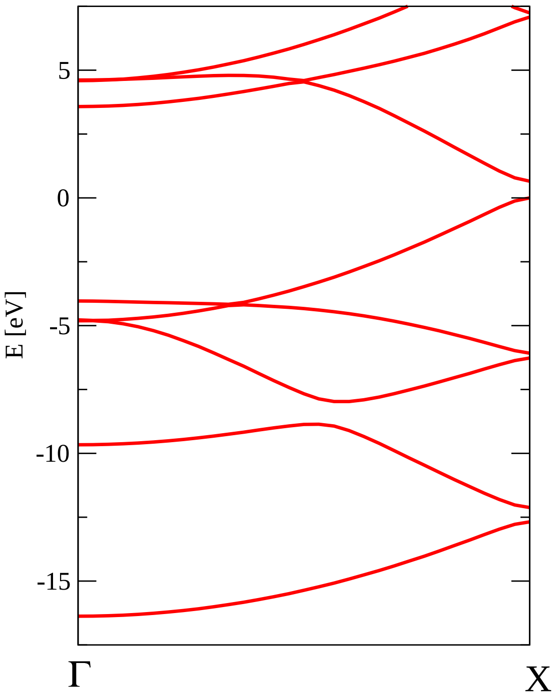

Figure 2.5: Electronic Band Structure of *trans*-polyacetylene.

finding an electronic band gap of 0.6 eV, lower than in the previous geometry. The translational symmetry of the polymer chain implies that the solutions of the Scrödinger equation must be of the Bloch form, $\Psi(k, \mathbf{r}) = u_k(\mathbf{r})e^{ikx}$, where $u_k(\mathbf{r})$ is a periodic function and k is the crystal momentum along the x direction. Periodicity in reciprocal space implies that $\Psi(k, \mathbf{r}) = \Psi(k + G, \mathbf{r})$, where G is the reciprocal lattice vector. The first BZ is defined by the region between $-\frac{\pi}{a} <= k <= \frac{\pi}{a}$. The electronic band structure is shown in Fig. 2.5. The highest occupied state at X has been shifted in order to have zero energy.

Optical Modes [cm^{-1}]								
Experimental freq.[a]	3013	2990	1457	1294	1170	1066	1012	884
LDA (E_{cut}=40 Ry)	2911	2890	1552	1261	1176	1162	1037	923
LDA (E_{cut}=30 Ry)	3154	3136	1716	1312	1176	1114	984	867

Table 2.2: Comparison between the experimental and calculated optical phonons frequencies of a *trans*-polyacetylene at Γ point for the relaxed geometry shown in Fig. 2.4.[a]References [13, 14, 15].

Acoustic Modes [cm^{-1}]				
LDA (E_{cut}=40 Ry)	215	50	33	−38
LDA (E_{cut}=30 Ry)	98	39	27	−37

Table 2.3: Calculated acoustic phonons frequencies of a *trans*-polyacetylene at Γ point for the relaxed geometry shown in the Fig. 2.4.

2.2.2 Phonons

I performed DFPT calculations starting from the fully relaxed structure. I checked again phonon frequencies at wavevector $\mathbf{q} = (0, 0, 0)$

The effect of the relaxation is clearly decisive. The most impressive effect appears in the four lowest acoustic frequencies, shown in Tab. 2.3. Then I used DFPT to calculate the full phonon bands. In order to do that, it is convenient to calculate IFC's in real space. The calculation involves three steps:

1. a self consistent step calculation of the charge density and Kohn-Sham orbitals for the unperturbed system.

2. the calculation of phonons and dynamical matrices on a uniform grid of **q**-vectors including Γ.

3. the transformation of the dynamical matrices from **G**-space to **R**-space. Once the IFC's in real space are available, one can calculate phonons frequencies at any wavevector **q**, by just reconstructing the dynamical matrix. If the grid is dense enough the reconstructed dynamical matrix will be accurate. This procedure is a "Fourier interpolation" of the IFC's.

Phonon Frequencies [cm^{-1}] at $\mathbf{q}$=0.37($\frac{2\pi}{a}$, 0, 0)												
$N_{\mathbf{q}}$	257	312	440	612	866	937	1108	1254	1285	1532	2893	2905
10	245	309	436	603	873	935	1114	1250	1283	1527	2894	2906
26	267	318	449	612	873	934	1113	1256	1287	1541	2895	2906
40	263	317	448	611	872	934	1111	1255	1286	1540	2895	2906

Table 2.4: Calculated phonon frequencies on a $\mathbf{q}$ vector not included in the three grids. The convergence on the grid is reached when the direct calculation and the Fourier interpolation give the same result within an accuracy range.

Charge density and Kohn-Sham orbitals were calculated with a E_{cut}=40 Ry. Phonons and dynamical matrices were evaluated on one-dimensional grids along the $\hat{x}$-axis of the BZ containing $N_{\mathbf{q}}$ points. I used $N_{\mathbf{q}}$=10, 26 and 40. To test the dependence of the phonon frequencies on the grid, I calculated the phonon energies for a $\mathbf{q}$-point not contained in the uniform grids. In Tab. 2.4 the real phonon frequencies for this $\mathbf{q}$-point are compared with the ones obtained by Fourier interpolation of the IFC's calculated at $N_{\mathbf{q}}$=10, 26 and 40. I see that from 6^{th} to 12^{th} branch the IFC's interpolation is very accurate already using the smallest grid. By using denser grids a good agreement is obtained also for the lower branches. The phonon bands along the high symmetry line Γ-X are shown in Fig. 2.6.

As it can be seen in Fig. 2.6 there are two optical modes with frequencies around $\sim 3000\,cm^{-1}$, ν_7 and ν_8. These can be attributed to the stretching of the $C-H$ bonds. The number of such modes corresponds to the number of hydrogen atoms. These modes are also dispersionless indicating the independent nature of the vibrations corresponding to different $C-H$ bonds.

The other optical modes are located between 750 and 1500 cm^{-1}. That one around 1500 cm^{-1}, (ν_6) is assigned to the in-phase $C=C$ stretch mode

The ν_5 mode consists primarily of the $C\hat{C}C$ deformation, and the $C=C$ bond stretching. The displacements of C atoms are nearly perpendicular to the chain axis.

The ν_4 mode is connected to the $C-H$ in plane bending vibrations while ν_7 and ν_8 are two of plane modes.

The first four modes at lower energies appearing in Fig. 2.6 are the acoustic modes: three of them are related to the translational symmetry and one extra acoustic mode (not present in bulk systems) is related to the rotational invariance around

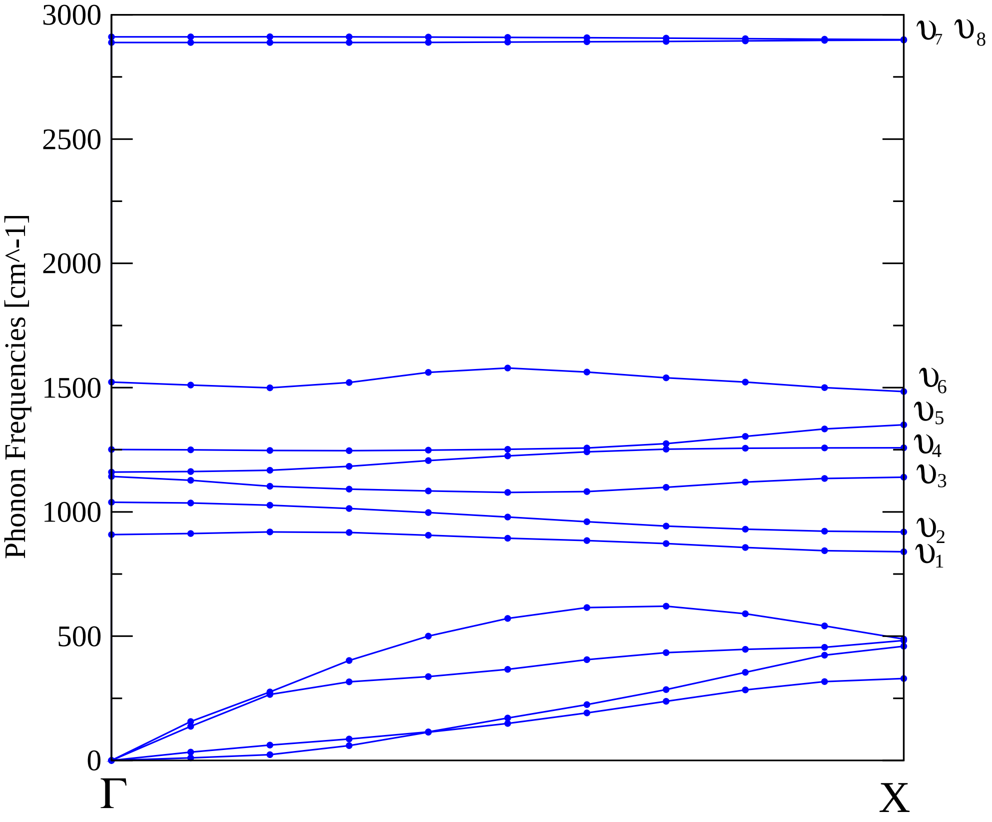

Figure 2.6: Phonon dispersion curves of *trans*-polyacetylene calculated with 40 Ry as kinetic cutoff energy.

the polymer axis. The translational mode along the polymer axis and the rotational mode have a linear dispersion energy for $\mathbf{q} \rightarrow 0$. The last two modes, instead, have an energy dispersion proportional to q^2 and they correspond to translational modes which are orthogonal to the polymer axis.

2.3 Polyethylene

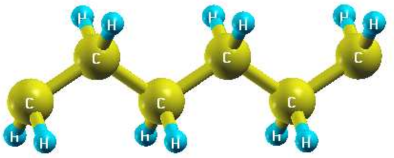

Figure 2.7: A segment of the polyethylene chain.

In σ-bonded polymers, the C-atoms are sp^3 hybridized, as in the polyethylene (PE) structure shown in Fig. 2.7, and each C-atom has four bonds. In such non-conjugated polymers, the electronic structure consists only of σ-bands. The large electron energy band gaps in σ-bonded polymers makes these polymers electrically insulating, and generally non-absorbing to visible light.

	r_{CC} (Å)	r_{CH} (Å)	θ_{CCC} (°)	θ_{HCH} (°)
Experimental	1.53	1.07	112	107.5
LDA	1.503	1.097	113.58	105.3

Table 2.5: Comparison between the experimental [17, 18] and calculated geometry (bond lengths and angles) of a polyethylene chain.

2.3.1 Ground state, phonons and electrons

Unlike in the case polyacetylene, PE shows only slight differences among the different geometries determined either by experiment or by theory. In my calculation I use the structure measured using x-ray diffraction [17, 18] whose bond lengths and angles are represented in Tab. 2.5. In addition I relaxed the atomic structure.

First I checked that the CC bond length effectively corresponds to the optimum one by varying the distance between the two carbon atoms around the experimental length, assumed to be the equilibrium one. To resolve such a small movements a high cutoff is needed (E_{cut}=60 Ry). The result is shown in Fig. 2.8.

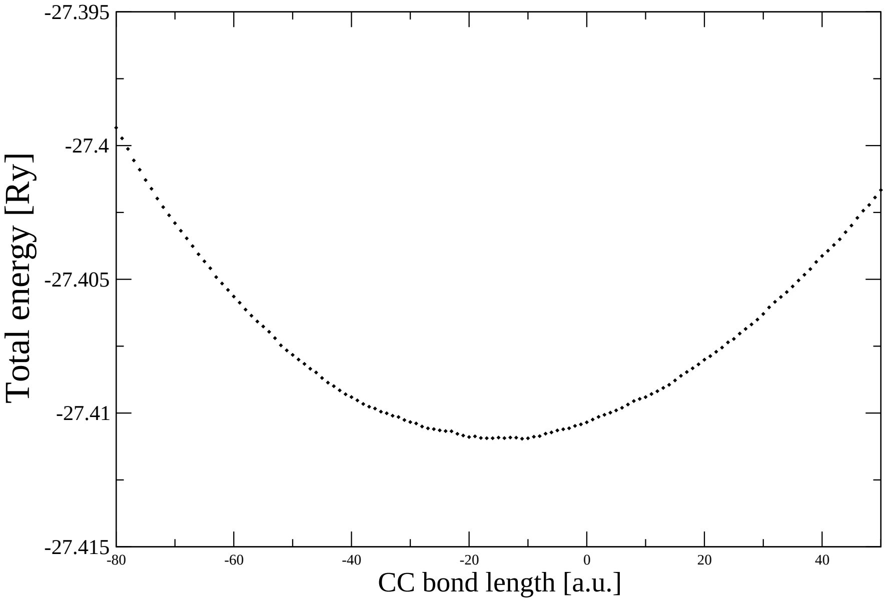

Figure 2.8: Calculated total energy versus C-C bond length of polyethylene.

Fitting this curve with a parabola, I found that the minimum of the energy corresponds to a $C - C$ bond length equal to 1.502 Å. The internal geometrical structure of the isolated polymer chain thus fixes the repetition length of the crystal unit cell, to be $\mathbf{a} = 2.51$ Å.

The electronic band structure and the phonon bands have been investigated following the very same strategy outlined in the case of the *trans*-polyacetylene.

Analogous convergence tests were performed for the energy cutoff. While E_{cut} is varied between 30 Ry and 60 Ry in steps of 5 Ry the volume of the unit cell is kept fixed. The unit cell is orthorhombic, centred in the origin of the axis with dimensions **a**=4.75 a.u., **b**=20 a.u., **c**=20 a.u.. The integration over the BZ is done with a uniform mesh of 10 points. I found that if $E_{cut} = 40Ry$ the total energy converges within an accuracy of 0.04 eV. At this cutoff the electronic gap is 6.57 eV at Γ. It represents a converged value within a range of accuracy of 0.03 eV.

The same analysis has been carried out for the convergence on the sides **b** and **c** of the unit cell, at E_{cut}=40 Ry. I found that if **b** and **c** equal 20 a.u. the total energy converges within an accuracy range of 0.0002 eV. At that volume the electronic gap is 6.57 eV at Γ. It represents a converged value within a range of accuracy of 0.07 eV.

The electronic and phononic band structures at 40 Ry are that shown in Figs. 2.9 and 2.10 respectively.

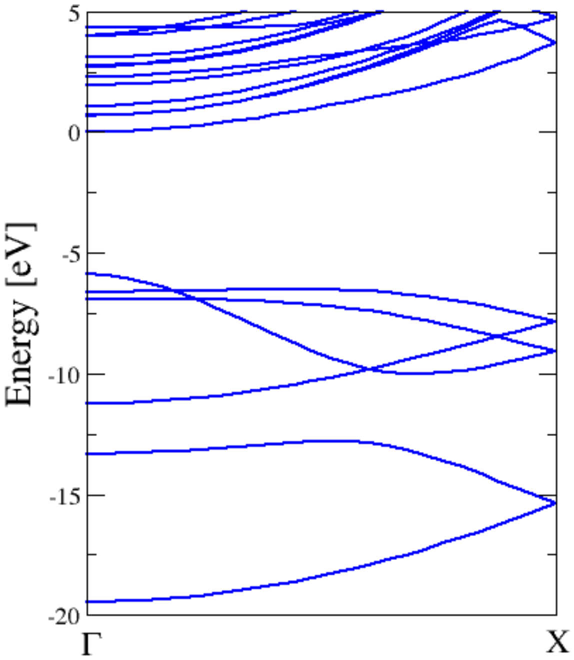

Figure 2.9: Electronic band structure of polyethylene.

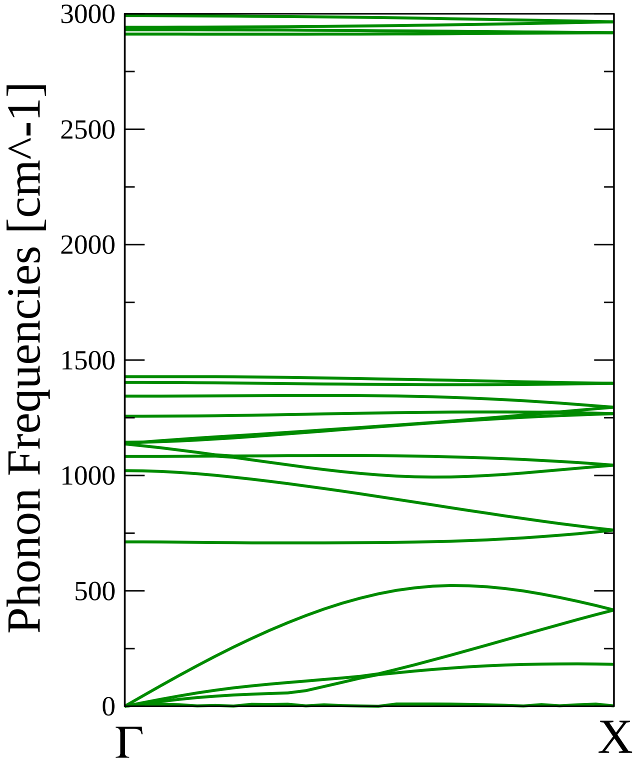

Figure 2.10: Phonon band structure of polyethylene.

2.4 Acoustic phonons and the bending of polymers

Long wavelength phonons play a delicate role in carbon based nanostructures. The tendency to bend and to curl in graphite layers is well documented [19, 20, 21].

Molecular dynamics simulations [22], in fact, demonstrated that acoustic phonon modes tend to close graphite sheets to form nanotubes. The relevant point is that the energy barrier against the curvature is $0.3\,eV$. It means that already at $T \sim 2-3000\,K$ such a barrier can be overcome by thermal fluctuations. This has been confirmed by studying the vibrational spectra of graphene and looking for the presence of a particular class of vibrational eigenmodes having a symmetry tending to fold the flat sheet into a cylinder, as shown in Fig. 2.11.

The eigenmodes responsible for the bending are also present in polymers. Indeed, the experimental growth of long straight polymer chains, turns out to be quite difficult.

In the present context the tendency of the chain to bend induces uncontrollable quasiparticle corrections that explode as the temperature is increased. As I consider straight chains the acoustic phonons will be neglected.

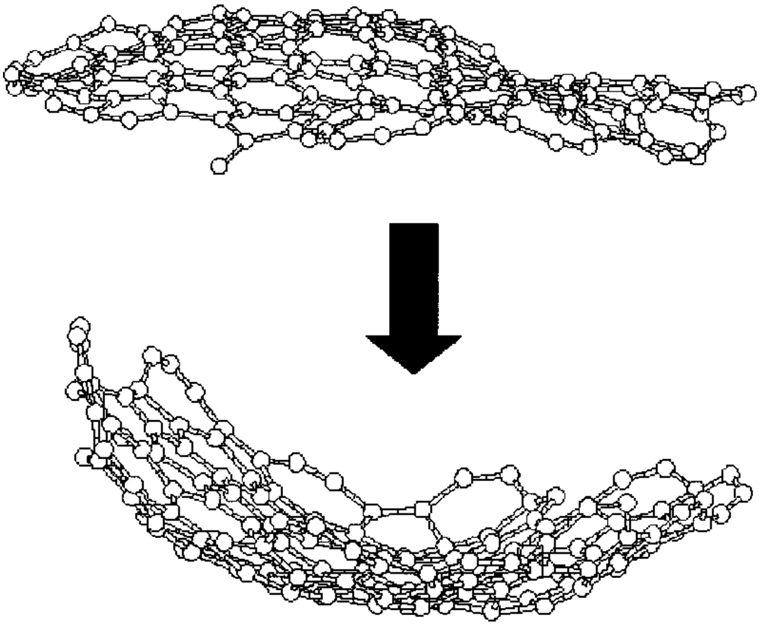

Figure 2.11: Snapshots of a molecular dynamics simulations of a graphite layer at $T = 4000\,K$. The lower configuration is taken at about $4\,ps$ after the upper one. From Ref. [22].

2.5 A random walker for atoms to reveal a huge electronic instability

In the BOA the dynamic of atoms oscillating in their potential walls is mapped into that of quantum harmonic oscillators. Each atom oscillates around its equilibrium position and at the same time it is part of the collective oscillations, the phonons. The ground state wavefunction of a three-dimensional harmonic oscillator is a Gaussian function

$$G_s(\vec{r}) = Ne^{-C(\vec{r})}, \tag{2.25}$$

where N is a normalization factor and $C(\vec{r})$ is a generic conical function.

Performing a thermal average over all phonons it is possible to calculate the atomic indetermination, as the square of the atomic displacements

$$\sigma^s_{ij}(T) = \langle u^s_i u^s_j \rangle = \sum_{\mathbf{q}\lambda} \frac{1}{2N_{\mathbf{q}\lambda} M_s \omega_{\mathbf{q}\lambda}} \vec{\epsilon}^{\,*}_i(\mathbf{q}\lambda/s)\vec{\epsilon}_j(\mathbf{q}\lambda/s)(2B(\omega_{\mathbf{q}\lambda}) + 1). \tag{2.26}$$

The indices i, j label the three directions x, y, z, while s labels the generic species. The atomic indetermination is obtained summing over all phonons, labeled by **q**-vector and the branch λ. σ^s_{ij} depends on the atom mass M_s, and it includes the scalar product of the polarization vectors. Phonon frequencies and polarization vectors are the eigenvalues and the eigenstates respectively of the Hessian operator defined by Eq. (2.8). σ^s_{ij} is a function of temperature, through the Bose function distribution

Trans-polyacetylene		
Conical axis C and H	C $a.u.$	H $a.u.$
$\hat{x}$	0.1	0.32
$\hat{y}$	0.07	0.21
$\hat{z}$	0.07	0.34

Polyethylene			
Conical axis C	C $a.u.$	H $a.u.$	Conical axis H
$\hat{x}$	0.1	0.32	$\hat{x}$
$\hat{y}$	0.08	0.21	$-0.54\hat{y} + 0.84\hat{z}$
$\hat{z}$	0.06	0.33	$0.84\hat{y} + 0.53\hat{z}$

Table 2.7: Atomic amplitudes Δ_i^s obtained by diagonalization of the σ_{ij}^s (T=0) matrices.

$B(\omega_{\mathbf{q}\lambda})$. Even if at $T = 0\,K$ there are no phonons and the Bose function vanishes, the atomic indetermination is different from zero. This is the zero point motion effect, an exclusively quantum effect.

The diagonalization of the σ_{ij}^s matrix provides the axis of the conical function $C(x, y, z)$. Physically they represent the directions along which the atoms can be maximally delocalized. Indeed if

$$\sigma_{ij}^s d_j^s = \Delta_i^s d_i^s, \tag{2.27}$$

Δ_i^s is the indetermination of the atomic species s along the direction defined by d_i^s.

The main ingredients I need to evaluate Eq. (2.26) can be obtained by a DFPT calculation, as it was shown in Sec. 2.1. The results for *trans*-polyacetylene and polyethylene are summarized in Tab. 2.7. Despite the conical axis are expected to lie along arbitrary directions, I found that in the case of *trans*-polyacetylene they are just along the polymer main axis, both for C and H. It means that $\sigma_{ij}^s(0)$ is already in a canonical form. The same happens to C in polyethylene, while the Gaussian associated to H has one axis coinciding with the $\hat{x}$ direction, while the other two orthogonal axis are rotated with respect to $\hat{y}$ axis of 32°.

The different values between the C and the H atoms are obviously due to the different masses. Particularly interesting is to compare these values with the typical bond lengths (see left panel of Fig. 2.2 and Tab. 2.5) of *trans*-polyacetylene and polyethylene. The relatively large values of Δ_i^s point to a possible important effect of the atom indetermination on the electronic levels. As a consequence the appropriate description of atoms is quantistic, where point atoms are replaced by a three-dimensional Gaussian probability centered in the equilibrium positions

$$G_s(\vec{r}) = \frac{1}{(2\pi)^{\frac{3}{2}} \Pi_i \sqrt{\sigma_{ii}^s}} e^{-\frac{1}{2}\left(\sum_{ij} \frac{r_i r_j}{\sigma_{ij}^s}\right)}. \tag{2.28}$$

The key point now, is how to investigate the potential effect of the giant zero point motion effect on the electronic levels. I would like to have a first, qualitative picture that links the quantum fluctuations of the atoms with the electronic levels. The easiest way is to use the frozen-phonon approach. In this approach the atoms are displaced of a small quantity and the corresponding electronic levels are calculated by performing a self-consistent Kohn-Sham calculation.

To simulate the zero point motion effect I used a Gaussian random walk. I generated N=10000 Gaussian distributed atomic configurations moving atoms around their equilibrium positions. The N configurations are generated by a Metropolis algorithm. The starting point is the system with atoms in their equilibrium position, whose geometry is shown in Fig 2.2 and Tab. 2.5. In this case the set of displacements is $\{\vec{u}_0\} = 0$.

As a first step the algorithm proposes a set of displacements $\{\vec{u}_1\}$ from the equilibrium position. The suggested total displacement is then

$$D = \{\vec{u}_1\} + previously\ accepted. \tag{2.29}$$

This proposal is "accepted" as the new configuration if a number r, randomly distributed in the $[0, 1]$ interval satisfies

$$r < G(\{\vec{u}_1\} + previously\ accepted)/G(previously\ accepted). \tag{2.30}$$

When this condition is satisfied, $\{\vec{u}_1\}$ is accepted. If such a condition was not satisfied instead, the displacement would be refused, the algorithm would retain the current configuration at time step $t - 1$. The result is a sampling of the atomic positions centered around the equilibrium one with variance $\vec{u}_s^2$.

A single point energy calculation (wavefunctions and charge density are calculated for a particular arrangements of nuclei) has been performed for each atomic configuration. The electronic structure is each time relaxed to a new configuration dictated by the current atomic positions. For this reason movements are adiabatic. A random-walker simulation is equivalent to consider only Γ-point movements, because a movement associated to a given atom is the same in all cells. Since each atomic displacement is independent on the others belonging to the monomer, I am considering decoupled and isolated harmonic oscillators. As the ground state wavefunction of an isolated harmonic oscillator is a Gaussian function the association of a Gaussian probability to each atom is justified in this context.

The aim of this analysis is to check how much the KS energy of each electronic state deviates with respect to the reference one, when the effect of zero point motion is introduced by hand. With this approach I am actually overestimating the zero point motion effect. Besides the broadening of the electronic levels following the atomic motions, I am also including a further broadening due to the fact that movements are chaotic: atom are *not* moved, in fact, respecting the phonon symmetries.

I have also considered the case of a standard deviation set by hand at $\sigma = 0.05 a.u.$. This "sharper" random walker is used to simulate the movements of the carbon atoms, only.

Both in the normal and sharp random-walker I evaluated the spectral function, as the probability that the KS energy of the electronic state $n\mathbf{k}$ is equal to an arbitrary energy ω:

$$A_{n\mathbf{k}}(\omega) = \frac{1}{N} \sum_{i=1}^{N} \delta(\omega - \epsilon_{n\mathbf{k}}(i)), \tag{2.31}$$

where the sum runs over all accepted atomic configurations. As a probability function it is obviously normalized to 1. Results for the first occupied band of *trans*-polyacetylene are summarized in Fig. 2.12.

The first noteworthy observation is that in most of the cases the spectral functions spread over a range of about 2 eV. It means that small atomic movements around equilibrium positions produce great changes in the single particle electronic energy. It is a first evidence for a strong coupling between electronic and atomic degrees of freedom, even at $T = 0\,K$, when the only zero point motion effect is taken into account.

When I associate a smaller indetermination to the atom, it is like if the electron saw a more massive atom with respect to the classical picture of point atoms. I can observe as a general trend that a sharper random walker produces distributions more symmetrically distributed. In the sharp random walker, indeed, atoms are strongly bounded to their equilibrium positions. In the standard random walker, instead, the SF's are, in general, non symmetric. I interpret this asymmetry as due to the deep modification of the electronic levels. Indeed the atomic movements seem to induce a severe rearrangement of the electronic levels that are represented by mixed packets of levels referred to the original, un-displaced geometry. These packets can be, in general, centered on a different energy that represents the most probable energy spanned by the electron during the Gaussian oscillations.

In conclusion, this simplified simulation, has revealed a giant renormalization of the electronic levels following the atomic motion. The purpose of the next chapter is to ground these preliminary results on a more rigorous theoretical basis.

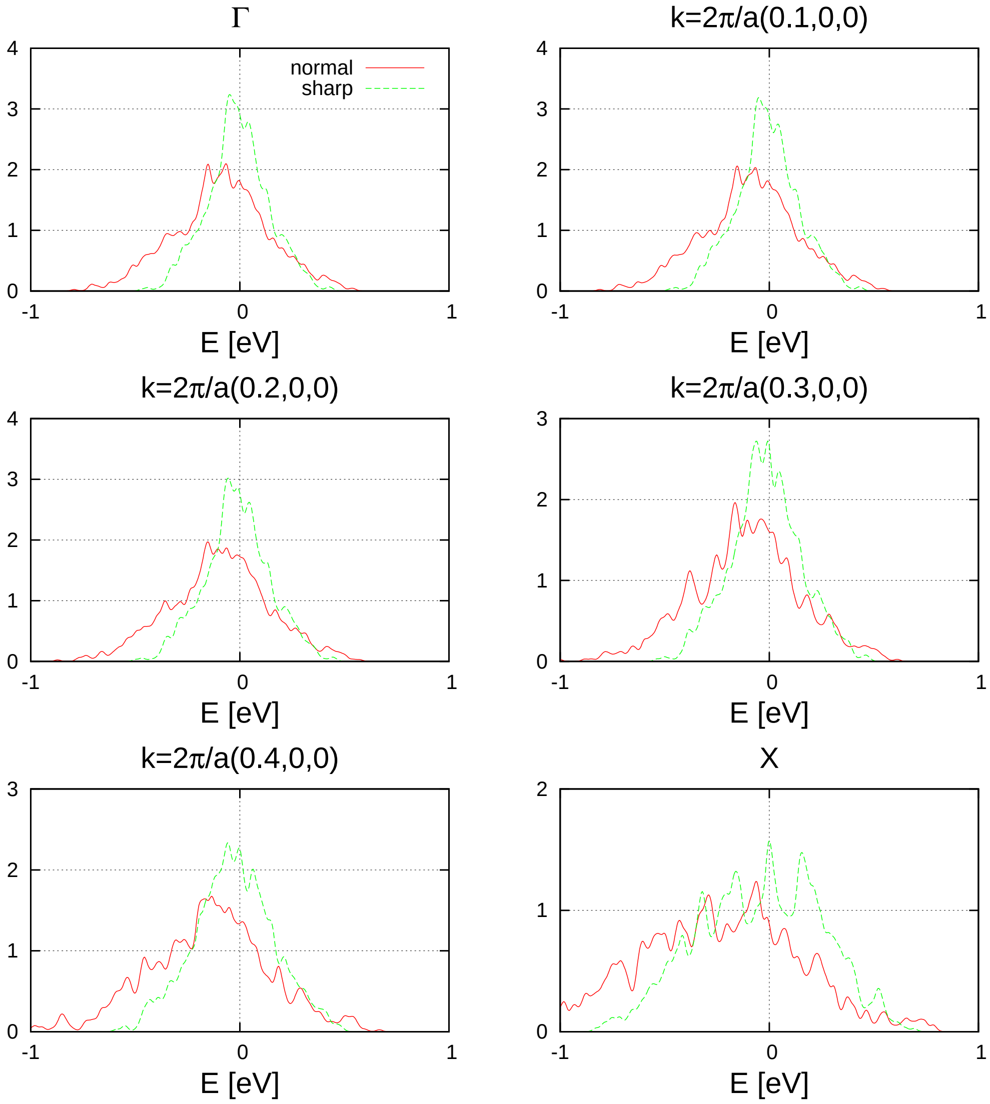

Figure 2.12: Spectral functions of the first occupied band obtained after a random walker simulation (red line) and after a sharper one (green line).

Bibliography

[1] P.D. De Cicco and F.A. Johnson, Proc. R. Soc. London, Ser. A **310**, 111 (1969)

[2] R. Pick, M.H. Cohen and R.M. Martin, Phys. Rev. B **1**, 910 (1970)

[3] P. Hohenberg e W. Kohn, Phys. Rev. B ,**136**, 864 (1964)

[4] W. Kohn e L. J. Sham, Phys. Rev. A,**140**, 1133 (1965)

[5] H. Hellmann, Einführung in die Quantenchemie (Deuticke, Leipzig) (1937)

[6] R.P., Feynman, Phys. Rev. **56**, 340 (1939)

[7] M. Lazzeri and F. Mauri Phys. Rev. Lett. **97**, 266407 (2006)

[8] R.E. Peierls *Quantum Theory of Solids* (Clarendon, Oxford, 1955)

[9] Quantum Espresso Home Page, http://www.quantum-espresso.org
P. Giannozzi and S. Baroni et al., J. Phys.: Condens. Matter **21**, 395502 (2009)

[10] J. Perdew and A. Zunger, Phys. Rev. B **23**, 5048 (1981)

[11] U. Von Barth and R. Car (unpublished); for a brief description of this method, see A. Dal Corso, S. Baroni, R. Resta, and S. de Gironcoli, Phys. Rev. B **47**, 3588 (1993).

[12] B. Kirtman, J.L. Toto, K.A. Robins and M. Hasan, J. Chem. Phys. **102**, 5350 (1995)

[13] H. Takeuchi, T. Harakawa, Y. Furakawa, I. Harada and H. Shirakawa, J. Mol. Struct. **158**, 179 (1987)

[14] H. Kuzmany, Phys. Stat. Sol. b **97**, 521 (1980)

[15] H. Shirakawa and S. Ikeda, J. Polym, **2**, 231 (1971)

[16] C.S. Yannoni and T.C. Clarke, Phys. Rev. Lett. **51**, 1191 (1983)

[17] H.M.M. Shearer, V. Vand, Acta Cryst. **9**, 379 (1956).

[18] P.W. Teare, Acta Cryst. **12**,294 (1959).

[19] D. Ugarte, Nature London **359**, 707 (1992).

[20] F.M. Banhart and P.M. Ajayan, Nature London **382**, 433 (1996).

[21] L. Boulanger, B. Andriot, M. Cauchetier, and F. Willaime, Chem. Phys. Lett. **234**, 227 (1995).

[22] M. Volpe and F. Cleri J. Chem. Phys. **115**, 3308 (2001)

Chapter 3

Polarons: ab–initio theories of electron–phonon interaction

The Born–Oppenheimer approximation (BOA) and the consequent decoupling of the atomic and electronic degrees of freedom, represents the basis for the majority of the ab–initio calculations. As a consequence, in these standard approaches the electronic and optical properties are calculated assuming the atoms frozen in their crystallographic positions. As a matter of fact the coupling of the electronic states with the lattice vibrations has been often undervalued. The most important aspect is that little, or not, valid motivations to this approximation are provided. Instead, even when $T \rightarrow 0$, atomic quantum fluctuations appear. Only by a careful analysis of the effects induced by the electron-phonon coupling it is possible to estimate the impact of the frozen atom approximation.

Indeed, the measured temperature dependence of the energy bands at a constant pressure derives partially from the renormalization of the band energies by electron-phonon coupling (EPC) and partially from the thermal expansion. The observed thermal shift of the electron energies in metals and semiconductors is typically larger by a factor of 5 than can be accounted for by the thermal expansion alone. The electron-phonon interaction besides being the largest effect is also the hardest one to evaluate.

The theory of EPC has attracted a large interest since 1951 [1], when Fan developed the theory of this effect. He calculated the electronic self-energy in a simple model (Debye phonons, parabolic bands and only evaluating the intraband terms) by retaining terms up to the second order in the electron-phonon interaction . The model yields a decreasing gap with increasing T, in agreement with the experiment for Ge and Si [2],[3]. On the other hand Antoncik [4] and other authors [5] found a reasonable agreement with the experiments over quite a range of temperature, by the only inclusion of the Debye-Waller correction.

It was believed for many years that Debye-Waller and Fan theories were equivalent, i.e. either one or the other could be used. Instead in the 70's and 80's a new awareness became widespread [6]. In the case of diamond–type semiconductors both terms are needed. The inclusion of the solely Debye-Waller term overestimates the variation of the energy gap with the temperature. When the Fan term is added the agreement between theory and experiment improves.

The purpose of the present chapter is to review the second order adiabatic theory which rigorously gives both the self-energy and the Debye-Waller corrections. The condition of translational invariance is used to transform the Debye-Waller term in a form closely related to the self-energy correction. It will be also evident that the interband terms are by no means unimportant as instead was assumed for a long time.

In Sec. 3.1 the Heine Allen Cardona approach to polarons is introduced, following Refs. [7]. In Sec. 3.1.1 I will retrace some of the results that have been obtained using this approach. In particular a first–principle study relied on the HAC technique has been used [8] to pursue successfully the temperature–dependence of the optical spectrum of Silicon in a full ab–initio manner. This study will be reviewed in Sec. 3.1.2.

Sec. 3.2 focuses on the results I obtained when the HAC approach is applied to *trans*-polyacetylene. I will provide and discuss the calculations for the temperature–dependent energy shifts of the electronic states produced by the electron-phonon interaction. In particular I will show how the HAC approach leads, in this case, to pronounced and uncontrollable numerical instabilities, related to the large polaronic corrections.

A further step will be to evaluate the electron–phonon self-energy (Sec. 3.3.1) within the Many–Body Perturbation Theory framework. Moreover in the same section I will show that the thermal shift of the electron energies within the many-body approach, reduces to the static HAC approach in the *on mass shell* and the adiabatic limits.

3.1 The Heine–Allen–Cardona approach

We consider a crystal constituted by atoms of different species. The generic atom position is $\mathbf{R}_{Is}^{(0)} + \mathbf{u}_{Is}$, with I the cell index and s the species. $\mathbf{R}_{Is}^{(0)}$ is the equilibrium position and $\mathbf{u}_{Is}$ the corresponding displacement. As the displacements are usually small, one can expand H_{scf} (Eq. (2.12)) in powers of $\mathbf{u}_{Is}$. The two leading terms in the Taylor expansion are,

$$\mathcal{H}_1 = \sum_{Is} \mathbf{u}_{Is} \cdot \vec{\nabla}_{Is} V_{scf}(\mathbf{r} - \mathbf{R}^{(0)}_{Is}), \tag{3.1}$$

$$\mathcal{H}_2 = \sum_{\substack{Is \\ Js'}} \mathbf{u}_{Is}\mathbf{u}_{Js'} \cdot \vec{\nabla}_{Is}\vec{\nabla}_{Js'} V_{scf}(\mathbf{r} - \mathbf{R}^{(0)}_{Is}). \tag{3.2}$$

V_{scf} is the Kohn–Sham potential defined by the Eq. (1.35), evaluated in the atomic equilibrium positions (BOA), which form the crystal periodic potential. The solution of the electronic Hamiltonian corresponding to V_{scf}, gives the Kohn–Sham states $\mid n\mathbf{k}\rangle$, and the band energies $\epsilon_{n\mathbf{k}}$, respectively eigenstates and eigenvalues of H_{scf}.

The adiabatic approximation implies that the time dependence of $\mathbf{u}_{Is}$ is neglected and treats $\mathbf{u}_{Is}$ as a static operator. This makes possible to calculate the perturbed electron energy $E_{n\mathbf{k}}(\{\mathbf{u}_{Is}\})$ of the state $\mid n\mathbf{k}\rangle$ in the presence of a configuration $\{\mathbf{u}_{Is}\}$ of static lattice displacements. To second order in $\mathbf{u}_{Is}$ the result is

$$E_{n\mathbf{k}}(\{\mathbf{u}_{Is}\}) = \epsilon_{n\mathbf{k}} + \langle n\mathbf{k} \mid (\mathcal{H}_1 + \mathcal{H}_2) \mid n\mathbf{k}\rangle + {\sum_{n'\mathbf{k}'}}' \frac{|\langle n'\mathbf{k}' \mid \mathcal{H}_1 \mid n\mathbf{k}\rangle|^2}{\epsilon_{n\mathbf{k}} - \epsilon_{n'\mathbf{k}'}}, \tag{3.3}$$

where the prime symbol in the summation indicates that the term $n'\mathbf{k}' = n\mathbf{k}$ is omitted.

The corresponding change in energy of an electronic state $\mid n\mathbf{k}\rangle$ of unperturbed energy $\epsilon_{n\mathbf{k}}$ is

$$\Delta E_{n\mathbf{k}}(\{\mathbf{u}_{Is}\}) = \sum_{\substack{\alpha Is, \\ \beta Js'}} \left\{ \frac{1}{2} \langle n\mathbf{k} \mid \frac{\partial^2 V_{scf}}{\partial R_{\alpha,Is} \partial R_{\beta,Js'}} \mid n\mathbf{k}\rangle + \right.$$

$$\left. + {\sum_{n'\mathbf{k}'}}' \frac{1}{\Delta_{n\mathbf{k}n'\mathbf{k}'}} \langle n\mathbf{k} \mid \frac{\partial V_{scf}}{\partial R_{\alpha,Is}} \mid n'\mathbf{k}'\rangle \langle n'\mathbf{k}' \mid \frac{\partial V_{scf}}{\partial R_{\beta,Js'}} \mid n\mathbf{k}\rangle \right\} u_{\alpha,Is} u_{\beta,Js'}, \tag{3.4}$$

where

$$\Delta_{n\mathbf{k}n'\mathbf{k}'} = \epsilon_{n\mathbf{k}} - \epsilon_{n'\mathbf{k}'}. \tag{3.5}$$

The first order correction from $\mathcal{H}_1$ is dropped, because the thermal average over the ensemble of thermal displacements will cause $\langle \mathbf{u}_{Is}\rangle$ to vanish in the harmonic approximation.

It must be observed that the terms in Eq. (3.4) correspond to Debye-Waller and self-energy corrections, in order of appearance. The second correction is equivalent to the Fan's theory [1].

The subscripts $\alpha, \beta, ...$ denote Cartesian components which are summed when repeated. $\frac{\partial V_{scf}}{\partial R_{\alpha,Is}}$ is the change in the electron–lattice potential per unit displacement of the atom Is in the α direction. It is self–consistently calculated for any variation of the electronic charge accompanying an atomic displacement.

The first term of Eq. (3.4) arises from the second–order electron-phonon coupling, treated within the first–order perturbation theory, while the second term is first–order electron-phonon coupling, within the second–order perturbation theory.

We will now introduce the following short notation

$$\Delta^{Is}_{\alpha\beta}(n\mathbf{k}) \equiv \langle n\mathbf{k} \mid \nabla_{\alpha Is,\beta Is} V_{scf} \mid n\mathbf{k}\rangle, \tag{3.6}$$

$$\Gamma^{Is}_{\alpha}(n\mathbf{k}n'\mathbf{k}') \equiv \langle n\mathbf{k} \mid \nabla_{\alpha Is} V_{scf} \mid n'\mathbf{k}'\rangle, \tag{3.7}$$

which allows to re–write Eq. (3.4) in a more compact and suitable form

$$\begin{aligned} \Delta E_{n\mathbf{k}}(\{\mathbf{u}_{Is}\}) \;=\;& \underbrace{\sum_{\substack{\alpha Is,\\ \beta Js'}} \frac{1}{2}\Delta^{Is}_{\alpha\beta}(n\mathbf{k}) u_{\alpha,Is} u_{\beta,Is} +}_{\Delta E^{DW}_{n\mathbf{k}}} \\ &+ \underbrace{\sum_{n'\mathbf{k}'}{}' \frac{1}{\Delta_{n\mathbf{k}n'\mathbf{k}'}} \Gamma^{Is}_{\alpha}(n\mathbf{k}n'\mathbf{k}') \Gamma^{Js'}_{\beta}(n'\mathbf{k}'n\mathbf{k}) u_{\alpha,Is} u_{\beta,Js'}\,.}_{\Delta E^{Fan}_{n\mathbf{k}}} \end{aligned} \tag{3.8}$$

The definition given by Eq. (3.6) assumes the pseudo potential to be local: only diagonal terms ($s = s'$) of the operator $\partial^2 V_{scf}$ are considered. Such a condition is fullfilled only if the Hamiltonian depends on the atomic positions only within a *rigid ions* scheme. The non diagonal terms, in fact, would vanish in this case. Within DFPT, instead, the variation of the ionic potential felt by electrons is screened by the inverse of the dielectric function, which in turns depends implicitly on the atomic positions.

Non–diagonal Debye-Waller contributions (NDDW) are in principle non zero, in the general case. In extended systems the efficient screening weakens the implicit dependence of V_{scf} on the atomic positions. The reason is that the plasmon oscillations are not appreciably influenced by a tiny atomic rearrangement. P. Boulanger [9] has shown that NDDW contributions play a crucial role in molecules, where the screening is poor. In this thesis I will study infinite 1D chains where plasmons can indeed be excited. As a consequence I assume the electronic screening to be large enough to reduce substantially the NDDW corrections. Therefore, in the following, NDDW corrections will be neglected.

We now investigate the implication of the translational invariance by noticing that if every atom is further displaced by a fixed amount u_α, the energy must not change

$$\Delta E_{n\mathbf{k}}(\{u_{\alpha,Is}+u_\alpha\}) = \Delta E_{n\mathbf{k}}(\{u_{\alpha,Is}\}). \tag{3.9}$$

Then Eqs. (3.8) and (3.9) impose the following identity relating the matrix elements of ∂V_{scf} and $\partial^2 V_{scf}$ appearing in Eq. (3.4)

$$\begin{aligned} 0 &= \sum_{\substack{\alpha Is,\\ \beta Js'}} \left\{ \frac{1}{2}\Delta^{Is}_{\alpha\beta}(n\mathbf{k})(u_{\alpha,Is}+u_\alpha)(u_{\beta,Is}+u_\beta) + \right. \\ &+ \left. \sum_{n'\mathbf{k}'}{}' \frac{1}{\Delta_{n\mathbf{k}n'\mathbf{k}'}} \Gamma^{Is}_{\alpha}(n\mathbf{k}n'\mathbf{k}')\Gamma^{Js'}_{\beta}(n'\mathbf{k}'n\mathbf{k})(u_{\alpha,Is}+u_\alpha)(u_{\beta,Js'}+u_\beta) \right\}. \end{aligned} \tag{3.10}$$

Eq. (3.10) is equivalent to the *acoustic sum rule* of lattice dynamics [10] and it guarantees that Eq. (3.8) vanishes as $\mathbf{q} \to 0$, if $u_{\alpha,Is}$ represents a long–wavelength acoustic phonon, as argued by Zeyher [11] and in Ref. [12].

From Eq. (3.10) it is possible to get two conditions, coming from the first and the second order terms in $\mathbf{u}_{Is}$. The first order one allows to re–write the Debye-Waller correction in a form similar to the self-energy correction.

Grouping terms with u_α, and those with u_β, renaming β in α in the term multiplying u_β, and observing that $\Delta^{Is}_{\alpha\beta}(n\mathbf{k}) = \Delta^{Is}_{\beta\alpha}(n\mathbf{k})$, the first order in $\mathbf{u}_{Is}$ condition can be re–written as

$$\begin{aligned} \Delta^{Is}_{\alpha\beta}(n\mathbf{k})\ \ u_{\beta,Is} \ &+\ \frac{1}{\Delta_{n\mathbf{k}n'\mathbf{k}'}} \left[\left(\sum_{Is} \Gamma^{Is}_{\alpha}(n\mathbf{k}n'\mathbf{k}') \right) \Gamma^{Js'}_{\beta}(n'\mathbf{k}'n\mathbf{k}) u_{\beta,Js'} \right. \\ &+ \left. \Gamma^{Is}_{\beta}(n\mathbf{k}n'\mathbf{k}') \left(\sum_{Js'} \Gamma^{Js'}_{\alpha}(n'\mathbf{k}'n\mathbf{k}) \right) u_{\beta,Is} \right] = 0, \end{aligned} \tag{3.11}$$

where repeated indexes are summed. Eq. (3.11) allows to derive the $\Delta^{Is}_{\alpha\beta}$ matrix elements appearing in the Debye-Waller energy correction, in terms of the gradients Γ^{Is}_{α}. Both types of correction now appear to be of the second order in V_{scf}; a result which was not transparent at all in the original form (Eq. (3.4)). This close relation was obscured by the fact that it involves different powers of V_{scf}.

The temperature dependent band energy corrections $\Delta E_{n\mathbf{k}}(T)$ can be obtained by performing a thermal average of $E_{n\mathbf{k}}(\{\mathbf{u}_{Is}\})$ over the ensemble of displacements. In order to do that, the factor $\langle u_{\alpha,Is} u_{\beta,Is} \rangle$ is evaluated resorting to the Fourier transform of the atomic displacements in the phonon representation

$$u_{\alpha,Is} = \sum_{\mathbf{q}\lambda} \left(\frac{1}{2M_s \omega_{\mathbf{q}\lambda} N_{\mathbf{q}}} \right)^{\frac{1}{2}} e^{i\mathbf{q}\cdot(\mathbf{R}_I+\tau_s)} \epsilon_\alpha(\mathbf{q}\lambda/s)(b^\dagger_{-\mathbf{q}\lambda} + b_{\mathbf{q}\lambda}). \tag{3.12}$$

M_s is the mass of the s^{th} atomic species, in the unit cell at the position τ_s, N is the number of transferred momenta $\mathbf{q}$, $\epsilon_\alpha(\mathbf{q}\lambda/s)$ are the polarization vectors, and $b^\dagger_{-\mathbf{q}\lambda}$ and $b_{\mathbf{q}\lambda}$ are the bosonic creation and annihilation operators. Performing the thermal average implies to evaluate $\langle(b^\dagger_{-\mathbf{q}\lambda} + b_{\mathbf{q}\lambda})(b^\dagger_{\mathbf{q}\lambda} + b_{-\mathbf{q}\lambda})\rangle$ in order to get the matrix elements

$$\langle u_{\alpha,Is} u_{\beta,Is}\rangle = \sum_{\mathbf{q}\lambda} \frac{1}{2M_s\omega_{\mathbf{q}\lambda}N_{\mathbf{q}}} \epsilon^*_\alpha(\mathbf{q}\lambda/s)\epsilon_\beta(\mathbf{q}\lambda/s)\left(2B(\omega_{\mathbf{q}\lambda})+1\right), \tag{3.13}$$

where $B(\omega_{\mathbf{q}\lambda})$ is the Bose function distribution. The elements on the diagonal are the atomic vibrational amplitudes (see Sec.2.5).

To get to the final result for the energy correction some further steps must be taken. We can group the products between the matrix elements $\Gamma^{Is}_\alpha(n\mathbf{k}n'\mathbf{k}')$ and the atomic displacements $u^*_{\alpha,Is}$ appearing in Eq. (3.8), using Eq. (3.12)

$$\begin{aligned} &\textstyle\sum_{\alpha Is} \Gamma^{Is}_\alpha(n\mathbf{k}n'\mathbf{k}')u_{\alpha,Is} = \\ &\textstyle\sum_{\alpha Is}\langle n\mathbf{k} \mid e^{-i\mathbf{q}\cdot\mathbf{R}_I}\nabla_{\alpha Is}V_{scf} \mid n'\mathbf{k}'\rangle \displaystyle\sum_{\mathbf{q}\lambda}\left(\frac{1}{2M_s\omega_{\mathbf{q}\lambda}N_{\mathbf{q}}}\right)^{\frac{1}{2}} e^{-i\mathbf{q}\cdot\tau_s}\epsilon^*_\alpha(\mathbf{q}\lambda/s)(b^\dagger_{\mathbf{q}\lambda}+b_{-\mathbf{q}\lambda}). \end{aligned} \tag{3.14}$$

By using the Bloch's theorem we get

$$\begin{aligned} &\textstyle\sum_{\mathbf{k}'}\sum_{\alpha Is} \Gamma^{Is}_\alpha(n\mathbf{k}n'\mathbf{k}')u_{\alpha,Is} = \\ &\textstyle\sum_{\alpha s}\langle n\mathbf{k} \mid \nabla_{\alpha s}V_{scf} \mid n',\mathbf{k}+\mathbf{q}\rangle \displaystyle\sum_{\mathbf{q}\lambda}\left(\frac{1}{2M_s\omega_{\mathbf{q}\lambda}N_{\mathbf{q}}}\right)^{\frac{1}{2}} e^{-i\mathbf{q}\cdot\tau_s}\epsilon^*_\alpha(\mathbf{q}\lambda/s)(b^\dagger_{\mathbf{q}\lambda}+b_{-\mathbf{q}\lambda}). \end{aligned} \tag{3.15}$$

At this point we can define

$$\left(g^{\mathbf{q}\lambda}_{n'n\mathbf{k}}\right)^* = \sum_{\alpha s}\langle n\mathbf{k} \mid \nabla_{\alpha s}V_{scf} \mid n',\mathbf{k}+\mathbf{q}\rangle \sum_{\mathbf{q}\lambda}\left(\frac{1}{2M_s\omega_{\mathbf{q}\lambda}N_{\mathbf{q}}}\right)^{\frac{1}{2}} e^{-i\mathbf{q}\cdot\tau_s}\epsilon^*_\alpha(\mathbf{q}\lambda/s). \tag{3.16}$$

The $g^{\mathbf{q}\lambda}_{n'n\mathbf{k}}$ factors describe the probability amplitude that an electron scatters from $\mathbf{k} \rightarrow \mathbf{k}'$ with the emission or the absorption of a phonon of transferred momentum $\mathbf{q}$ and branch λ. These electron-phonon matrix elements can be obtained from the first order derivative of the self–consistent potential V_{scf} defined by Eq. (2.14), with respect to atomic displacements $u_{\alpha,Is}$ for the s^{th} atom in lattice position $\mathbf{R}_{Is}$. Moreover it is possible to further simplify the self-energy term by using completeness relations involving polarization vectors.

By using a similar procedure to the one that leads to Eq. (3.15) we can work out the Debye-Waller contribution to Eq. (3.8). This can be observed when the matrix element $\Delta^{Is}_{\alpha\beta}$, gathered from the condition of translational invariance, Eq. (3.11), is inserted in Eq. (3.8). The $\Delta^{Is}_{\alpha\beta}(n\mathbf{k})u_{\alpha,Is}u_{\beta,Is}$ factor can be simplified and written in a more compact form when we define

$$\begin{aligned}\Lambda^{\mathbf{q}\lambda}_{nn'\mathbf{k}} &= 2\Re\left[\sum_{\alpha\beta}\left(\sum_{s}\langle n\mathbf{k} \mid \nabla_{\alpha s}V_{scf} \mid n'\mathbf{k}\rangle\right)\cdot\right.\\ &\left.\cdot\left(\sum_{Is}\langle n'\mathbf{k} \mid \nabla_{\beta Is}V_{scf} \mid n\mathbf{k}\rangle\frac{\epsilon^*_{\alpha}(\mathbf{q}\lambda/s)\epsilon_{\beta}(\mathbf{q}\lambda/s)}{2M_s\omega_{\mathbf{q}\lambda}N_{\mathbf{q}}}\right)\right].\end{aligned} \tag{3.17}$$

Using Eq. (3.17) we get to the final expression for the thermal shift

$$\Delta E_{n\mathbf{k}}(T) = \sum_{\mathbf{q}\lambda}\frac{1}{N_{\mathbf{q}}}\sum_{n'}\left[\frac{\mid g^{\mathbf{q}\lambda}_{n'n\mathbf{k}}\mid^2}{\epsilon_{n\mathbf{k}} - \epsilon_{n'\mathbf{k}'}} - \frac{1}{2}\frac{\Lambda^{\mathbf{q}\lambda}_{nn'\mathbf{k}}}{\epsilon_{n\mathbf{k}} - \epsilon_{n'\mathbf{k}}}\right](2B(\omega_{\mathbf{q}\lambda}) + 1)\,, \tag{3.18}$$

where squared electron-phonon matrix elements appear together with a sum over all energy bands weighted by their energy denominators. $\Delta E_{n\mathbf{k}}(T)$ can be also rewritten in terms of a generalized Eliashberg function $g^2F_{n\mathbf{k}}(\omega)$

$$\Delta E_{n\mathbf{k}}(T) = \int d\omega g^2F_{n\mathbf{k}}(\omega)\left[B(\omega_{\mathbf{q}\lambda}) + \frac{1}{2}\right], \tag{3.19}$$

with $B(\omega_{\mathbf{q}\lambda}) = (e^{\beta\omega} - 1)^{-1}$, being the Bose occupation function. The complex $g^2F_{n\mathbf{k}}(\omega)$ function is defined by

$$g^2F_{n\mathbf{k}}(\omega) = \sum_{\mathbf{q}\lambda}\frac{\partial E_{n\mathbf{k}}}{\partial B(\omega_{\mathbf{q}\lambda})}\delta(\omega - \omega_{\mathbf{q}\lambda}), \tag{3.20}$$

where the sum is extended over all phonons $\{\mathbf{q}\lambda\}$.

It is clear that self-energy and Debye-Waller terms will be similar in order of magnitude. Both of them are cast in the form of interband transitions in Eq. (3.18). Since several calculations showed that also Debye-Waller gives a large contribution, the approximation introduced by Fan, of only considering the intraband terms in self-energy, can no longer be justified.

Following the Heine–Allen–Cardona (HAC) formulation it is possible to calculate the energy renormalization of state $\mid n\mathbf{k}\rangle$ due to the electron-phonon interaction using Eq. (3.18). When these shifts are evaluated for metals, or in general for systems where the typical energy differences $\mid \epsilon_{n\mathbf{k}} - \epsilon_{n'\mathbf{k}+\mathbf{q}} \mid$ are comparable to the phonon frequencies $\omega_{\mathbf{q}\lambda}$, a correction to the Fan term appears

$$\begin{aligned}\Delta E^{Fan}_{n\mathbf{k}}(T) &= \sum_{n'\mathbf{q},\lambda}\frac{\mid g^{\mathbf{q},\lambda}_{n'n\mathbf{k}}\mid^2}{N_{\mathbf{q}}}\left[\frac{(2B(\omega_{\mathbf{q}\lambda}) + 1)(\epsilon_{n\mathbf{k}} - \epsilon_{n'\mathbf{k}+\mathbf{q}})}{(\epsilon_{n\mathbf{k}} - \epsilon_{n'\mathbf{k}+\mathbf{q}})^2 - {\omega_{\mathbf{q}\lambda}}^2}+\right.\\ &+ \left.\frac{(1 - 2f_{n'\mathbf{k}+\mathbf{q}})\omega_{\mathbf{q}\lambda}}{(\epsilon_{n\mathbf{k}} - \epsilon_{n'\mathbf{k}+\mathbf{q}})^2 - {\omega_{\mathbf{q}\lambda}}^2}\right].\end{aligned} \tag{3.21}$$

The Debye-Waller correction, instead, does not change. So finally we get

$$\Delta E_{n\mathbf{k}}(T) = \Delta E^{Fan}_{n\mathbf{k}}(T) + \frac{1}{2}\frac{\Lambda^{\mathbf{q},\lambda}_{nn'\mathbf{k}}(2B(\omega_{\mathbf{q}\lambda})+1)}{\epsilon_{n\mathbf{k}}-\epsilon_{n'\mathbf{k}}}. \tag{3.22}$$

It can be verified that in the $\omega_{\mathbf{q}\lambda}$ going to zero limit, Eq. (3.22) becomes the expression for the energy corrections seen in Eq. (3.18). As discussed in Sec. 3.3.1 Eq. (3.21) can be obtained within the many-body perturbation theory scheme.

3.1.1 Polaronic Effects in semiconductors: bulks and nanostructures

In this section I will review some applications of the HAC approach to the calculations of these properties in bulks like Ge, Si and Diamond, in nanostructures like Carbon Nanotubes and a layered material, hexagonal–BN.

Germanium, Silicon and Diamond

The temperature dependence of the indirect gaps of Ge and Si has been known for half a century [14]. In one of the seminal paper of Allen and Cardona [6] the HAC approach has been applied to Silicon and Germanium. The corresponding T–dependence of the $\mathbf{k} = 0$ states near the band gap is shown in Fig. 3.1. The $T \to 0$ limit of Fig. 3.1 highlights the zero point motion effect. The electronic gap is reduced by the electron-phonon coupling even at $T = 0\,K$.

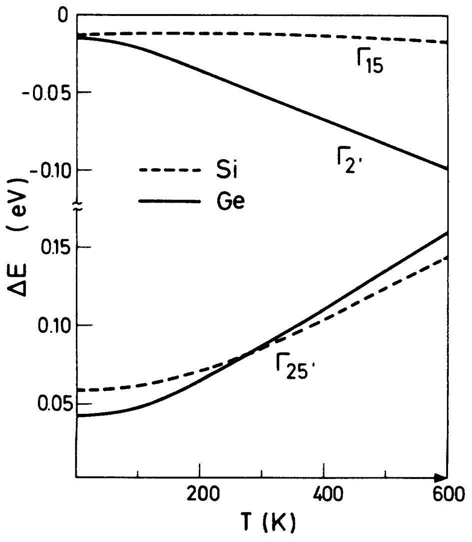

Figure 3.1: Temperature dependence of the thermal shift $\Delta E_{n\mathbf{k}}(T)$ for few bands at $\mathbf{k} = 0$ in silicon and germanium. From Ref. [6].

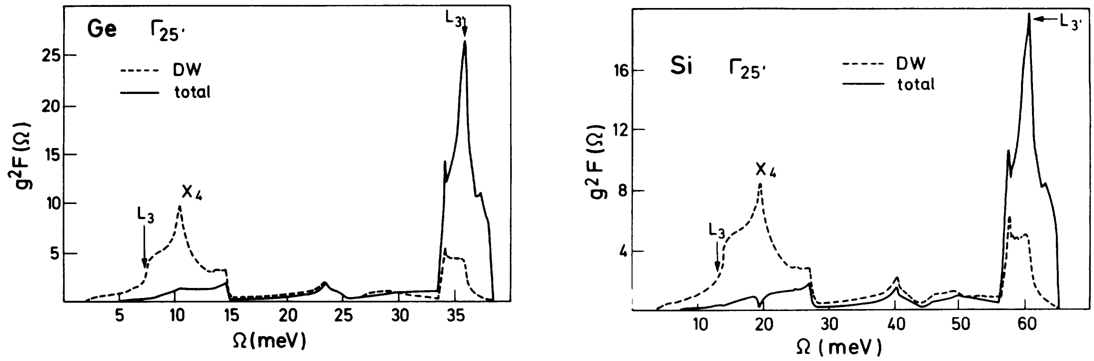

Figure 3.2: Eliashberg function $g^2F_{n\mathbf{k}}(\omega)$ of Ge (left panel) and Si (right panel) for a valence state at $\mathbf{k} = 0$. From Ref. [6].

In this work Allen and Cardona also calculate the generalized Eliashberg function, shown in Fig. 3.2. From Fig.3.2 it is clear that the DW contribution is of the same order of magnitude of the Fan term.

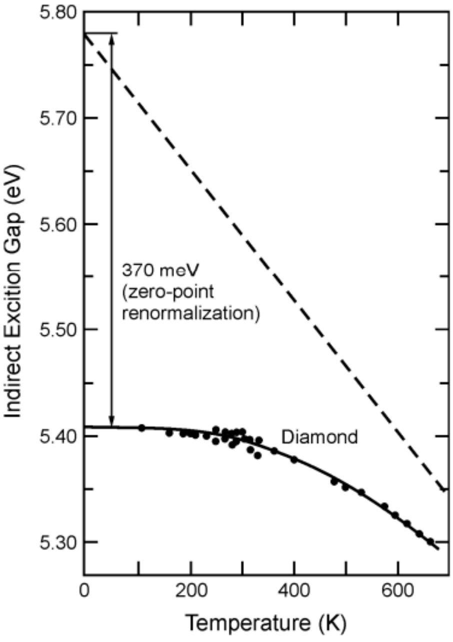

Figure 3.3: Optical gap of Diamond as a function of temperature. The dots are the experimental values fitted by the solid line. The dashed line is the asymptotic behaviour at high temperatures extracted from the fit. The extrapolation at $T = 0\,K$ gives the unrenormalized band gap. The difference between the intercepts with the vertical axis, gives the zero–point renormalization. From Ref. [19].

In contrast to Si and Ge, diamond has a much larger Debye temperature ($\sim 1900\,K$). Therefore electron-phonon corrections would be expected to be larger as $T \to 0$. The gap renormalization is estimated to be 370 meV, as shown in Fig. 3.3, much larger than the corresponding values for Ge and Si ($\simeq\ 70\,meV$).

Carbon Nanotubes

The first measurements of optical gap E_g in the semiconducting single wall carbon nanotubes (SWNTs) started to be available after 10 years since their discovery. Since experiments are performed at room temperature, the understanding of $E_g(T)$ is extremely important. Capaz et al. [15] calculated the optical gap of a large variety, for diameter and chirality (n, m), of SWNTs. The meaning of the pair of indices (n, m) is more evident in Fig. 3.4.

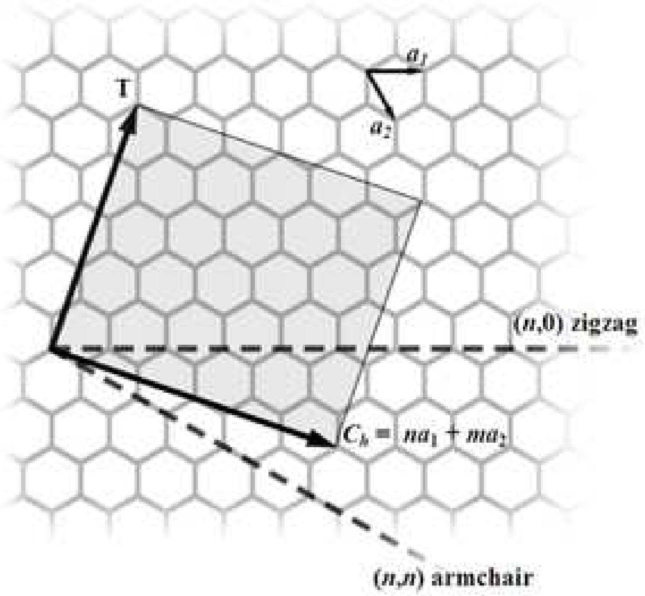

Figure 3.4: The (n, m) nanotube naming scheme can be thought of as a vector ($\mathbf{C_h}$) in an infinite graphene sheet that describes how to "roll up" the graphene sheet to make the nanotube. $\mathbf{T}$ denotes the tube axis, and $\mathbf{a_1}$ and $\mathbf{a_2}$ are the unit vectors of graphene in real space.

The shift of the electronic eigenenergies due to static atomic displacements is calculated using the HAC approach and the electron-phonon coupling has been evaluated using the "frozen phonon" approach. Even though the energy shift properly takes into account the effect of the zero point motion, the authors plotted in Fig. 3.5 the calculated values of $\Delta E_g(T) = E_g(T) - E_g(0)$, which vanishes for $T \to 0$, up to $T = 400\,K$. As a consequence it is not possible to glean any idea about the renormalization of the optical gap due to the zero point motion effect.

The general conclusion is that the temperature dependence of the band gap is small if compared to bulk semiconductors. The most interesting thing to observe in Fig. 3.5 is that in the case when $\nu = (n - m)\,mod\,3 = 2$ SWNTs the gap in general exhibits a *non–monotonic* variation with temperature, positive for small T and negative for larger T. Besides being observed in photoluminescence experiments [16], these trends find an explanation in the analysis of different contributions to $E_g(T)$

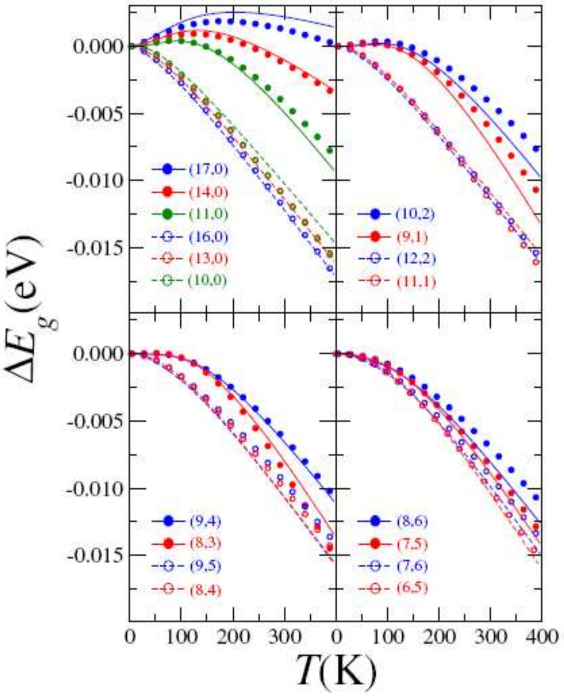

Figure 3.5: Calculated and fitted optical gap as function of temperature. Solid and dots lines represent results for $\nu = 2$ SWNTs. Open dots and dashed lines represents instead results for $\nu = 1$ SWNTs. From Ref. [15].

coming from the different phonon modes. The authors, in fact, plotted the electron-phonon spectral function for the gap, g^2F in Fig. 3.6. The plot is restricted to the low–energy phonon branches (two upper panels), because they are the most relevant in the considered temperature range $0 < T < 400\,K$.

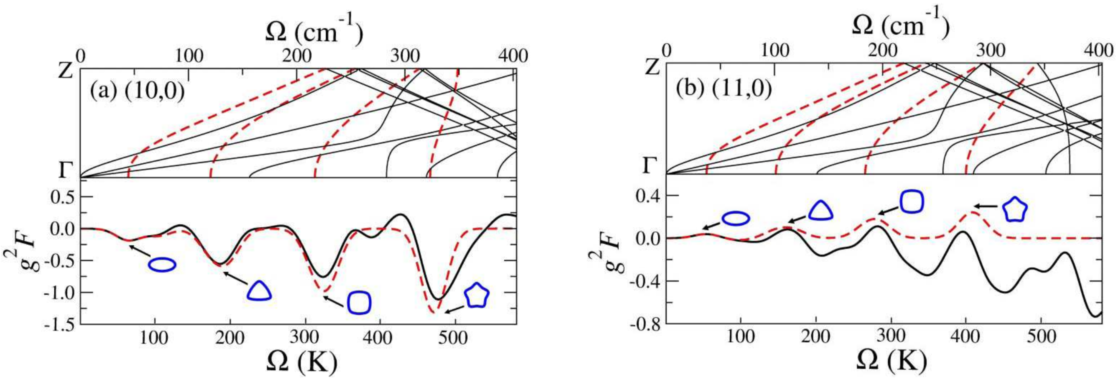

Figure 3.6: Dimensionless g^2F (lower panel) and phonon spectra (upper panels) for $\nu = 1$ SWNTs (left picture) and $\nu = 2$ SWNTs (right picture). In both lower panels, the solid black line is the total g^2F and the dashed line is the contribution from the modes which deform the shape. From Ref. [15].

In Fig. 3.6 the contribution given by the shape deformation modes (SDMs), which deform the circular section of tubes to ellipses, triangles, squares etc., is highlighted in dashed lines (two lower panels). In $\nu = 1$ SWNTs this contribution is large, negative and dominates in all temperature range. In $\nu = 2$ SWNTs instead, it is small, positive and dominates in the temperature range $T < 200K$, as beyond the other modes start being more important. However the global effect is appreciably lower with respect to $\nu = 2$ SWNTs and this explains the corresponding *non–monotonic* gap variation with temperature noticed in $\nu = 2$ SWNTs.

3.1.2 Finite temperature excitons

The HAC approach has been also extended to the description of the finite temperature properties of excitons. These neutral, bosonic–like particles are created by bound electron–hole pairs. Excitons are usually probed in photo absorption experiments. The absorption spectra of bulk materials, surfaces, nanostructures and even organic or biological molecules are usually described by the solution of the Bethe–Salpeter (BS) equation [17] of the many-body perturbation theory. It represents a well established tool [18] to interpret absorption and photoluminescence experiments, that are usually carried out at room temperature.

Absorption and emission lines at any temperature show an intrinsic width [19] that reflects the *finite* lifetime of the excitonic states. The BS equation is actually solved assuming atoms frozen in their crystallographic positions, so the effect of lattice vibrations is neglected at all. As a consequence the excitonic states acquire an *infinite* lifetime and they are completely insensitive to the temperature. The calculated absorption spectrum is then convoluted with an ad–hoc broadening function to yield the best agreement with the experiments. Even in the T going to zero limit in fact, atoms vibrate in order to satisfy the indetermination principle (zero–point vibrations).

In the frozen atom (FA) approximation the BS equation, the excitonic states $\mid \lambda_{FA}\rangle$ and the energies E_{λ}^{FA} are eigenstates and eigenvalues of the Hamiltonian $\mathbf{H}^{FA}$ written in the electron (e) hole (h) basis [17]

$$H^{FA}_{\substack{ee'\\hh'}} = (E_e - E_h)\delta_{eh,e'h'} + (f_e - f_h)\Xi_{\substack{ee'\\hh'}}. \tag{3.23}$$

$E_{e(h)}$ and $f_{e(h)}$ are the quasielectron (hole) energies and occupations. Ξ is the Bethe–Salpeter kernel, that is the sum of a direct and an exchange electron–hole (e–h) scattering. An explicit expression for $\Xi_{\substack{ee'\\hh'}}$ can be found, for example, in Ref. [18].

The absorption spectrum is given by the imaginary part of the dielectric function

$$\epsilon_2(\omega) = -\frac{8\pi}{V}\sum_{\lambda} \mid S_{\lambda}^{FA} \mid^2 \Im\left[(\omega - E_{\lambda}^{FA} + i\eta)^{-1}\right], \tag{3.24}$$

where S_λ^{FA} are the excitonic optical strengths and η is a broadening parameter.

The smallest excitation energy in semiconductors, the gap energy, is usually much larger than the typical thermal energy corresponding to the experimental temperatures. This justifies the fact that the quasiparticle (QP) energies $E_{e,h}$, obtained within the GW approximation for the electronic self-energy, are assumed to be real and independent on T. The Hamiltonian $\mathbf{H}^{FA}$ is also independent on T and Hermitian. As a consequence the excitonic states $\mid \lambda_{FA}\rangle$ will have an *infinite* lifetime and the eigenenergies E_λ^{FA} will be real. An ad–hoc broadening parameter η is introduced in Eq. (3.24) just to mimic the experimental broadening.

In Ref. [8] the BS equation is solved in a fully ab–initio manner including the coupling with lattice vibrations. In the finite temperature regime the QP energies $E_{e,h}$ acquire an explicit dependence on the temperature $E_{e,h}(T) = E_{e,h} + \Delta E_{e,h}(T)$, with $\Delta E_{e,h}(T) = \Delta E_{e,h}^{e-ph}(T) + \Delta E_{e,h}^{TE}(T)$. $\Delta E_{e,h}^{TE}(T)$ is the thermal expansion (TE) contribution while $\Delta E_{e,h}^{e-ph}(T)$ represents the complex energy correction that arises from the electron-phonon interaction. In Ref. [8] the electron-phonon interaction is treated in the HAC approach. In particular the QP states acquire a *finite* lifetime as shown in Ref. [20].

The temperature dependence of the QP states modifies Eq. (3.23). The BS Hamiltonian turns, in fact, to be now a *non–Hermitian* operator

$$H_{\substack{ee'\\hh'}}(T) = H^{FA}_{\substack{ee'\\hh'}} + \left[\Delta E_e(T) - \Delta E_h(T)\right]\delta_{eh,e'h'}. \tag{3.25}$$

The excitonic states are the solutions of the eigenvalue problem $H(T) \mid \lambda(T)\rangle = E_\lambda(T) \mid \lambda(T)\rangle$. The eigenstates $\mid \lambda(T)\rangle$ are linear combinations of e–h pairs: $\mid \lambda(T)\rangle = \sum_{e,h} A^\lambda_{e,h}(T) \mid eh\rangle$, with $A_{e,h}(T) = \langle eh \mid \lambda\rangle$. If we plug this expansion in the definition of the excitonic energies $E_\lambda(T) = \langle\lambda(T) \mid \mathbf{H} \mid \lambda(T)\rangle$, we get

$$E_\lambda(T) = \langle\lambda(T) \mid \mathbf{H^{FA}} \mid \lambda(T)\rangle + \sum_{e,h} \mid A^\lambda_{e,h}(T) \mid^2 \left[\Delta E_e(T) - \Delta E_h(T)\right]. \tag{3.26}$$

Using Eq. (3.19) and neglecting the TE term, Eq. (3.26) yields

$$\begin{aligned}\Re\left[\Delta E_\lambda(T)\right] = &\left[\langle\lambda(T) \mid \mathbf{H^{FA}} \mid \lambda(T)\rangle - \langle\lambda_{FA} \mid \mathbf{H^{FA}} \mid \lambda_{FA}\rangle\right] + \\ &+ \int d\omega \Re\left[g^2F_\lambda(\omega,T)\right]\left[\mathcal{N}_{\mathbf{q}\lambda} + \frac{1}{2}\right],\end{aligned} \tag{3.27}$$

$$\Im\left[E_\lambda(T)\right] = \int d\omega \Im\left[g^2F_\lambda(\omega,T)\right]\left[\mathcal{N}_{\mathbf{q}\lambda} + \frac{1}{2}\right], \tag{3.28}$$

where $\Delta E_\lambda(T) = E_\lambda(T) - E_\lambda^{FA}$ and an exciton–phonon coupling function $g^2F_\lambda(\omega, T) = \sum_{e,h} \mid A_{e,h}^\lambda(T) \mid^2 [g^2F_e(\omega) - g^2F_h(\omega)]$ has been introduced. Eq. (3.28) defines, in an ab–initio manner, the non radiative excitonic lifetime that is infinite in the FA approximation.

The dielectric function now depends explicitly on T,

$$\epsilon_2(\omega) = -\frac{8\pi}{V} \sum_\lambda \mid S_\lambda(T) \mid^2 \Im \left[(\omega - E_\lambda(T))^{-1} \right], \tag{3.29}$$

and no damping parameter η is needed anymore.

When $T \to 0$ the zero point motion effect causes the excitonic states to have a finite lifetime.

The experimental optical spectra of Si, shown in Fig. 3.7, are dominated by two excitonic peaks. As the temperature increases, the peaks move towards lower energies and the width, reflecting only the damping of the excitons due to the scattering with phonons, increases with temperature. These results are well reproduced by the finite temperature BS equation. The $g^2F_\lambda(\omega)$, right panel of Fig. 3.7, is used to pin down the phonon modes that contribute to the redshift of the peaks: the optical phonons at 60 meV. As the temperature increases, the phonon population increases and an analysis of the different contribution to Eq. (3.27) shows that the $g^2F_\lambda(\omega)$ integral is the dominant negative contribution. This is the *incoherent contribution*, coming when electrons and holes interact separately with the lattice vibrations and when $\mid \lambda(T)\rangle \simeq \mid \lambda_{FA}\rangle$. It happens in the case of Si because e–h pairs are weakly bounded.

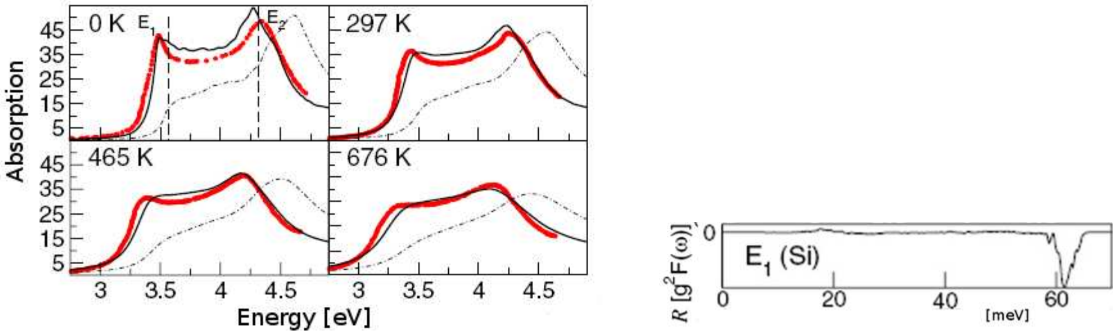

Figure 3.7: Optical absorption of bulk Silicon for several temperatures. The experimental spectra (circles) are compared with the BS equation (solid line) and with the independent particle approximation. From Ref. [8].

In Ref. [8] the author considers also a layered material, hexagonal–BN ($h-BN$). $h-BN$ is a wide gap insulator, therefore excitonic effects are expected to be enhanced by the layered structure. Moreover the phonon band structure of $h-BN$ is well known [21] and it is characterized by the competition of in–plane and out–of–plane modes.

In $h--BN$ instead the lattice vibrations participate actively in the exciton build up. In fact the coupling induces bright to dark (and vice versa) transitions. It happens when the first term of Eq. (3.27) is dominant. It represents the *coherent contribution* that modifies the A_{eh}^{λ} components and vanishes when $\mid \lambda(T)\rangle = \mid \lambda_{FA}\rangle$. The thermal evolution of the excitonic energies and optical strengths $\mid S_{\lambda}(T) \mid^2$ for the near gap excitons is shown in Fig. 3.8. The size of the circles is proportional to $\mid S(T) \mid^2$ which strongly depends on temperature. The R_1 and the B_2 excitons undergo a bright to dark (and vice versa) transition at room temperature. The microscopical mechanism is a transfer of optical strength between energetically close excitonic states.

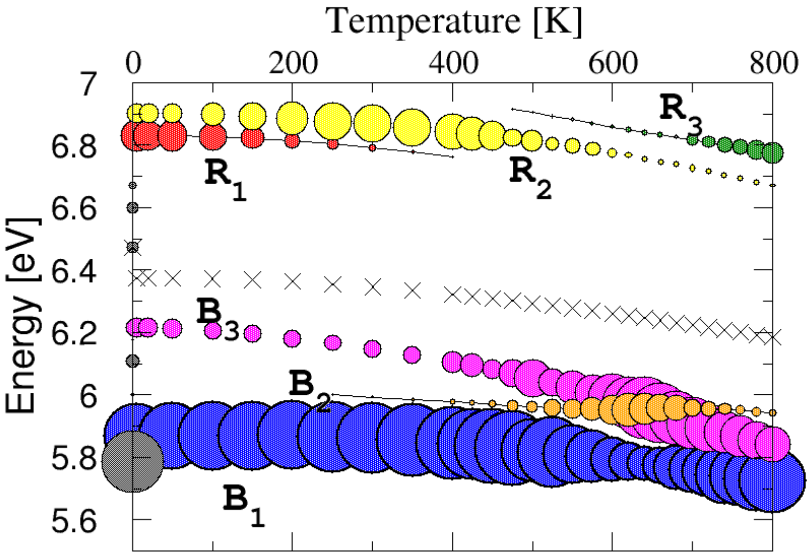

Figure 3.8: Temperature dependence of the energies and oscillator strengths of the near–gap bound (B) and resonant (R) excitons in *h*–BN. The sizes of the circles are proportional to the excitonic optical strengths. From Ref. [8].

This example concludes the retracing of the works where finite temperature properties have been investigated within the HAC approach. In Sec. 3.3.1 the electron-phonon interaction will be treated in the many-body framework.

3.2 Polymers in the Heine Allen Cardona approach

I first evaluated in *trans*-polyacetylene the $\Delta E_{n\mathbf{k}}$ given by Eq. (3.22), at $T = 0\,K$ on uniformly distributed one dimensional grids $N_{\mathbf{q}}\,1\,1$ with $N_{\mathbf{q}} = 10$, 26, 40 and 54.

The calculation proceeds as follows: first the variation of the self–consistent potential ΔV_{scf} is calculated on a given grid, then the electron-phonon coupling matrix elements $g^{\mathbf{q},\lambda}_{n'n\mathbf{k}}$ are evaluated on the same grid of $\mathbf{k}$ points but using a larger number of bands. For any grid the second calculation has been repeated with an increasing number of bands just to check the convergence. The results are summarized in Figs. 3.9 and 3.10 at the Γ and X points, that are in common among all the considered grids.

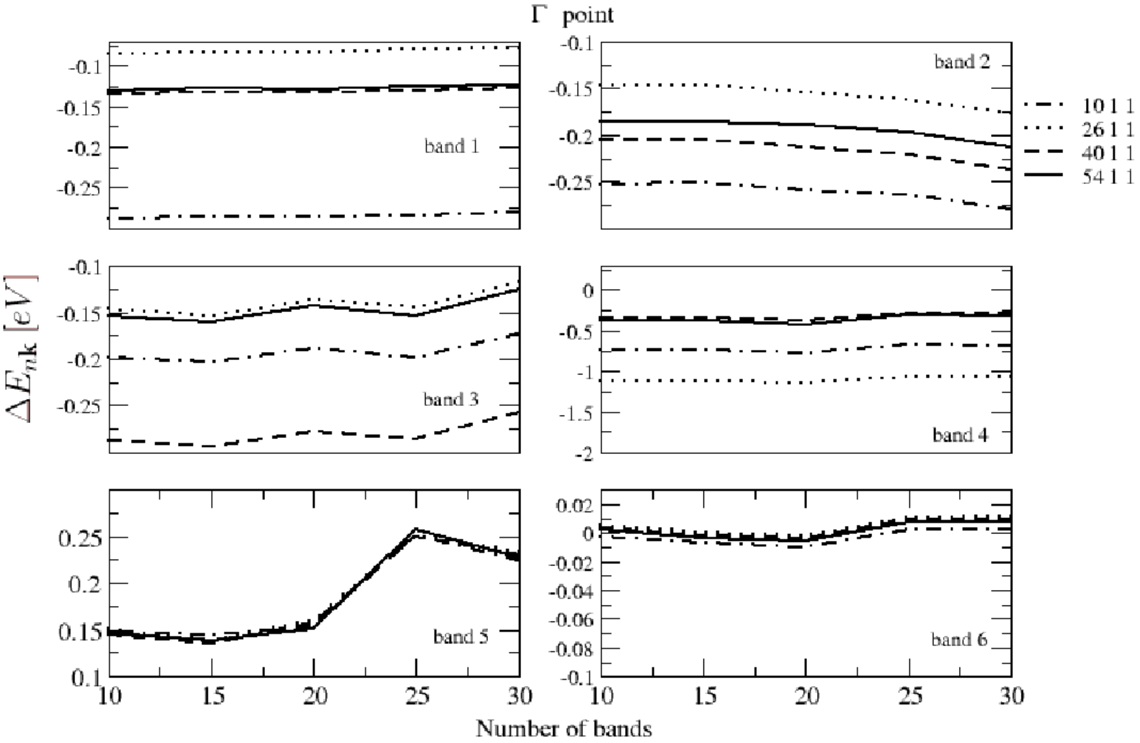

Figure 3.9: Calculated energy corrections at the Γ–point for different grids dimensions and number of bands.

The corrected gap is shown instead in Fig. 3.11, where the reference DFT electronic gap is 0.6 eV.

The first conclusion is that no particular insight regarding the appropriate number of bands to use can be extracted from an analysis of Figs. 3.9, 3.10 and 3.11. In general unexpected fluctuations at Γ, for the 5^{th} band appear. The same happens for the 4^{th}, 5^{th} and 6^{th} band at X, as shown in Fig. 3.10. Fig. 3.11 shows how the band gap varies with the numbers of bands. Even if the gap value appears to fluctuate, it can be inferred from the global trend that the renormalized electronic gap decreases with respect to the reference one, showing a sizable finite zero point motion effect.

The most puzzling and evident aspect of Figs. 3.9, 3.10 and 3.11 is the $\Delta E_{n\mathbf{k}}$ oscillations with the number of bands and $\mathbf{k}$–points. These oscillations are clearly related to an instability of the HAC theory whose source could be, however, simply

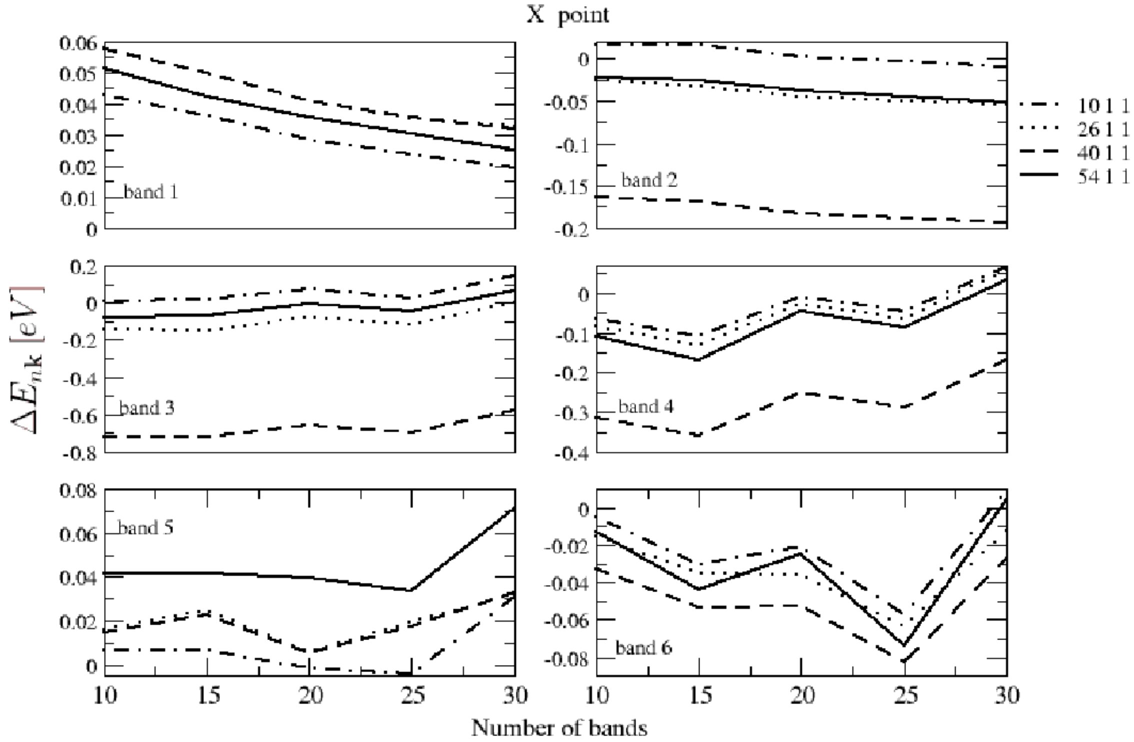

Figure 3.10: Calculated energy corrections at the X–point for different k grids and varying the number of bands.

numerical. For this reason I further investigated the nature of above shown energy oscillations performing the sum over $\mathbf{q}$ points appearing in Eq. (3.22) using a randomly distributed three dimensional grid. So I generated 500 random $\mathbf{q}$ points. For each $\mathbf{q}$ point phonons and electron-phonon matrix elements are calculated, using the electronic density of a 10 1 1 $\mathbf{k}$–point grid, and 45 empty bands.

The energy corrections and the corresponding unperturbed KS energies are shown in Fig. 3.12. The oscillations of the energy corrections are, somehow, smaller. However, the behaviour of some states is still unstable. The energy correction for the state $\mid n = 4, \mathbf{k}_3 = 0.2\,(\frac{2\pi}{a}, 0, 0)\rangle$, for example, is about $-0.5\,eV$. This value converges when 40 bands are included in the sum. For other states the convergence is much slower, as for the state $\mid n = 4, \mathbf{k}_4 = 0.3(\frac{2\pi}{a}, 0, 0)\rangle$. In this case the energy correction is $-0.46\,eV$ with 20 bands, then it fluctuates between $-0.51\,eV$, $-0.48\,eV$ and $-0.37\,eV$ when 30, 40 and 50 bands are included.

Although the numerical oscillations still appear, Fig. 3.12 clearly highlights that the HAC corrections are huge, of the same order of magnitude of the electronic gap. But are they also reliable?

The oscillations of the HAC energy corrections point to the fact that the self-energy, indeed, must have a complex dependence on the bare electrons energy.

A direct approach to investigate the presence of complex structures in the HAC

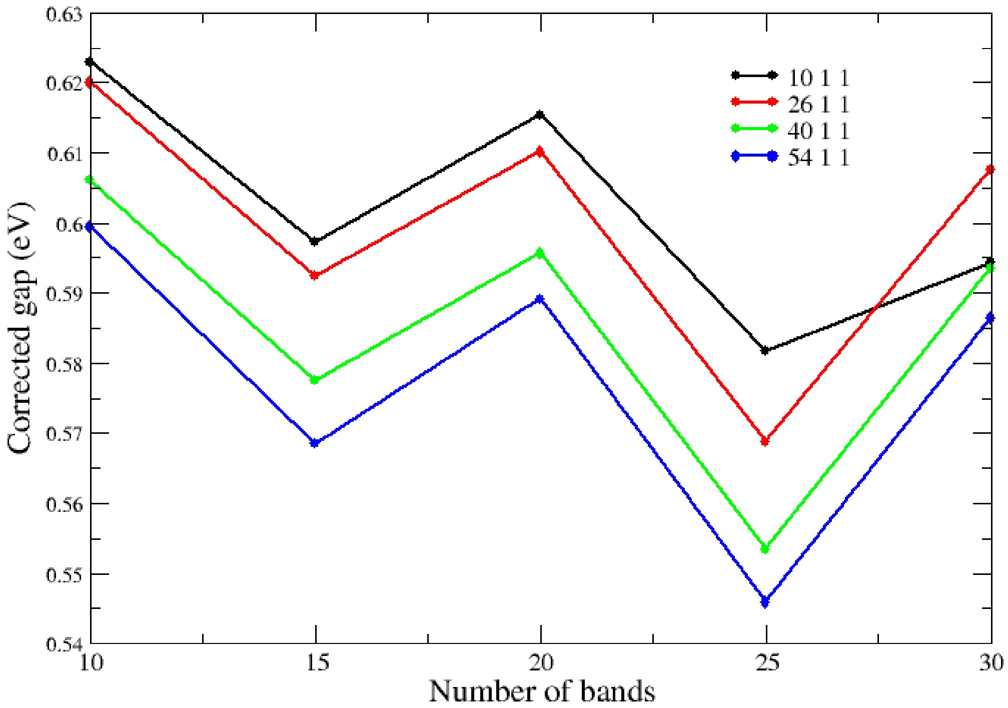

Figure 3.11: Renormalized electronic gap for different k grids and number of bands.

approach is to introduce, by hand, a frequency dependent energy correction

$$\Delta E^{Fan}_{n\mathbf{k}} \rightarrow \Delta E^{Fan}_{n\mathbf{k}}(\omega) = \sum_{n'\mathbf{q},\lambda} \frac{\left| g^{\mathbf{q},\lambda}_{n'n\mathbf{k}} \right|^2}{N_{\mathbf{q}}} \cdot \frac{2B(\omega_{\mathbf{q}\lambda}) + 1}{\omega - \epsilon_{n'\mathbf{k}+\mathbf{q}}}, \tag{3.30}$$

releasing the adiabatic approximation on which the HAC approach is based.

Eq. (3.30) can be formally obtained using the diagrammatic many-body perturbation theory, as shown in the next section. We can now take into account the frequency dependence of the HAC corrections by expanding up to the first order in the derivative of $\Delta E^{Fan}_{n\mathbf{k}}(\omega)$ around the bare energy $\epsilon_{n\mathbf{k}}$

$$\begin{aligned} E_{n\mathbf{k}} &= \epsilon_{n\mathbf{k}} + \Delta E^{Fan}_{n\mathbf{k}}(\epsilon_{n\mathbf{k}}) + \left.\frac{\partial \Delta E^{Fan}_{n\mathbf{k}}(\omega)}{\partial \omega}\right|_{\omega=\epsilon_{n\mathbf{k}}} (E_{n\mathbf{k}} - \epsilon_{n\mathbf{k}}) \\ &= \epsilon_{n\mathbf{k}} + Z_{n\mathbf{k}} \Delta E^{Fan}_{n\mathbf{k}}(\epsilon_{n\mathbf{k}}), \end{aligned} \tag{3.31}$$

where the *renormalization factor*, $Z_{n\mathbf{k}}$ reads

$$Z_{n\mathbf{k}} = \left[1 - \left.\frac{\partial \Delta E^{Fan}_{n\mathbf{k}}(\omega)}{\partial \omega}\right|_{\omega=\epsilon_{n\mathbf{k}}} \right]^{-1}. \tag{3.32}$$

The "renormalized" particle with energy $E_{n\mathbf{k}}$, is otherwise named quasiparticle. Physically, a quasiparticle state is viewed as the original non interacting state, but surrounded by an "interaction cloud" [22], which is responsible for the renormalization. The $Z_{n\mathbf{k}}$ factor describes the weight of the bare electron ($Z_{n\mathbf{k}} = 1$) in the quasiparticle.

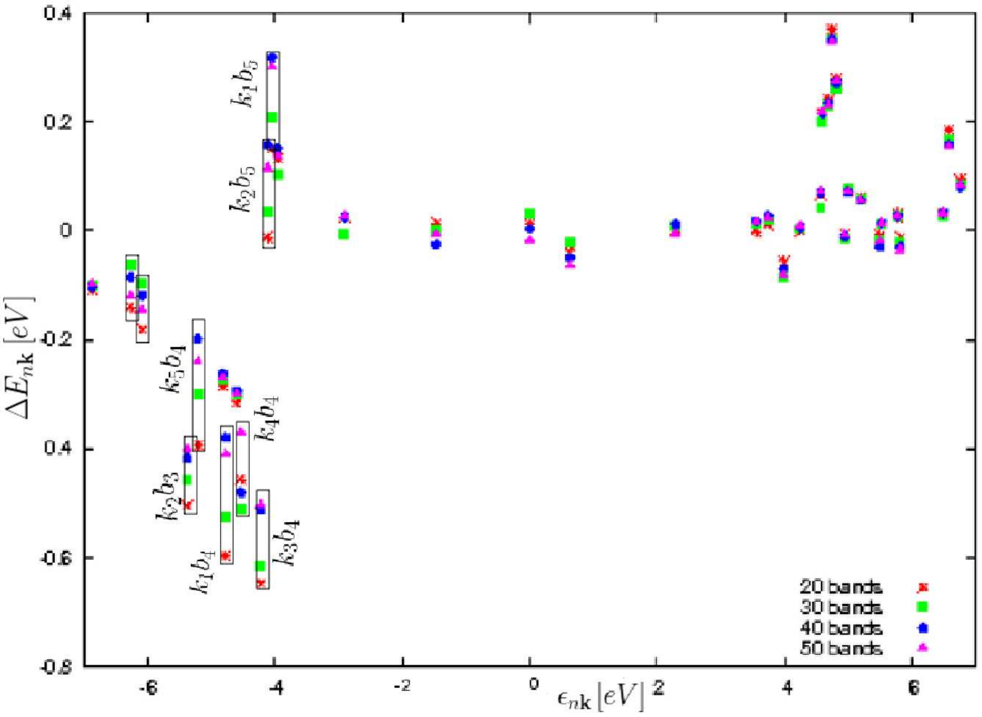

Figure 3.12: Calculated energy corrections as a function of the KS energy, using a random grid of $\mathbf{q}$–points and different numbers of empty bands. The generic state is labeled with $\mathbf{k}_i b_j$ where i is the i^{th} $\mathbf{k}$-vector $\mathbf{k}_i = \frac{(i-1)}{10}(\frac{2\pi}{a}, 0, 0)$ on a uniform grid 10×1×1 and j is the j^{th} occupied band.

The basic condition of validity of Eq. (3.30), is that the higher order derivatives must be small. In a many-body language it means that the bare energy must be far from any intense pole of the self-energy, i.e. it should be in an energy region where $\Re\Sigma^{Fan}_{n\mathbf{k}}(\omega)$ is almost flat. In these conditions the first derivative of $\Re\Sigma^{Fan}_{n\mathbf{k}}(\omega)$ is generally small and the renormalization factor is positive and less than 1. These boundary values are consistent with the physical meaning of *electron charge*, associated to the $Z_{n\mathbf{k}}$ factors within many-body perturbation theory. I will discuss more extensively these factors in the next chapter.

The $Z_{n\mathbf{k}}$ factors calculated according to Eq. (3.32) indeed reveal pronounced numerical instabilities, as shown in Tab. 3.1. Beside being negative in some cases (4^{th} band and 10^{th} $\mathbf{k}$–point), the $Z_{n\mathbf{k}}$ factors are often greater than one (6^{th} band). This is clearly unphysical. The numerical instabilities of the HAC energy corrections, are therefore connected to the instability of the polaronic charges, $Z_{n\mathbf{k}}$, when a quasiparticle picture is adapted.

The interpretation of the puzzling values of the $Z_{n\mathbf{k}}$ factors requires a deeper analysis of the real energy dependence of the Fan self-energy. In order to do that in the following section I will review the many-body approach to the electron-phonon interaction .

Renormalization factors $Z_{n\mathbf{k}}$									
Bands	$\mathbf{k}_1$	$\mathbf{k}_2$	$\mathbf{k}_3$	$\mathbf{k}_4$	$\mathbf{k}_5$	$\mathbf{k}_6$	...	$\mathbf{k}_{10}$	
4	1.60	1.45	0.64	1.38	2.07	1.81	...	−.86	
5	0.28	0.26	0.25	0.25	0.24	0.21	...	0.16	
6	5.51	4.58	3.89	3.87	3.29	1.74	...	0.97	

Table 3.1: Renormalization factors for different bands and $\mathbf{k}$–points calculated on a uniform grid 60×1×1 and summing over a randomly distributed one dimensional grid of $\mathbf{q}$ points. The generic $\mathbf{k}$-vector is labeled with $\mathbf{k}_i = \frac{(i-1)}{60}(\frac{2\pi}{a}, 0, 0)$ on a uniform grid 60×1×1.

3.3 Beyond the HAC approach

The HAC approach represents a successful and predictive tool to study polaronic effects in an ab–initio manner, as exemplified in the sections 3.1.1 and 3.1.2. Nevertheless the HAC approach suffers of drastic limitations, mainly connected to the adiabatic approximation, as I highlighted in the previous section. To disclose, and cure, these limitations in the next section I will re–derive the HAC equations within the more general MBPT. This non–adiabatic extension of the HAC approach will be applied to polymers in the next chapter.

3.3.1 The many-body perspective: a non adiabatic approach

Within the many-body framework the electron-phonon interaction is obtained from a perturbative calculation [12] of the electron self-energy at the second order in atomic displacement $\mathbf{u}_{Is}$. The effect of the electron-phonon interaction is then broken up into two contributions: the Fan [1] and the Debye-Waller term [4]. The corresponding Feynman diagrams are shown in Fig. 3.13.

The Fan's diagram can be compared to the self-energy diagram evaluated in Sec. 1.4.2, where the screened interaction W is replaced by a phonon propagator of wavevector $\mathbf{q}$ and branch λ. In the GW approximation only one phonon is assumed to be virtually scattered. Applying the diagrammatic rules it is possible to define the self-energy operator, recovering the expression originally evaluated by Fan [3].

The Fan's contribution is obtained by a convolution of the electron and the phonon Green's function

$$\Sigma^{Fan}_{n\mathbf{k}}(\omega_i) = -\frac{1}{\beta}\frac{1}{N_{\mathbf{q}}}\sum_{\mathbf{q}\lambda}\sum_{n'} \mid g^{\mathbf{q}\lambda}_{n'n\mathbf{k}} \mid^2 \sum_{j=-\infty}^{+\infty} \mathcal{D}^{(0)}(\mathbf{q}\lambda, \omega_j)\mathcal{G}^{(0)}(\mathbf{k}-\mathbf{q}, \omega_i - \omega_j). \quad (3.33)$$

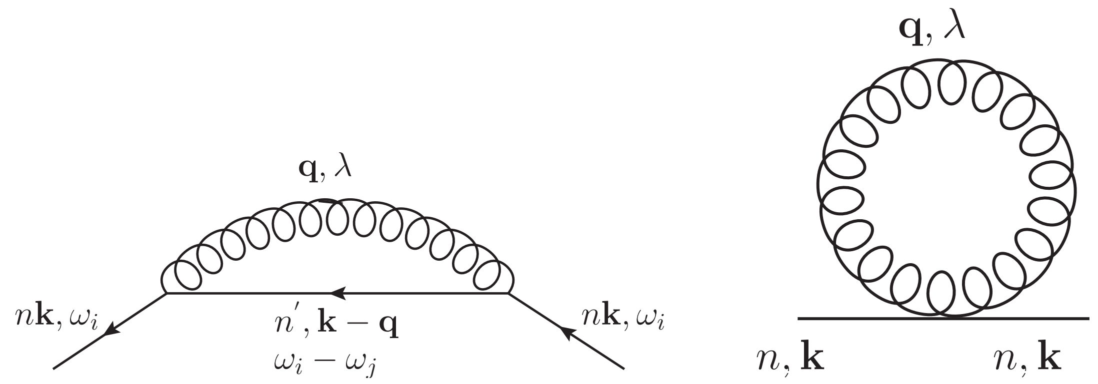

Figure 3.13: Electronic self-energy diagrams which are widely used to get the temperature renormalization of the bands to second order in the displacement $\mathbf{u}_{Is}$. Fan (on the left) and the Debye-Waller (on the right) terms.

Sums over Matsubara frequencies usually appear when Matsubara Green's functions are used. For the electronic propagator we will use the definition of Green's function provided by Eq. (1.81). The phonon propagator instead is [23]

$$\mathcal{D}^{(0)}(\mathbf{q}\lambda, \omega_j) = \left(\frac{1}{i\omega_j - \omega_{\mathbf{q}\lambda}} - \frac{1}{i\omega_j + \omega_{\mathbf{q}\lambda}} \right). \tag{3.34}$$

It is important to note that the definition (3.34) implies a time–dependent displacement operator.

Inserting Eqs. (1.81) and (3.34) in Eq. (3.33) we can evaluate the polaronic electron self-energy due to the scattering with phonons:

$$\begin{aligned} \Sigma^{Fan}_{n\mathbf{k}}(\omega_i) = -\frac{1}{\beta} \sum_{n'\,\mathbf{q}\,\lambda} \frac{\mid g^{\mathbf{q}\lambda}_{n'n\mathbf{k}} \mid^2}{N_{\mathbf{q}}} \sum_{j=-\infty}^{+\infty} \left(\frac{1}{i\omega_j - \omega_{\mathbf{q}\lambda}} - \frac{1}{i\omega_j + \omega_{\mathbf{q}\lambda}} \right) \cdot \\ \cdot \frac{1}{i\omega_i - i\omega_j - \epsilon_{n'\mathbf{k}-\mathbf{q}} + \mu}. \end{aligned} \tag{3.35}$$

We note that there is frequency conservation: an electron with frequency $i\omega_i$ absorbs or emits a phonon of frequency $i\omega_j$, so that the electron is scattered to an intermediate state with frequency $i\omega_i - i\omega_j$. The summations are performed over all intermediate electronic bands, momenta $\mathbf{q}$, branches λ and frequencies. We will follow the same strategy outlined in Sec. 1.4.2 and we define a function analogous to Eq. (1.111)

$$F(\omega) = \frac{1}{i\omega_i - \omega - \epsilon_{n'\mathbf{k}-\mathbf{q}} + \mu} \cdot \left[\frac{1}{\omega + \omega_{\mathbf{q}\lambda}} - \frac{1}{\omega - \omega_{\mathbf{q}\lambda}} \right], \tag{3.36}$$

having poles at the frequencies $\pm\omega_{\mathbf{q}\lambda}$ and $i\omega_i - \epsilon_{n'\mathbf{k}-\mathbf{q}} + \mu$.

The summation over the Matsubara frequencies is performed by converting it into an integral over a contour $\mathcal{C}'$ enclosing all poles of the function $F(\omega)B(\omega)$, where $B(\omega)$ is the Bose function distribution, whose poles occur at frequencies $\omega_j = \frac{2j\pi}{\beta}$, $j = 0, \pm 1, \ldots.$ The suitable integration region $\mathcal{C}'$ is shown in Fig. 3.14.

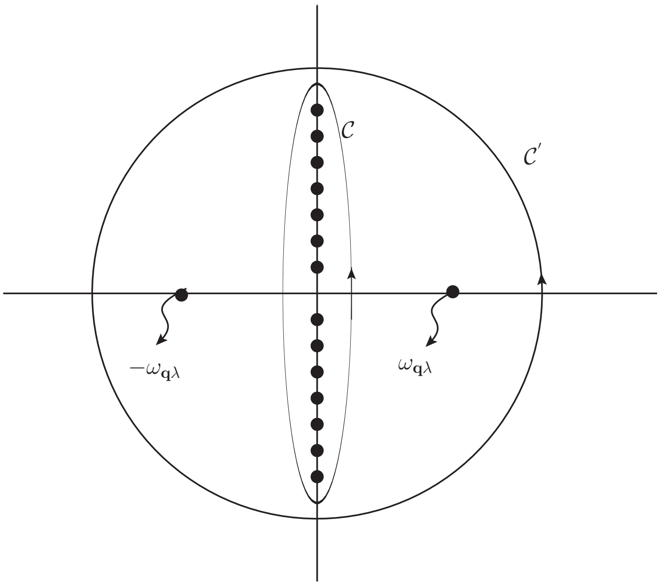

Figure 3.14: The contour $\mathcal{C}'$ on the complex plane used to integrate the polaronic self-energy.

The contour integral can be evaluated by applying the residuals theorem

$$\begin{aligned}
\underbrace{\oint_{\mathcal{C}'} d\omega F(\omega) B(\omega)}_{I} &= 2\pi i \Big[\mathrm{Res} \left[F(\omega)B(\omega)\right]\big|_{\omega=\pm\omega_{\mathbf{q}\lambda}} + \\
&+ \mathrm{Res} \left[F(\omega)B(\omega)\right]\big|_{\omega=i\omega_i-\epsilon_{n'\mathbf{k}-\mathbf{q}}+\mu} \Big] + \\
&+ \underbrace{\oint_{\mathcal{C}} d\omega F(\omega) B(\omega)}_{J}. \qquad (3.37)
\end{aligned}$$

It implies to consider all residuals of $F(\omega)B(\omega)$, both at poles of $F(\omega)$ and those of $B(\omega)$ which fall within the contour $\mathcal{C}$. The latest sum up to the integral J

$$J = \oint_{\mathcal{C}} d\omega F(\omega) B(\omega) = \frac{2\pi i}{\beta} \sum_{j=-\infty}^{+\infty} F(i\omega_j). \qquad (3.38)$$

Since the integral I on contour $\mathcal{C}' : Re^{i\theta}$ vanishes when $R \to \infty$, the summation over the Matsubara frequencies which identifies the integral J is re–written in terms of a sum of residues

$$-\frac{1}{\beta} \sum_{j=-\infty}^{+\infty} F(i\omega_j) = \mathrm{Res} \left[F(\omega)B(\omega)\right]\big|_{\omega=\pm\omega_{\mathbf{q}\lambda}} + \mathrm{Res} \left[F(\omega)B(\omega)\right]\big|_{\omega=i\omega_i-\epsilon_{n'\mathbf{k}-\mathbf{q}}+\mu}. \qquad (3.39)$$

The residues evaluated at each pole are shown as follows

$$\begin{aligned}
\omega &= \omega_{\mathbf{q}\lambda} & \mathrm{Res}_1 &= -\frac{B(\omega_{\mathbf{q}\lambda})}{i\omega_i - \omega_{\mathbf{q}\lambda} - \epsilon_{n'\mathbf{k}-\mathbf{q}} + \mu}, & (3.40)\\
\omega &= -\omega_{\mathbf{q}\lambda} & \mathrm{Res}_2 &= \frac{B(-\omega_{\mathbf{q}\lambda})}{i\omega_i + \omega_{\mathbf{q}\lambda} - \epsilon_{n'\mathbf{k}-\mathbf{q}} + \mu}, & (3.41)\\
\omega &= i\omega_i - \epsilon_{n'\mathbf{k}-\mathbf{q}} + \mu & \mathrm{Res}_3 &= \frac{2\omega_{\mathbf{q}\lambda} B(i\omega_i - \epsilon_{n'\mathbf{k}-\mathbf{q}} + \mu)}{\left[(i\omega_i - \epsilon_{n'\mathbf{k}-\mathbf{q}} + \mu)^2 - \omega^2_{\mathbf{q}\lambda}\right]}. & (3.42)
\end{aligned}$$

Finally, we use the Bose function properties and the frequencies ω_i as odd multiples of $\frac{\pi}{\beta}$ to observe that $B(-\omega_{\mathbf{q}\lambda}) = -1 - B(\omega_{\mathbf{q}\lambda})$ and $B(i\omega_i - \epsilon_{n'\mathbf{k}-\mathbf{q}} + \mu) = -1 + f_{n'\mathbf{k}-\mathbf{q}}$. These expressions can be readily exploited to rewrite Eq. (3.39) in a more compact form

$$\frac{1}{\beta}\sum_{j=-\infty}^{+\infty} F(i\omega_j) = \frac{B(\omega_{\mathbf{q}\lambda}) + 1 - f_{n'\mathbf{k}-\mathbf{q}}}{i\omega_i - \omega_{\mathbf{q}\lambda} - \epsilon_{n'\mathbf{k}-\mathbf{q}} + \mu} + \frac{B(\omega_{\mathbf{q}\lambda}) + f_{n'\mathbf{k}-\mathbf{q}}}{i\omega_i + \omega_{\mathbf{q}\lambda} - \epsilon_{n'\mathbf{k}-\mathbf{q}} + \mu}. \tag{3.43}$$

A summation over a suitable integration region leads to the final expression for the electron-phonon Fan self-energy

$$\Sigma^{Fan}_{n\mathbf{k}}(\omega_i) = \sum_{n'\mathbf{q}\lambda} \frac{\mid g^{\mathbf{q}\lambda}_{n'n\mathbf{k}} \mid^2}{N_{\mathbf{q}}} \left[\frac{B(\omega_{\mathbf{q}\lambda}) + 1 - f_{n'\mathbf{k}-\mathbf{q}}}{i\omega_i - \epsilon_{n'\mathbf{k}-\mathbf{q}} - \omega_{\mathbf{q}\lambda}} + \frac{B(\omega_{\mathbf{q}\lambda}) + f_{n'\mathbf{k}-\mathbf{q}}}{i\omega_i - \epsilon_{n'\mathbf{k}-\mathbf{q}} + \omega_{\mathbf{q}\lambda}}\right]. \tag{3.44}$$

The self-energy defined by Eq. (3.44) is formally defined on the imaginary axis, due to the use of the Matsubara technique. In order to link the Matsubara Green's functions to physical observables we need to rotate the energy variable from the imaginary axis to the real axis, using an analytic continuation [24].

Eq. (3.44) on the real axis reads

$$\Sigma^{Fan}_{n\mathbf{k}}(\omega) = \sum_{n'\mathbf{q}\lambda} \frac{\mid g^{\mathbf{q}\lambda}_{n'n\mathbf{k}} \mid^2}{N_{\mathbf{q}}} \left[\frac{B(\omega_{\mathbf{q}\lambda}) + 1 - f_{n'\mathbf{k}-\mathbf{q}}}{\omega - \epsilon_{n'\mathbf{k}-\mathbf{q}} - \omega_{\mathbf{q}\lambda} - i0^+} + \frac{B(\omega_{\mathbf{q}\lambda}) + f_{n'\mathbf{k}-\mathbf{q}}}{\omega - \epsilon_{n'\mathbf{k}-\mathbf{q}} + \omega_{\mathbf{q}\lambda} - i0^+}\right]. \tag{3.45}$$

As the self-energy defined in Eq. (3.45) is a complex function, we can separate the real from the imaginary part. The $\Re\Sigma^{Fan}_{n\mathbf{k}}(\omega)$ modifies the electron energy through virtual scatterings (energy is *not* conserved) with a quantum of the lattice vibrations. The $\Im\Sigma^{Fan}_{n\mathbf{k}}(\omega)$ instead, affects the particle lifetime, through real scatterings (energy is conserved) with a quantum of the lattice vibrations.

For what concern $\Sigma^{DW}_{n\mathbf{k}}$, a frequency independent operator, it has the following expression

$$\Sigma^{DW}_{n\mathbf{k}} = -\sum_{\mathbf{q}\lambda} \frac{1}{N_{\mathbf{q}}} \sum_{n'} \frac{1}{2} \frac{\Lambda^{\mathbf{q}\lambda}_{nn'\mathbf{k}}}{\epsilon_{n\mathbf{k}} - \epsilon_{n'\mathbf{k}}} \left(2B(\omega_{\mathbf{q}\lambda}) + 1\right), \tag{3.46}$$

which corresponds to the Debye-Waller contribution to the thermal shift I have already shown in Sec. 3.1. Such expression was achieved by imposing a condition of translational invariance when every atom in the crystal is displaced of the same amount from its equilibrium position (Eq. (3.10)).

The correction to the unperturbed energy $\epsilon_{n\mathbf{k}}$ of the initial state, is given by a purely real $\Sigma^{DW}_{n\mathbf{k}}$ contribution, Eq. (3.46) and by the complex $\Sigma^{Fan}_{n\mathbf{k}}$, Eq. (3.45). So in the end every state $n\mathbf{k}$ is endowed of a complex energy. When the bare energy $\epsilon_{n\mathbf{k}}$ is far from a pole of the self-energy, then the renormalized energy is obtained by Taylor expanding $\Re\Sigma^{Fan}_{n\mathbf{k}}$ around the bare energy

$$E_{n\mathbf{k}} = \epsilon_{n\mathbf{k}} + \Re\Sigma^{Fan}_{n\mathbf{k}}(\epsilon_{n\mathbf{k}}) + \left.\frac{\partial\Re\Sigma^{Fan}_{n\mathbf{k}}(\omega)}{\partial\omega}\right|_{\omega=\epsilon_{n\mathbf{k}}} (E_{n\mathbf{k}} - \epsilon_{n\mathbf{k}}), \tag{3.47}$$

analogously to Eq. (3.30), but here derived in a more formal and clear manner. As a consequence the contribution to the $\Im\Sigma^{Fan}_{n\mathbf{k}}(\epsilon_{n\mathbf{k}})$, coming from the real transitions, is small. In these conditions a positive charge

$$Z_{n\mathbf{k}} = \left[1 - \left.\frac{\partial\Re\Sigma^{Fan}_{n\mathbf{k}}(\omega)}{\partial\omega}\right|_{\omega=\epsilon_{n\mathbf{k}}}\right]^{-1} \tag{3.48}$$

is associated to the electron. This charge is correctly smaller or equal to 1. These are the basic ingredients to make the quasiparticle concept, identified by the case (**b**) in Fig. 3.15, having supposed the existence of only one pole in the self-energy.

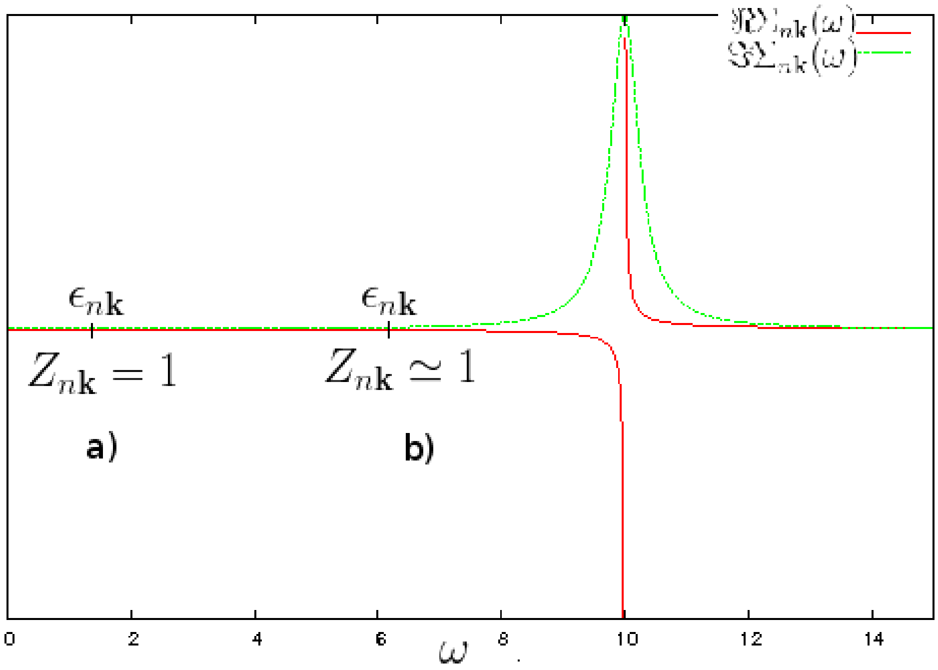

Figure 3.15: Real and Imaginary part of the self-energy. The energy range of the bare energy determines the validity, or not, of Eq. (3.47).

In this framework the origin of puzzling anomalous oscillations of $Z_{n\mathbf{k}}$ factors, pointed out in the previous section, are clearly explained. If the bare energy is close to an intense pole of the self-energy, where derivatives can be huge, then Eq. (3.47) is not valid. The $\Im\Sigma^{Fan}_{n\mathbf{k}}(\omega)$ is not small and if it so, the electron remains in its state for a short time. The electron, in fact, has a finite probability to scatter with electrons and phonons in real transitions, having an energy comparable with the pole of the self-energy. The electron will loose its identity, implying also unphysical $Z_{n\mathbf{k}}$ factors.

Nevertheless, unpredictable oscillations by varying the number of bands were observed in the previous section. I was induced to think that not only one but more than one pole, accumulated around the bare energy $\epsilon_{n\mathbf{k}}$, can explain the origin of such oscillations. Some of these poles, in fact, induce larger structures in the imaginary part of the self-energy that is influenced even by small variations of the number of bands.

The limit case (**a**) of Fig. 3.15, instead, $Z_{n\mathbf{k}} = 1$, corresponds to have a pole of the self-energy far from the bare energy $\epsilon_{n\mathbf{k}}$, so that the first derivative of $\Re\Sigma^{Fan}_{n\mathbf{k}}(\omega)$ vanishes and $\Im\Sigma^{Fan}_{n\mathbf{k}}(\epsilon_{n\mathbf{k}}) \equiv 0$. The electron only scatters in virtual transitions with the mean field created by the other particles, which renormalizes its energy. In these conditions the energy corrections Eq. (3.47) are calculated up to the 0^{th}–order in the expansion, i.e. in the *on mass shell* limit.

Moreover the diagrammatic many-body approach correctly accounts for the time dependence of the phonon amplitude. This is pointed out by the phonon frequencies $\omega_{\mathbf{q}\lambda}$, at the denominators of Eq. (3.45). However, in semiconductors and sometimes in metals (except at low temperatures and at the Fermi level) the phonon frequency can be neglected in the denominators with respect to the typical electronic energies. So in the adiabatic limit, $\omega_{\mathbf{q}\lambda} \ll\mid \epsilon_{n\mathbf{k}} - \epsilon_{n'\mathbf{k}-\mathbf{q}} \mid$ and in the *on mass shell* limit, the HAC results are recovered.

In this chapter I brought into questions the limitations of the HAC approach, when it is applied to the calculation of energy corrections. I highlighted that the numerical instabilities are an evidence for a complex structure of the self-energy. In particular, the presence of poles close to the bare energy, induces puzzling values of $Z_{n\mathbf{k}}$ factors. In the next chapter I will discuss more extensively the physical meaning of the $Z_{n\mathbf{k}}$ factors, within an extended quasiparticle approach.

Bibliography

[1] H.Y. Fan, Phys. Rev. **82**, 900 (1951)

[2] M. Becker and H.Y. Fan, Phys. Rev. **76**, 1531 (1949)

[3] H.Y. Fan, Phys. Rev. **78**, 808 (1950)

[4] E. Antoncik, Czech. J. Phys. **5**, 449 (1955)

[5] C. Keffer, T.M. Hayes and A. Bienenstock, Phys. Rev. Lett. **21**, 1676 (1968)

[6] P.B. Allen and M. Cardona, Phys. Rev. B **27**, 4760 (1983)

[7] P.B. Allen and M. Cardona, Phys. Rev. B **23**, 1495 (1981)

[8] A. Marini, Phys. Rev. Lett. **101**, 106405 (2008)

[9] P. Boulanger, PhD thesis, Université de Montréal, Canada and Université Catholique de Louvain–la–Neuve, Belgium

[10] R.M. Pick, M.H. Cohen and R.M. Martin, Phys. Rev. B **1**, 910 (1970)

[11] R. Zeyher, *Light Scattering in Solids*, Flammarion, Paris (1976)

[12] P.B. Allen and V. Heine, J. Phys. C **9**, 2305 (1976)

[13] P.B. Allen, Phys. Rev. B **18**, 5217 (1978)

[14] Y.P. Varshni, Physica (Utrecht) **34**, 149 (1967)

[15] R.B. Capaz, C.D. Spataru, P. Tangney, M.L. Cohen and S.G. Louie Phys. Rev. Lett. **94**, 036801 (2005)

[16] J. Lefebvre, Phys. Rev. B **70**, 045419 (2004)

[17] G. Strinati, Rivista del nuovo cimento **11**, 1 (1988)

[18] For a review, see G. Onida, L. Reining, and A. Rubio, Rev. Mod. Phys. **74**, 601 (2002)

[19] For a review, see M. Cardona, Solid State Commun. **133**, 3 (2005)

[20] P. Lautensclager, P.B. Allen and M. Cardona Phys. Rev. B **31**, 2163 (1985); **33**, 5501 (1986)

[21] J. Serrano, A. Bosak, R. Arenal, M. Krisch, K. Watanabe, T. Taniguchi, H. Kanda, A. Rubio, and L. Wirtz, Phys. Rev. Lett. **98**, 095503 (2007)

[22] R. D. Mattuck, *A guide to Feynman diagrams in the Many–Body problem*, McGraw–Hill, New York (1976)

[23] G.D. Mahan Many–Particle Physics (New York: Plenum) 1998

[24] L. Fetter and J.D. Walecka Chap.9, *Quantum theory of Many–Body Systems*

Chapter 4

Giant Polaronic Effects

In the previous chapter I showed that a straightforward application of the quasiparticle (QP) picture in, and even beyond, the HAC approach leads to numerical instabilities and unphysical $Z_{n\mathbf{k}}$ factors. I also discussed how these oscillations are connected to the existence of intense poles of the self-energy close to the bare electron energies. As the $Z_{n\mathbf{k}}$ factors are also linked to the quasiparticle charge, I wonder if such instabilities may even rule out the reliability of the QP concept!

For this reason in Sec. 4.1 I will review the concept of quasiparticle and of the relative spectral function. In Sec. 4.2 I will show that in the case of polymers the concept of quasiparticle fails, even at $T = 0\,K$, because of the existence of a multiplicity of structures in the spectral function. Reformulating the problem in an Hamiltonian representation I will show in Sec 4.3 that it is possible to identify each structure with a particular polaronic state, a packet of electrons and phonons. Finally in Sec. 4.4 I will give physical interpretations of the breakdown of the quasiparticle picture in terms of the Kohn-Sham (KS) charge distribution and of the isotopic effects.

4.1 Quasiparticles and Spectral Functions

The many-body Green's function theory [1] represents the most appropriate framework to describe and define the quasiparticles. In this theoretical framework, an ideal quasiparticle is the original non-interacting particle dressed by the interaction cloud [2]. The bare energy is renormalized because of the virtual scatterings described by the real part of the self-energy. A key quantity in the QP picture is the QP charge, $Z_{n\mathbf{k}}$. This charge is 1 for a non interacting electron and ≤ 1 in the QP. The $Z_{n\mathbf{k}}$ factors, indeed, measure the quality of the QP approximation. For example, in strongly correlated materials the $Z_{n\mathbf{k}}$ factors are particularly small.

The imaginary part of the self-energy is connected, instead, to the quasiparticle lifetime. A longer lifetime indicates a more stable QP, that slowly decays because of the scatterings with the other particles. Indeed a long lifetime is another condition for the existence of the QP concept.

Both quasiparticle energy, $E_{n\mathbf{k}}$ and lifetime $1/\Gamma_{n\mathbf{k}}$, are measurable with photoemission experiments. The most natural quantity to compare experiment and theory is the spectral function. A quasiparticle in fact appears as an excitation with a perfect Lorentzian-shaped spectral function $A_{n\mathbf{k}}(\omega) = \Gamma_{n\mathbf{k}}/\left[(\omega - E_{n\mathbf{k}})^2 + \Gamma_{n\mathbf{k}}^2\right]$. The position of the peak, $E_{n\mathbf{k}}$, provides the quasiparticle energy while the width $\Gamma_{n\mathbf{k}}$ is the inverse of the lifetime.

In the standard many-body perturbation theory instead the spectral function (SF) is defined in terms of the imaginary part of the Green's function of state n**k** as follows

$$A_{n\mathbf{k}}(\omega) = -\frac{1}{\pi}\Im\mathcal{G}_{n\mathbf{k}}(\omega). \tag{4.1}$$

The interacting propagator $\mathcal{G}(\mathbf{k},\omega)$ is given in terms of the Fan self-energy by

$$\mathcal{G}_{n\mathbf{k}}(\omega) = \frac{1}{\omega - \epsilon_{n\mathbf{k}} - \Re\Sigma_{n\mathbf{k}}^{Fan}(\omega) - i\Im\Sigma_{n\mathbf{k}}^{Fan}(\omega)}. \tag{4.2}$$

The excited energies of the system can be obtained by solving the equation for the poles of Eq. (4.2)

$$\omega - \epsilon_{n\mathbf{k}} - \Re\Sigma_{n\mathbf{k}}^{Fan}(\omega) - i\Im\Sigma_{n\mathbf{k}}^{Fan}(\omega) = 0. \tag{4.3}$$

When the SF exhibits a peak and a branch cut in the region $\omega_1 < \omega < \omega_2$, as shown in Fig. 4.1, then the energy $E_{n\mathbf{k}}$ of the pole can be found by applying the Newton solver (see Eq. (3.47)) to Eq. (4.3).

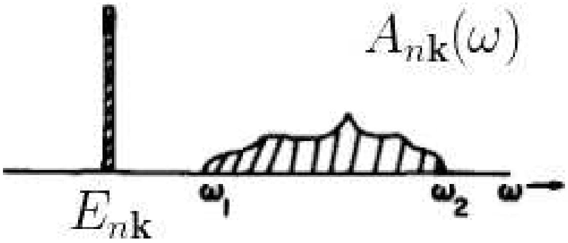

Figure 4.1: In the QP picture the spectral function $A_{n\mathbf{k}}(\omega)$ has a sharp peak at $E_{n\mathbf{k}}$ far from the region where $\Im\Sigma \neq 0$, represented by the crosshatched distribution.

Finally Eq. (4.2) can be re-written as

$$\mathcal{G}_{n\mathbf{k}}(\omega) = \frac{Z_{n\mathbf{k}}\Im\Sigma_{n\mathbf{k}}(\epsilon_{n\mathbf{k}})}{\omega - \underbrace{(\epsilon_{n\mathbf{k}} + Z_{n\mathbf{k}}\Re\Sigma_{n\mathbf{k}}(\epsilon_{n\mathbf{k}}))}_{E_{n\mathbf{k}}} - iZ_{n\mathbf{k}}\Im\Sigma_{n\mathbf{k}}(\epsilon_{n\mathbf{k}})}, \tag{4.4}$$

leading to an expression for the SF around the main peak $E_{n\mathbf{k}}$ given by

$$A^{qp}_{n\mathbf{k}}(\omega) = \frac{Z_{n\mathbf{k}}\Im\Sigma_{n\mathbf{k}}(\epsilon_{n\mathbf{k}})}{[\omega - E_{n\mathbf{k}}]^2 + [Z_{n\mathbf{k}}\Im\Sigma_{n\mathbf{k}}(\epsilon_{n\mathbf{k}})]^2}. \tag{4.5}$$

Eq. (4.5) defines the QP spectral function. When $A^{qp}_{n\mathbf{k}}(\omega)$ collects most of the weight $Z_{n\mathbf{k}} \simeq 1$ and the QP approximation is well motivated. In this case, it is also possible to associate a single, well defined energy to the particle. This is the basis of the band theory, which allows to draw the band structure of the material.

It is interesting to observe that when $Z_{n\mathbf{k}} = 1$ and $\Im\Sigma^{Fan}_{n\mathbf{k}}(\epsilon_{n\mathbf{k}}) \to 0$ the SF reduces to a delta function where the single particle states never decay, as shown in Fig. 4.2. This is the SF, $A^{(0)}_{n\mathbf{k}}$, of a bare particle with energy $\epsilon_{n\mathbf{k}}$. Also the HAC approach and the *on mass shell* limit approximation leads to delta-like spectral functions.

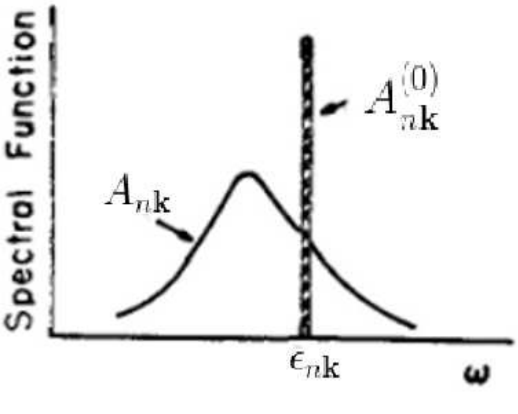

Figure 4.2: The unperturbed SF $A^{(0)}_{n\mathbf{k}}$ is represented by a delta function, while the interacting spectral function $A_{n\mathbf{k}}$ has often a finite width.

The SF $A_{n\mathbf{k}}$ is a probability function. It gives the probability to find an electron in the state labeled by band index n and momentum $\mathbf{k}$ with energy ω. Since the total integrated area under the entire spectra is 1,

$$\int_{-\infty}^{\infty} \frac{d\omega}{2\pi} A_{n\mathbf{k}}(\omega) = 1, \tag{4.6}$$

the existence of any area where $\Im\Sigma \neq 0$ (the crosshatched one in Fig. 4.1), implies that the renormalization factor $Z_{n\mathbf{k}}$ is less than unity. This is a further proof of the physical meaning of the $Z_{n\mathbf{k}}$ factors as electronic charge.

In the following section I will investigate the electronic properties of polymers when the electron-phonon interaction is introduced. I will show that the spectral functions I obtained do hardly fit into the quasi particle picture that, instead, appears to be totally inappropriate.

4.2 Breakdown of the quasiparticle picture

In strongly correlated materials the small renormalization factors $Z_{n\mathbf{k}}$ point to the creation of non qp-like excitations (like the Hubbard bands, for example). In the present case the situation is even more puzzling. The renormalization factors are non physical. As already pointed out previously, I linked this effect to the presence of intense self-energy poles close to $\epsilon_{n\mathbf{k}}$.

The electronic spectral function provides the most direct way to test the quasiparticle concept. I restrict the analysis to the $T = 0\,K$ case, following the procedure outlined in the previous section to calculate the spectral functions. In order to do that I generated 100 unidimensional (along $\hat{x}$ direction) random $\mathbf{q}$ points to better perform the sum over phonons $\mathbf{q}\lambda$, in Eq. (3.45). For each $\mathbf{q}$ point phonons and electron-phonon matrix elements are calculated, using the electronic density of a $60{\times}1{\times}1$ $\mathbf{k}$-point grid, and 45 empty bands.

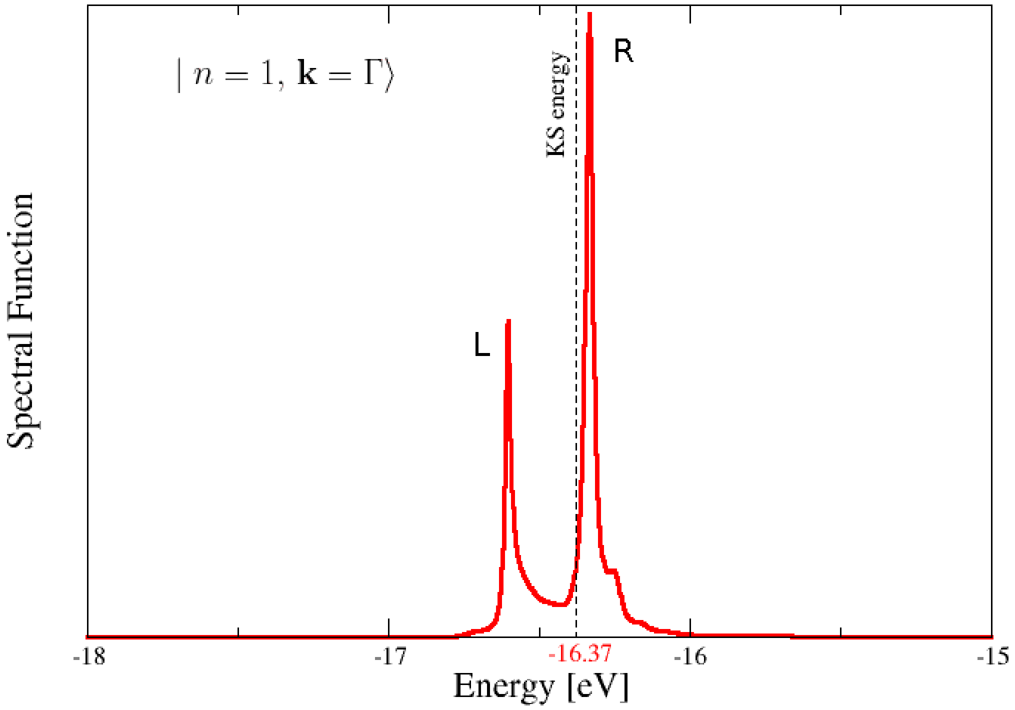

Figure 4.3: *Trans*-polyacetylene. Spectral function corresponding to the state $| n = 1, \mathbf{k} = \Gamma\rangle$. The position of the KS energy is indicated by the black dashed line.

In Fig. 4.3 the spectral function of the state $\mid n = 1, \mathbf{k} = \Gamma\rangle$ is depicted which, calculated at $T = 0\,K$, covers an energy range of about $0.8\,eV$. This is clearly a first evidence for the failure of the QP concept. Indeed, two distinct peaks appear: at -16.6 and $-16.32\,eV$. The existence of two peaks implies that the QP picture fails, because the condition of only one pole collecting most of the weight is not satisfied. It is worth to remind that this event occurs under the only effect of the zero point motion. I will discuss more deeply the physical interpretation in the next section. From a general point of view, however, the appearance of more than one peak in the spectral function can be further discussed.

First of all, the KS bare energy, $-16.37\,eV$, splits and moves aside of $0.05\,eV$ forming the peak R and of $-0.23\,eV$ for the peak L. As $\mid n = 1, \mathbf{k} = \Gamma\rangle$ is originally *one* electronic state, two peaks can not be two distinct QPs because, it would mean to associate to each peak one electron. Instead the formation of two peaks implies to consider an extended Fock space, composed of electrons and phonons. The breakdown of the quasiparticle picture is linked to the fact that the electron takes part in strong real transitions being its energy close to the poles of the self-energy. These scatterings send the bare electron into more than one of the mixed states of the extended Fock space (EFS). The stronger these scatterings are the more dressed the electron will be. As a consequence the electronic charge, $Z_{n\mathbf{k}}$, looses its physical meaning.

The many-body framework does not provide the tools to add further information about the composition of the “new” mixed states. The appropriate framework will be built in the next section.

On the other hand an analysis of the most important phonon branches that contribute to the spectral function can be carried out selecting the contribution coming from the optical phonons, divided into two groups: the O_1 branches (from the 5^{th} to the 10^{th}) and the O_2 branches (from the 11^{th} to the 12^{th}), as shown in Fig. 2.6. From Fig. 4.4 I assert that the optical branches O_1 mainly cause the breakdown of the quasiparticle picture, while if only the scatterings with the optical branches were considered they would renormalize the electron energy. However, in both cases, I cannot explain the additional structures in the spectral functions as due to phonon excitations only. Indeed the distance between the bare energy and each of two peak does not correspond to any phonon frequency. For example the peak R is at $0.05\,eV$ from the bare energy. It corresponds to about $400\,cm^{-1}$, the typical energies of acoustic phonons. As I discarded the contribution coming from the acoustic phonons as I discussed in Sec. 2.4, the new state builds up from a

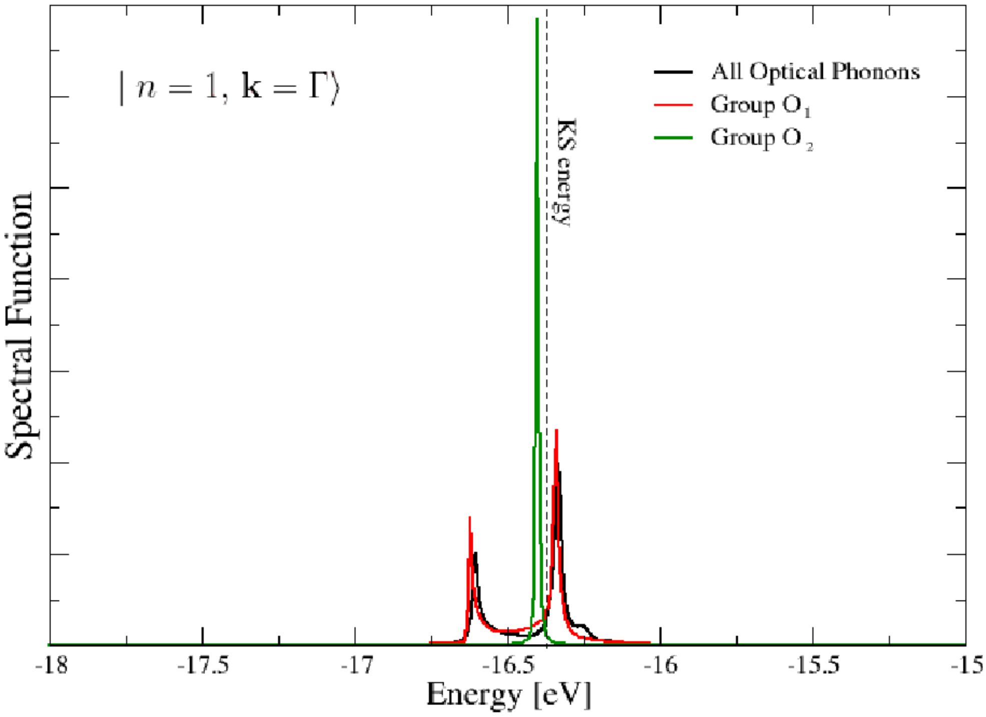

Figure 4.4: *Trans*-polyacetylene. Contributions of two groups of optical phonons to the spectral function of state $| n = 1, \mathbf{k} = \Gamma \rangle$.

particular combination of electrons and optical phonons. The same can be said for the peak L. It moves aside in fact, of $-0.23\, eV$ which is equivalent to $1850\, cm^{-1}$. However it does not correspond to any phonon frequency, as confirmed by Fig. 2.6.

The peculiar shape of the spectral function depicted in Fig. 4.3 is not a fortuitous case. It is instead a general trend both in *trans*-polyacetylene and in polyethylene. This is reasonable because both polymers have phonon frequencies of the same order of magnitude of the electronic ones. The spectral functions for *trans*-polyacetylene and polyethylene are largely structured in some cases. It means that Eq. (4.3) has more than one solution and, as a consequence, the Green's function has more than one pole.

In Figs. 4.5 and 4.7 the KS band structure and a sample of spectral functions are depicted, for *trans*-polyacetylene and polyethylene respectively. One of the most striking aspect is the energy range spanned by the spectral functions, which is even $3\, eV$ in some cases, like the 5^{th} band of polyethylene shown in green in Fig. 4.7. Another crucial aspect is that some spectral functions overlap, like the 3^{rd}, the 4^{th} and the 5^{th} band in *trans*-polyacetylene. In this case it is impossible both to associate a single, well defined energy to the electron and to state which band it belongs to.

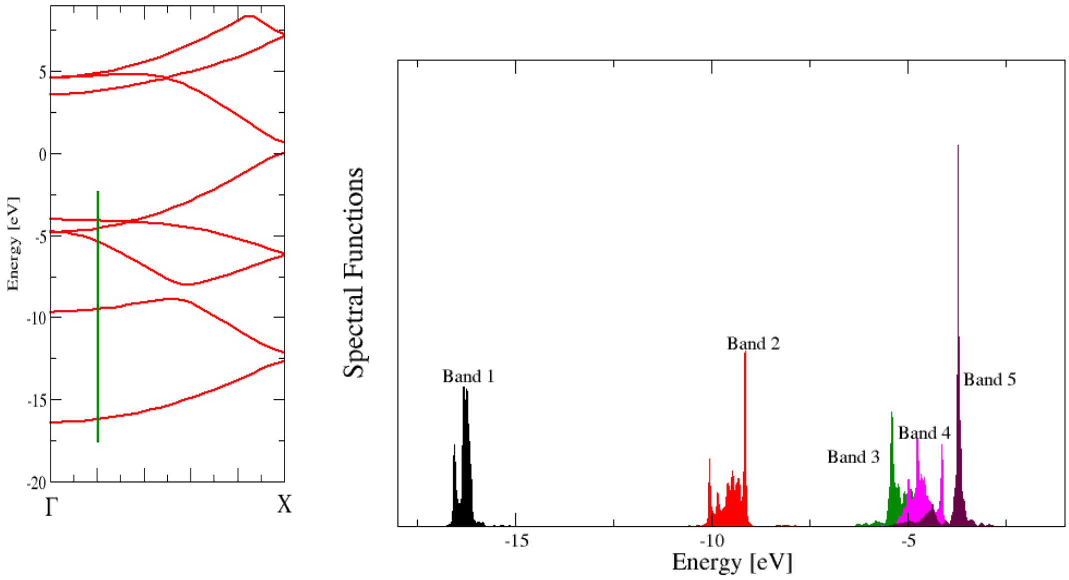

Figure 4.5: The electronic band structure (on the left) and the spectral functions of *trans*-polyacetylene calculated when the electron-phonon interaction is included (on the right). The green line in the left panel marks the energy range on which the corresponding SFs are shown.

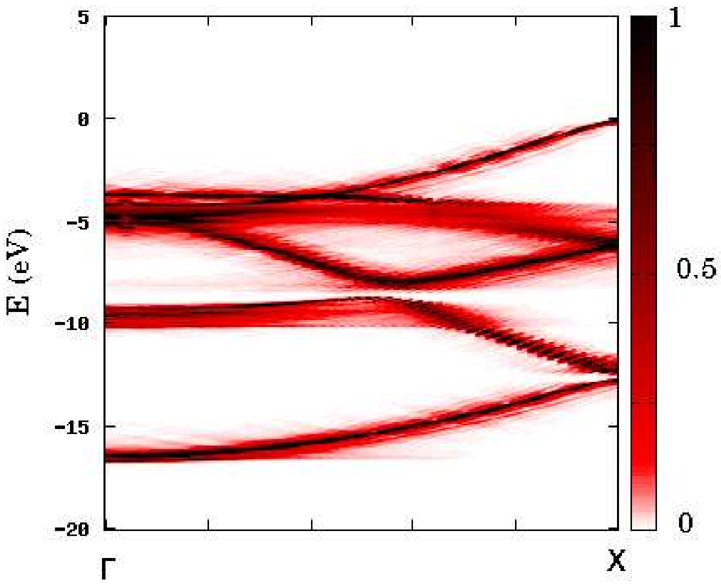

Figure 4.6: *Trans*-polyacetylene. Bidimensional representation of the probability amplitude. The intensities of peaks are associated to a coloured scale, from white to black. The solid black lines are the KS valence bands.

Interpreting the residue of each pole as the probability to find the electron in the relative state, it is possible to make a bidimensional representation of the probability amplitude.

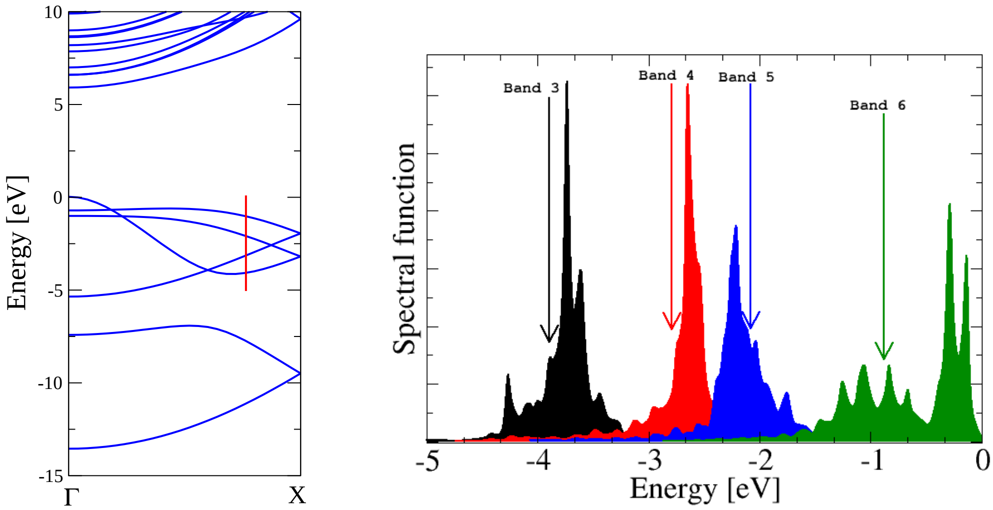

Figure 4.7: The electronic band structure (on the left) and the spectral functions of polyethylene calculated when the electron-phonon interaction is included (on the right). The red line in the left panel marks the energy range on which the corresponding SFs are shown.

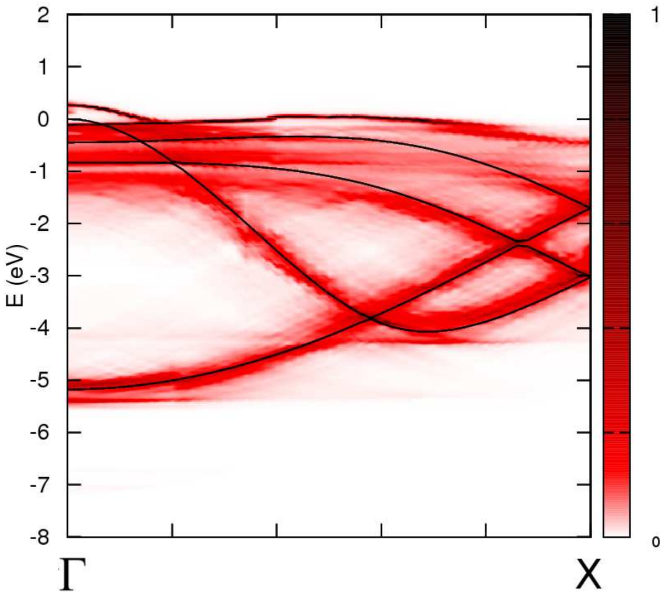

Figure 4.8: Polyethylene. Bidimensional representation of the probability amplitude. The intensities of peaks are associated to a coloured scale, from white to black. The solid black lines are the KS valence bands.

In Figs. 4.6 and 4.8 to the probability is associated a value from 0 to 1 on a coloured scale, from white (the less intense peak), to black (the most intense one). Moreover the KS electronic bands are also drawn as a reference of the electronic band structure before switching on the electron-phonon interaction. These pictures gather all the information about the energy range covered by the spectral functions and the intensity of all peaks. In Fig. 4.6 it is clearly shown that the spectral functions I plotted in Fig. 4.7 for polyethylene, overlap near the edge of the Brillouin Zone. In

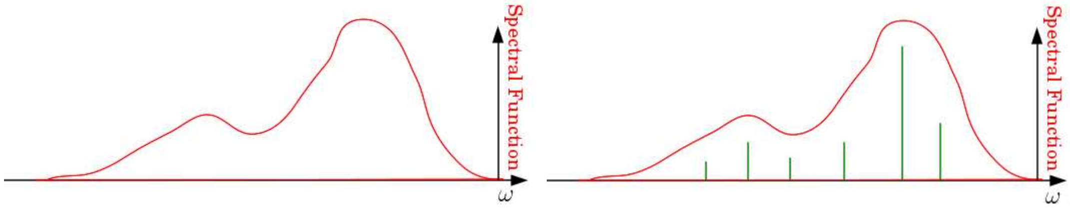

Figure 4.9: A simplified picture of the different way to calculate the spectral function: the many-body approach (left panel) and an expansion of the system eigenstates (right panel). In the second case the different structures are interpreted as polaronic states $\mid I\mathbf{k}\rangle$.

particular I observe that the 5^{th} band of polyethylene moves up close to Γ-point and then the electron completely disappears. In general I observe that each band has a different energy width which evolves in different manners moving from Γ to X.

The overall conclusion that can be drawn from the previous discussion is that electrons cannot be assimilated to quasiparticles, i.e. electrons are strongly dressed by the scattering with phonons. The SFs shown in Figs. 4.5 and 4.7 are clearly not assimilable to QP spectral functions because of the existence of a multiplicity of poles. They are the poles of the Green's function, solutions of Eq. (4.3), each one convoluted with a Lorentzian broadening. As a consequence the frequency dependence of the self-energy, includes all the information concerning the main structures of the spectral functions (left panel of Fig. 4.9).

The spectral function can be re-written as an expansion in the eigenstates $\mid I\mathbf{k}\rangle$ of the system

$$A_{n\mathbf{k}}(\omega) = \sum_{I\mathbf{k}} \mid \langle \Psi_0 \mid c^{\dagger}_{n\mathbf{k}} \mid I\mathbf{k}\rangle \mid^2 \frac{\Gamma_{I\mathbf{k}}}{(\omega - E_{I\mathbf{k}})^2 + \Gamma^2_{I\mathbf{k}}}, \tag{4.7}$$

where $\mid I\mathbf{k}\rangle$, eigenstate of the electron-phonon Hamiltonian, is an element of the EFS. In this way the shape of the spectral function is reproduced by weighting each eigenvalue of the mixed system by a Lorentzian broadening. In particular to each structure appearing in the spectral functions calculated within the many-body approach, is associated a precise state $\mid I\mathbf{k}\rangle$ (right panel of Fig. 4.9). Therefore the origin of the multiple poles in the spectral functions shown in Figs. 4.5 and 4.7 is connected to the existence of more than one intense state $\mid I\mathbf{k}\rangle$ belonging to the same state $\mid n\mathbf{k}\rangle$.

Unfortunately the many-body approach suffers of some limitations: the eigenstates of the system are not known. For this reason in the next section I will re-map the structures of the Many-Body spectral functions to the solution of an eigenvalue problem in the electron-phonon EFS. The eigenstates of the system will give interesting information about the mixed electronic/phononic character of the polaronic states.

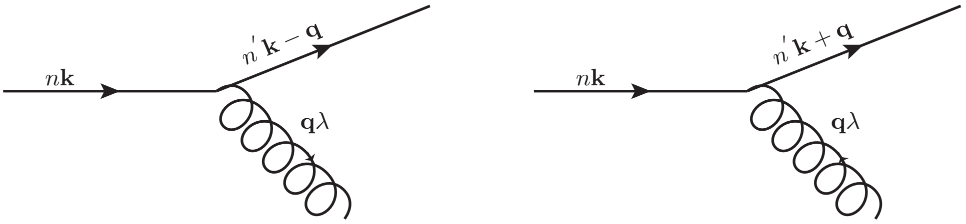

Figure 4.10: Phonon emission (on the left) and absorption (on the right) scattering events.

4.3 Multiplicity of the polaronic states: an Hamiltonian representation

In the previous section I supposed that the existence of more than one mixed electron-phonon state $\mid I\mathbf{k}\rangle$ projecting on the state $\mid n\mathbf{k}\rangle$, causes the appearance of several structures in the spectral function. In order to verify this assertion, I map the Many-Body spectral functions into the solution of an eigenvalue problem.

The basic Hamiltonian of the mixed electrons/phonons system is assumed to have the form

$$\hat{H} = \hat{H}_e + \hat{H}_p + \hat{H}_{ep}. \tag{4.8}$$

The first term is the electronic Hamiltonian H_e, already outlined in Chap. 1. The second term is the atomic Hamiltonian and the third one is the electron-phonon interaction Hamiltonian, which, written in the second quantization, read

$$\hat{H}_p = \sum_{\mathbf{q},\lambda} \omega_{\mathbf{q}\lambda}(b^{\dagger}_{\mathbf{q}\lambda} b_{\mathbf{q}\lambda} + \frac{1}{2}), \tag{4.9}$$

$$\hat{H}_{ep} = \frac{1}{N_{\mathbf{q}}} \sum_{\substack{n,n',\mathbf{k},\\ \mathbf{q},\lambda}} g^{\mathbf{q},\lambda}_{n'n\mathbf{k}} c^{\dagger}_{n'\mathbf{k}+\mathbf{q}} c_{n\mathbf{k}} (b^{\dagger}_{-\mathbf{q}\lambda} + b_{\mathbf{q}\lambda}), \tag{4.10}$$

where $c^{\dagger}_{n'\mathbf{k}+\mathbf{q}}$ and $c_{n\mathbf{k}}$ are the creation and the annihilation operators for the electrons with energies $\epsilon_{n'\mathbf{k}+\mathbf{q}}$ and $\epsilon_{n\mathbf{k}}$ in bands n' and n with wavevectors $\mathbf{k}+\mathbf{q}$ and $\mathbf{k}$, respectively. $b^{\dagger}_{\mathbf{q}\lambda}$ and $b_{\mathbf{q}\lambda}$ are the creation and annihilation operators for phonons with energy $\omega_{\mathbf{q}\lambda}$ and wavevector $\mathbf{q}$; the matrix element $g^{\mathbf{q},\lambda}_{n'n\mathbf{k}}$ describes the electron-phonon coupling, defined in Chap. 3. Both the interaction terms are included: the absorption and the emission of one phonon, as illustrated in Fig. 4.10.

The matrix elements must be written in an appropriate basis composed of independent electronic and phononic states. This basis must be chosen in order to make this approach equivalent to the many-body one. As outlined in Sec. 3.3.1 in the GW approximation only one phonon is assumed to be virtually scattered. As a consequence at a given temperature, being $\mathcal{N}_{\mathbf{q}\lambda}$ the mean phonon occupation number, the complete basis set will be composed of the following elements

$$\mid n\mathbf{k}\rangle \mid \mathcal{N}_{\mathbf{q}\lambda}\rangle, \; \mid n\mathbf{k}-\mathbf{q}\rangle \mid \mathcal{N}_{\mathbf{q}\lambda} \pm 1\rangle. \tag{4.11}$$

At zero temperature the basis set is reduced to

$$\mid n\mathbf{k}\rangle \mid 0_{ph}\rangle, \; \mid n\mathbf{k}-\mathbf{q}\rangle \mid \{1_{\mathbf{q}\lambda}\}\rangle, \tag{4.12}$$

and it reflects the fact that at $T = 0\,K$ no phonons in the ground state exist. As a consequence phonons absorption is not admitted, and only one phonon can be created.

As matrix elements corresponding to electronic states with different $\mathbf{k}$ do not mix, the Hamiltonian is readily written in the form sketched in Fig. 4.11.

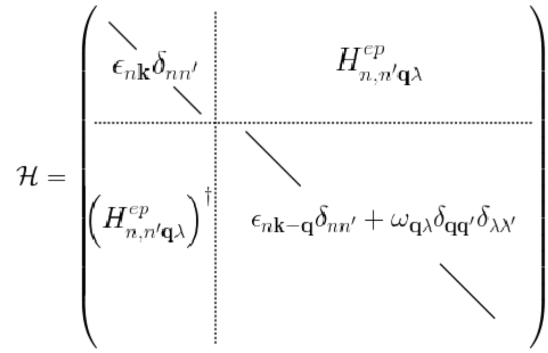

Figure 4.11: Electron-phonon Hamiltonian.

It can be verified that the Hamiltonian, shown in Fig. 4.11 is Hermitian, because H_{ep} is Hermitian. The dimension of the matrix, describing the system composed of electrons and phonons, is obtained by multiplying the number of electronic bands times the number of $\mathbf{q}$ vectors times the number of phononic branches, λ. This confirms the need, previously mentioned, to consider an extended Fock space to interpret the quasiparticle breakdown. As a consequence the number of eigenstates is larger than that of the electronic Hamiltonian. Before analyzing in detail the composition of the resulting eigenstates, I will first apply this procedure to a simple test model.

4.3.1 A test system

Let us consider two levels of energies $\epsilon_i = 0, E$ coupled to a phonon of energy ω_0 at $T = 0\,K$, as shown in Fig. 4.12.

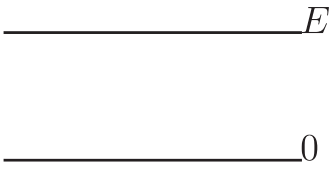

Figure 4.12: The two levels model used as a test case.

Eqs. (4.8-4.10) thus reduce to a simple expression for the Hamiltonian of this system

$$H = \sum_{i=1}^{2} \epsilon_i c_i^\dagger c_i + \omega_0 b_0^\dagger b_0 + \sum_{\substack{i=1,2 \\ j=1,2 \\ i\neq j}} g c_j^\dagger c_i (b_0^\dagger + b_0). \tag{4.13}$$

For the reason outlined in the previous section the scattering with only one phonon is considered and the basis set is

$$\mid 1\rangle \mid 0_{ph}\rangle, \mid 2\rangle \mid 0_{ph}\rangle, \tag{4.14}$$

$$\mid 1\rangle \mid 1_{ph}\rangle, \mid 2\rangle \mid 1_{ph}\rangle, \tag{4.15}$$

where by $\mid i\rangle$ I mean an electron in the level i^{th}. The dimension of the Hamiltonian matrix is then set by multiplying 2 bands × 1 **q** point × 1 phonon branch, resulting in a 4×4 matrix

$$\mathcal{H} = \begin{pmatrix} 0 & 0 & 0 & g \\ 0 & E & g & 0 \\ 0 & g & \omega_0 & 0 \\ g & 0 & 0 & E+\omega_0 \end{pmatrix}, \tag{4.16}$$

which can be diagonalized in two blocks, obtaining the following four energy levels

$$E_{1,2} = \frac{E+\omega_0 \pm \sqrt{(E+\omega_0)^2 + 4g^2}}{2}, \tag{4.17}$$

$$E_{3,4} = \frac{E+\omega_0 \pm \sqrt{(E-\omega_0)^2 + 4g^2}}{2}. \tag{4.18}$$

The corresponding four eigenvectors are

$$\mid I_1\rangle = \frac{1}{N_1}\left(\frac{g}{E_1}, 0, 0, 1\right), \tag{4.19}$$

$$\mid I_2\rangle = \frac{1}{N_2}\left(1, 0, 0, -\frac{g}{E_1}\right), \tag{4.20}$$

$$\mid I_3\rangle = \frac{1}{N_3}\left(0, 1, -\frac{g}{\omega_0 - E_3}, 0\right), \tag{4.21}$$

$$\mid I_4\rangle = \frac{1}{N_4}\left(0, \frac{g}{\omega_0 - E_3}, 1, 0\right), \tag{4.22}$$

where N_i are the normalization factors, $N_1 = N_2$ and $N_3 = N_4$.

These are the needed ingredients to calculate the Green's functions as matrix element of the resolvent

$$\mathcal{G}_i(\omega) = \langle vac \mid c_1 \frac{1}{\omega - H} c_1^+ \mid vac\rangle. \tag{4.23}$$

Expanding in eigenstates of the system, Eq. (4.23) becomes

$$\begin{aligned} \mathcal{G}_i(\omega) &= \sum_{j=1}^{4} \langle vac \mid c_i \frac{1}{\omega - H} \mid I_j\rangle\langle I_j \mid c_i^+ \mid vac\rangle \\ &= \sum_{j=1}^{4} \mid \langle vac \mid c_i \mid I_j\rangle \mid^2 \frac{1}{\omega - E_j}, \end{aligned} \tag{4.24}$$

where $\mid vac\rangle$ is the vacuum of phonons and electrons.

In order to show that the spectral functions calculated from Eq. (4.24) are analogous to the ones obtained in the MB approach, the Green's function for the 1^{st} state is evaluated from Eq. (4.24) as follows

$$\mathcal{G}_1(\omega) = \frac{1}{E_1 - E_2}\left[\frac{-E_2}{\omega - E_1} + \frac{E_1}{\omega - E_2}\right]. \tag{4.25}$$

On the other hand within the many-body approach Fan self-energy, Eq. (3.44), in this test case reduces to

$$\Sigma_1^{Fan}(\omega) = g^2\left[\frac{B(\omega_0) + 1 - f_2}{\omega - E - \omega_0 - i0^+} + \frac{B(\omega_0) + f_2}{\omega - E + \omega_0 - i0^+}\right]. \tag{4.26}$$

At zero temperature the Bose occupation factors vanish. The Fermi occupation factor f_2 in the Fan self-energy, Eq. (3.44) vanishes too, because the level is empty. Eq. (4.26) becomes

$$\mathcal{G}_1(\omega) = \frac{1}{\omega - g^2\left[\frac{1}{\omega - E - \omega_0}\right] - i0^+}. \tag{4.27}$$

The poles of Eq. (4.27) are $\omega = E_1$ and $\omega = E_2$, defined by Eq. (4.17). The residues evaluated at each pole are shown as follows

$$\begin{aligned} \omega = E_1 \qquad \mathrm{Res}_1 &= -\frac{E_2}{E_1 - E_2}, && (4.28) \\ \omega = E_2 \qquad \mathrm{Res}_2 &= \frac{E_1}{E_1 - E_2}. && (4.29) \end{aligned}$$

The final expression for $\mathcal{G}_1$ in the many-body approach is

$$\mathcal{G}_1(\omega) = \frac{1}{E_1 - E_2}\left[-\frac{E_2}{\omega - E_1 - i0^+} + \frac{E_1}{\omega - E_2 - i0^+}\right], \tag{4.30}$$

to be compared with Eq. (4.25). The Green's function $\mathcal{G}_1$, has components along the two mixed states $\mid I_1\rangle$ and $\mid I_2\rangle$ and the energy difference between the two poles is

$$E_1 - E_2 = \sqrt{(E + \omega_0)^2 + 4g^2}, \tag{4.31}$$

which is larger than $E + \omega_0$, that is the energy difference when $g \to 0$. When the electron-phonon interaction is strong, a high potential barrier must be overcome to create a scattering event. In order to do that a further amount of energy is needed. This implies that each additional structure can not be interpreted in energetic terms as simply an electron "plus" one phonon.

Even more complicated is the case when more than two electronic bands and than one phonon are considered. In Fig.4.13 the many-body and the Hamiltonian representation approaches are successfully compared when 8 electronic bands and all optical phonon branches are included. The two more intense peaks are $0.44\,eV$ far one each other, which is larger than the Debye frequency of this system. So the excitation of one phonon can not explain the additional structure.

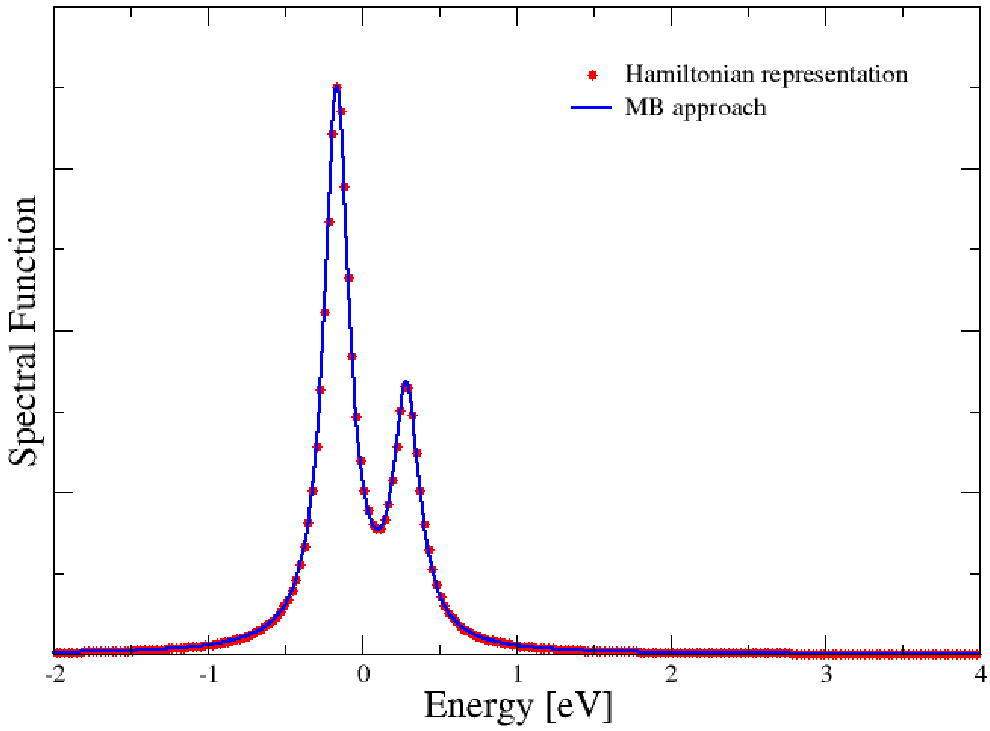

Figure 4.13: Spectral function $\mathcal{G}_1(\omega)$ of the level $\mid 1\rangle$ in a test system, calculated in two different manners: many-body in blue solid line and by diagonalization of the electron-phonon Hamiltonian in red dots.

4.3.2 The polaronic states

In order to better simulate a converged many-body spectral functions calculation, the Hamiltonian $\hat{H}$, shown in Fig. 4.11 is diagonalized including 30 electronic bands, 10 **q**-vectors and 12 phonon branches. The eigenvalue problem $\hat{H} \mid I_{\mathbf{k}}\rangle = E_{I_{\mathbf{k}}} \mid I_{\mathbf{k}}\rangle$ is satisfied by the following eigenstate

$$\mid I_{\mathbf{k}}\rangle = \sum_{n} A_{n\mathbf{k}} \mid n\mathbf{k}\rangle + \sum_{n'\mathbf{q}\lambda} B_{n'\mathbf{q}\lambda} \mid n'\mathbf{k}-\mathbf{q}\rangle \otimes \mid \mathbf{q}\lambda\rangle, \tag{4.32}$$

with energy $E_{I_{\mathbf{k}}}$. $\mid I_{\mathbf{k}}\rangle$ is a polaronic state with wavevector **k**, i.e. a packet made up of mixed electronic and phononic states. Since the Hamiltonian is written on a complete basis, the coefficients $A_{n\mathbf{k}}$ and $B_{n'\mathbf{q}\lambda}$ satisfy the following condition

$$\sum_{n} \mid A^{I}_{n\mathbf{k}} \mid^{2} + \sum_{n'\mathbf{q}\lambda} \mid B^{I}_{n'\mathbf{q}\lambda} \mid^{2} = 1, \tag{4.33}$$

and in general the eigenstates satisfy the following completeness relation

$$\langle J_{\mathbf{p}} \mid H \mid I_{\mathbf{k}}\rangle = \delta_{IJ}\delta_{\mathbf{kp}}. \tag{4.34}$$

Once the eigenstates $\mid I_{\mathbf{k}}\rangle$ and the eigenvalues $E_{I_{\mathbf{k}}}$ are known, the problem highlighted at the end of Sec. 4.2 is solved. The spectral function is calculated according to Eq. (4.7) and all the more intense peaks appearing in the spectral functions of state $\mid n\mathbf{k}\rangle$, are unambiguously labeled with a particular $\mid I_{\mathbf{k}}\rangle$ state, having $\mid n\mathbf{k}\rangle$ as the pure electronic component.

The Hamiltonian representation has the advantage to provide useful information on the composition of the polaronic states. Let us consider the $\mid n = 4, \mathbf{k} = 0.2(\frac{2\pi}{a}, 0, 0)\rangle$ state as an example. In Fig. 4.14 it is shown the corresponding spectral function.

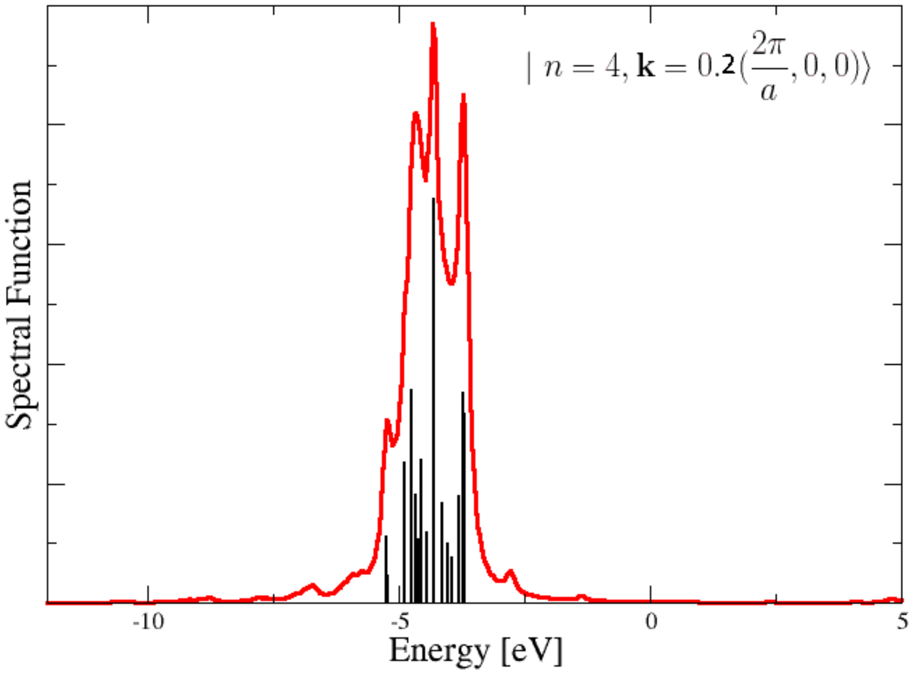

Figure 4.14: *Trans*-polyacetylene. Decomposition of the spectral function in polaronic states.

The poles and the corresponding residuals, indicated in Fig. 4.14 by bars with different heights, are summarized in Tab. 4.1.

Decomposition of the spectral function			
Pole (eV)	Residual:$\mid A_{n\mathbf{k}} \mid^2$	Pole (eV)	Residual:$\mid A_{n\mathbf{k}} \mid^2$
-5.25	$0.27\ 10^{-1}$	-4.42	$0.29\ 10^{-1}$
-5.21	$0.11\ 10^{-1}$	-4.30	0.17
-4.88	$0.58\ 10^{-1}$	-4.13	$0.41\ 10^{-1}$
-4.73	$0.89\ 10^{-1}$	-4.02	$0.24\ 10^{-1}$
-4.65	$0.45\ 10^{-1}$	-3.94	$0.18\ 10^{-1}$
-4.63	$0.15\ 10^{-1}$	-3.78	$0.44\ 10^{-1}$
-4.60	$0.26\ 10^{-1}$	-3.72	$0.87\ 10^{-1}$
-4.54	$0.59\ 10^{-1}$	-3.68	$0.78\ 10^{-1}$

Table 4.1: Poles and residuals for the spectral function of $| n=4, \mathbf{k}=0.2(\frac{2\pi}{a},0,0)\rangle$ state.

$\mid A^I_{n\mathbf{k}} \mid^2$ is the probability to find the polaronic state in the pure electronic $\mid n\mathbf{k}\rangle$ state. This reminds the physical meaning of the $Z_{n\mathbf{k}}$ factors, but in this contest the residual $\mid A^I_{n\mathbf{k}} \mid^2$ can not be assimilated to the electronic charge. From Tab. 4.1 it is in fact evident that the electron originally in the state $\mid n\mathbf{k}\rangle$ is spread over a multiplicity of states, each having a fictitious $Z_{n\mathbf{k}}$ factor less than 0.2. It means that in each polaronic state, defined by Eq. (4.32), the mixed electron-phonon contribution weights the most.

Decomposition of the spectral function

Pole (eV)	$\mathbf{q}$	λ	Residual: $\sum_{n'\mathbf{q}\lambda} \mid B_{n'\mathbf{k}-\mathbf{q}} \mid^2$
-5.25	3	$7, 9, 10$	0.89
	7	$7, 10$	
-5.21	$3, 7$	$9, 10$	0.88
-4.88	4	11	0.84
	8	12	
-4.73	5	$4, 6$	0.64
-4.65	5	$6, 7, 9, 10$	0.86
-4.63	5	$7, 9, 10$	0.92
-4.60	5	$7, 9, 10$	0.79
-4.54	$2, 10$	4	0.78
	$3, 7$	6	
	5	10	
-4.42	2	$7, 9$	0.78
	$3, 7$	6	
	5	11	
-4.30	2	$9, 11$	0.32
	9	4	
	10	9	
-4.13	2	11	0.60
	9	4	
-4.02	$1, 9$	10	0.65
	$5, 7$	4	
-3.94	3	$7, 9, 10$	0.79
	5	7	
	7	$9, 10$	
-3.78	$1, 9$	6	0.76
	$3, 7$	11	
-3.72	1	6	0.72
	$3, 5, 7$	11	
-3.68	5	11	0.70

Table 4.2: Poles, phonons and residuals of mixed electron-phonon states for the spectral function of $\mid n = 4, \mathbf{k} = 0.2(\frac{2\pi}{a}, 0, 0)\rangle$ state.

The smaller the $\mid A^{I}_{n\mathbf{k}} \mid^2$ is, the less the polaronic state can be assimilated to an electron. It is possible to isolate the most important phonon or phonons involved in the building up of the packet. They are summarized in Tab. 4.2.

$\mid B_{n'\mathbf{k-q}} \mid^2$ is the probability that the polaronic state is in the mixed electron–phonon $\mid n'\mathbf{k}-\mathbf{q}\rangle \otimes \mid \mathbf{q}\lambda\rangle$ state. Tab. 4.2 shows the sum of $\mid B_{n'\mathbf{k-q}} \mid^2$ over all the most important phonons for each pole. By comparing Tabs. 4.1 and 4.2 it can be verified that, for each pole, the sum of residuals is equal to 1. From an analysis of Tab. 4.2 it can be inferred that between the two groups of phonon branches, O_1 is mainly involved. This is confirmed for the $\mid n = 1, \mathbf{k} = \Gamma\rangle$ state in Fig. 4.15.

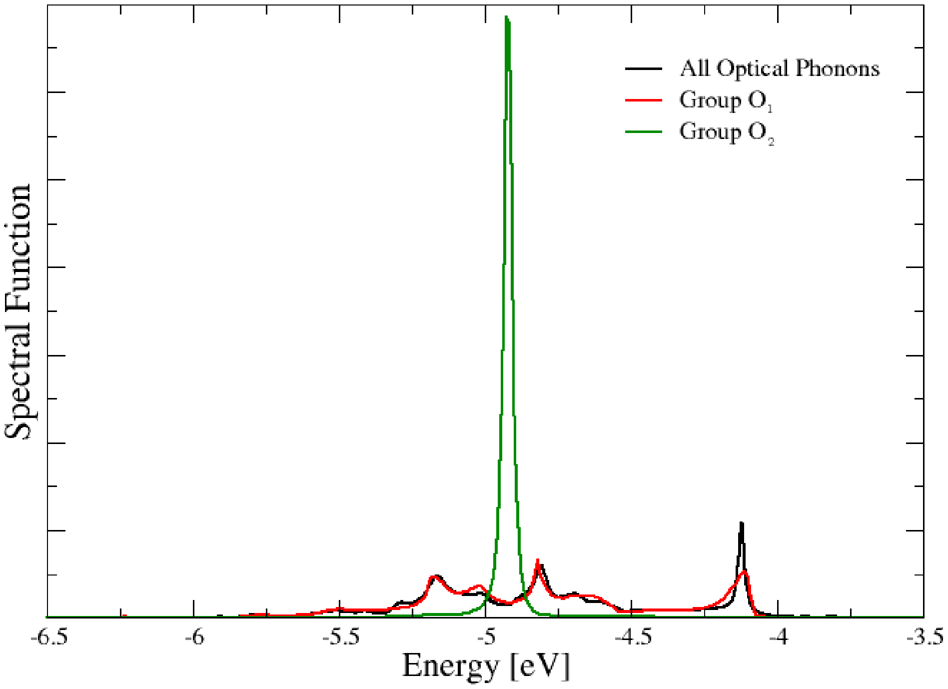

Figure 4.15: *Trans*-polyacetylene. Contribution of two groups of optical phonons to the spectral function of state $\mid n = 4, \mathbf{k} = 0.2(\frac{2\pi}{a}, 0, 0)\rangle$.

The small $Z_{n\mathbf{k}}$ factors outlined for the $\mid n = 4, \mathbf{k} = 0.2(\frac{2\pi}{a}, 0, 0)\rangle$ state actually represents a general trend. In Fig. 4.16 the projection $\mid \langle I_{\mathbf{k}} \mid n\mathbf{k}\rangle \mid^2 = \mid A_{n\mathbf{k}} \mid^2$ is plotted as a function of the polaronic eigenvalues. Only few polaronic states have $Z_{n\mathbf{k}} \simeq 1$. Most of all are below 0.5, instead. It means that the mixed electron-phonon part of the eigenstate, shown in Eq. (4.32), plays a dominant role.

To better characterize the polaronic states with a small electronic charge, further

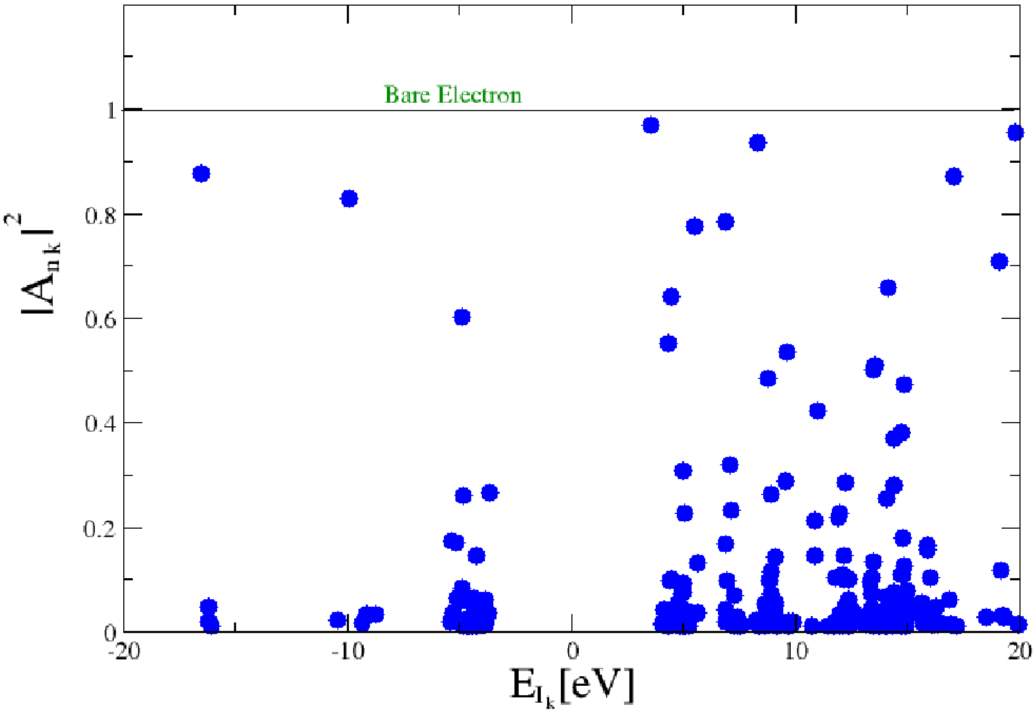

Figure 4.16: *Trans*-polyacetylene. The electronic charge $Z_{n\mathbf{k}}$ calculated as projection of the polaronic state over the pure electronic state, $|A_{n\mathbf{k}}|^2$. The bare electron charge is marked as limit value.

information must be extracted. In principle the mean value of any observable can be evaluated. For example the matrix elements of the atomic indetermination operator can be calculated as follows

$$\begin{aligned}\langle J_k \mid u^2_{\alpha,I,s} \mid I_k\rangle &= \sum_n \mid A^I_{n\mathbf{k}} \mid^2 \sum_{\mathbf{q}\lambda} \left(\frac{1}{2N_{\mathbf{q}}\omega_{\mathbf{q}\lambda}}\right) \epsilon_\alpha\left(\mathbf{q}\lambda/s\right) \epsilon^*_\alpha\left(\mathbf{q}\lambda/s\right) + \\ &+ 3\sum_{n'\mathbf{q}\lambda} \mid B^I_{n'\mathbf{q}\lambda} \mid^2 \left(\frac{1}{2N_{\mathbf{q}}\omega_{\mathbf{q}\lambda}}\right) \epsilon_\alpha\left(\mathbf{q}\lambda/s\right) \epsilon^*_\alpha\left(\mathbf{q}\lambda/s\right). \qquad (4.35)\end{aligned}$$

The values for the C and H species, calculated by Eq. (4.35), are shown in Tab. 4.3.

Trans-polyacetylene	C $a.u.$	H $a.u.$
$\hat{x}$	0.18	0.55
$\hat{y}$	0.13	0.36
$\hat{z}$	0.11	0.56

Trans-polyacetylene	C $a.u.$	H $a.u.$
$\hat{x}$	0.1	0.32
$\hat{y}$	0.07	0.21
$\hat{z}$	0.07	0.34

Table 4.3: Atomic amplitudes obtained by evaluating the matrix elements of operator $u^2_{\alpha,I,s}$: bare values (right table) and with the electron-phonon interaction (left table).

These values point to the fact that the atoms acquire an indetermination larger along the $\hat{x}$ direction, analogously to what I discussed in Sec. 2.5.

Even more interesting is to investigate the effect of the electron-phonon interaction on the final polaronic wavefunction $\Psi_{I_{\mathbf{k}}}(\vec{r})$ if compared to the corresponding pure KS wavefunction:

$$| \langle \vec{r} \mid I_{\mathbf{k}} \rangle |^2 = | A_{n\mathbf{k}} |^2 | \langle \vec{r} \mid n\mathbf{k} \rangle |^2 + \sum_{n'\mathbf{q}} | B_{n'\mathbf{k}-\mathbf{q}} |^2 | \langle \vec{r} \mid n'\mathbf{k}-\mathbf{q} \rangle |^2 . \tag{4.36}$$

The sum appearing in Eq. (4.36) is evaluated keeping the most important phonons $\mathbf{q}\lambda$ shown in Tab. 4.2 and considering the corresponding electronic state $| n^{'}\mathbf{k}-\mathbf{q} \rangle$.

In Fig. 4.17 (A) the wavefunction of the bare state $| n = 4, \mathbf{k} = 0.2(\frac{2\pi}{a}, 0, 0) \rangle$ is shown. The electron is mainly localized along the $C - H$ bond. When the electron-phonon interaction is switched on the wavefunction changes. In Figs. 4.17 (B) and (C) the wavefunctions of two polaronic states with a small $| A_{n\mathbf{k}} |^2$ are plotted. The first corresponds to the pole $-5.25\, eV$ and the second to $-4.73\, eV$. In general the electron is mainly localized along the carbon backbone.

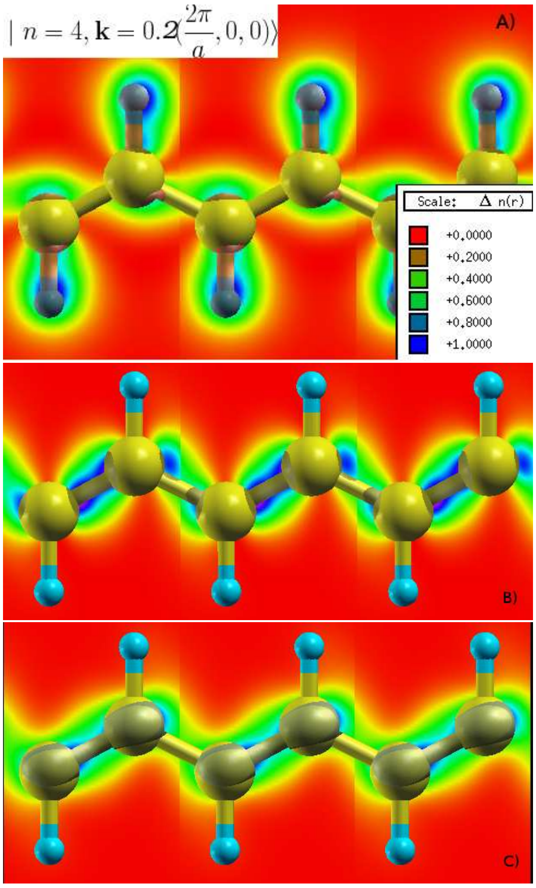

Figure 4.17: *Trans*-polyacetylene. A) Electronic density of the bare state $| n = 4, \mathbf{k} = 0.2(\frac{2\pi}{a}, 0, 0) \rangle$. B) and C) Polaronic wavefunction of two states which the bare state belongs to.

Combining the results concerning the atomic indetermination and the electronic wavefunctions of the two polaronic states shown in Figs. 4.17 (B) and (C), it can be concluded that electrons and phonons exert a cooperative effect on each other. The charge density changes, spreading all along the polymer, while the atoms squeeze along $\hat{y}$ and $\hat{z}$ directions, widening along $\hat{x}$. This cooperation can cause, for example, an enhancement of the mobility, opening therefore new perspectives for future investigations and applications of polymers.

4.4 Charge distributions and isotope effects

In the previous section I have analyzed the consequences of the electron-phonon interaction. Here I would like to investigate how it is possible to predict the breakdown of the quasiparticle picture starting from the bare electron charges and isotopic effects.

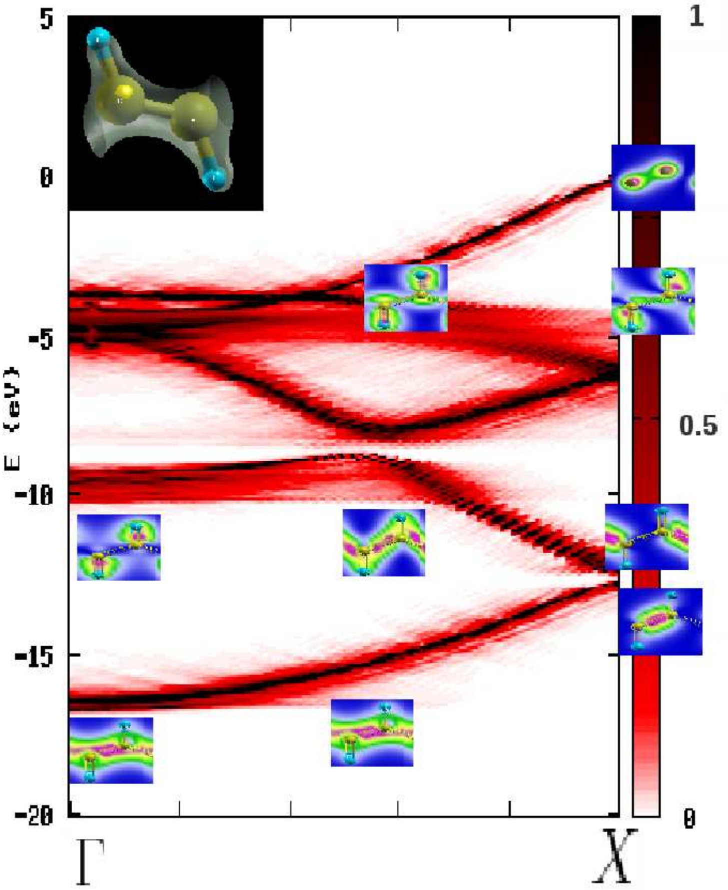

Figure 4.18: *Trans*-polyacetylene. Correspondence between the energy width of the spectral functions and the bare wavefunction of each electronic state.

The aim of Fig. 4.18 is to set a link between the energy range covered by the spectral functions and the KS wavefunctions. In each band, in fact, the spectral functions differently evolves from Γ to X, also depending on the evolution of the corresponding KS state, $\phi_{n\mathbf{k}} = \langle \vec{r} \mid n\mathbf{k} \rangle$.

I started by dividing the space surrounding the *trans*-polyacetylene monomer into four regions Ω_i, of which three are depicted in Fig. 4.19. They have been identified observing where the charge is localized mostly: along the double and the single carbon bond (1^{st} band), between the carbon-hydrogen bond (4^{th} band), over the carbons and perpendicular to the chain plane, where the polymer lies (π-orbitals belonging to the 5^{th} band). The last region is not shown in Fig. 4.19, because it is a bidimensional representation. Additional regions originated by the overlap of the previous ones have been taken into account to ensure that the total electronic charge is normalized to 1,

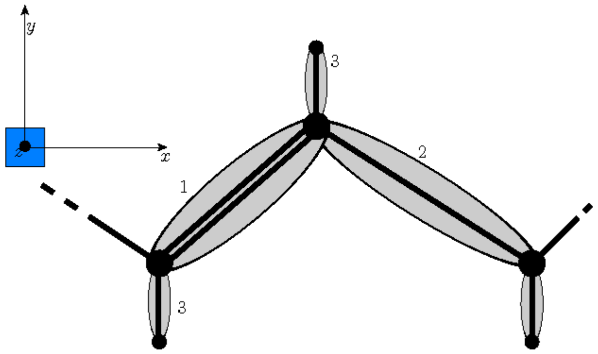

Figure 4.19: Projections on the xy plane of regions selected around the monomer, along the double bond (1), the single bond (2) and the CH bond (3).

$$\sum_{i=1}^{N} \int_{\Omega_i} \mid \phi_{n\mathbf{k}}(\vec{r}) \mid^2 d\mathbf{r} = 1. \tag{4.37}$$

In Fig. 4.20 (A) it is shown the charge density evolution along the 1^{st} band. The charge density in the three overlapping regions and that along the $C - H$ bond is constant and small. Close to Γ the charge density is initially equally distributed between the single and the double C bond. Moving towards X the 2^{nd} region is gradually depleted, filling the 1^{st} one. The electron is therefore mainly localized along the carbon backbone. It therefore experiences mostly the carbon zero point motion effect which is lower than the hydrogen one, as shown in Tab. 4.3.

It means a relative lower effect on the coupling with electrons which reflects on a reduced energy spread of the spectral functions as clearly highlighted in Fig. 4.20 (B). In this figure the spectral function evolution from Γ to X is shown. Close to the

Γ-point the spectral function shows two intense structures. Moving towards X the spectral function gets sharper, with the polaronic states turning into a quasiparticle.

As a consequence a clear correspondence between the charge distribution and the quasiparticle breakdown exists, if the different strength of double and single C bonds is taken into account. As a double bond is stiffer than a single one, the zero point motion effect of C atom is less effective, compared to the case where the charge is localized both on the single and the double bond.

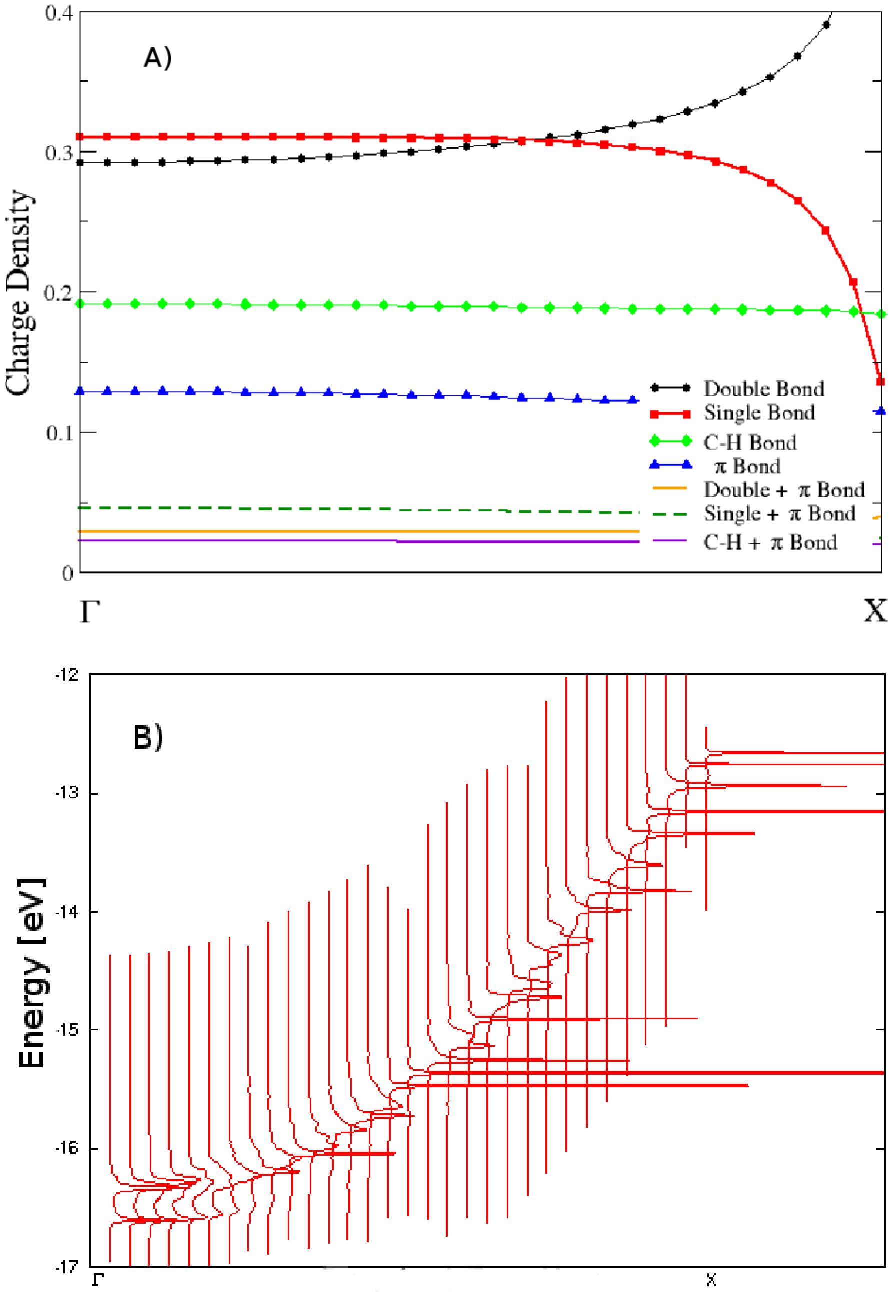

Figure 4.20: *Trans*-polyacetylene. Evolution of the charge distribution (top panel) and of the spectral functions (bottom panel) with the electronic states belonging to the 1^{st} band.

Different is the case for states belonging to the 4^{th} band and having the charge distributed on $C-H$ bonds. The spectral functions of this band are greatly structured, as showed in the previous section.

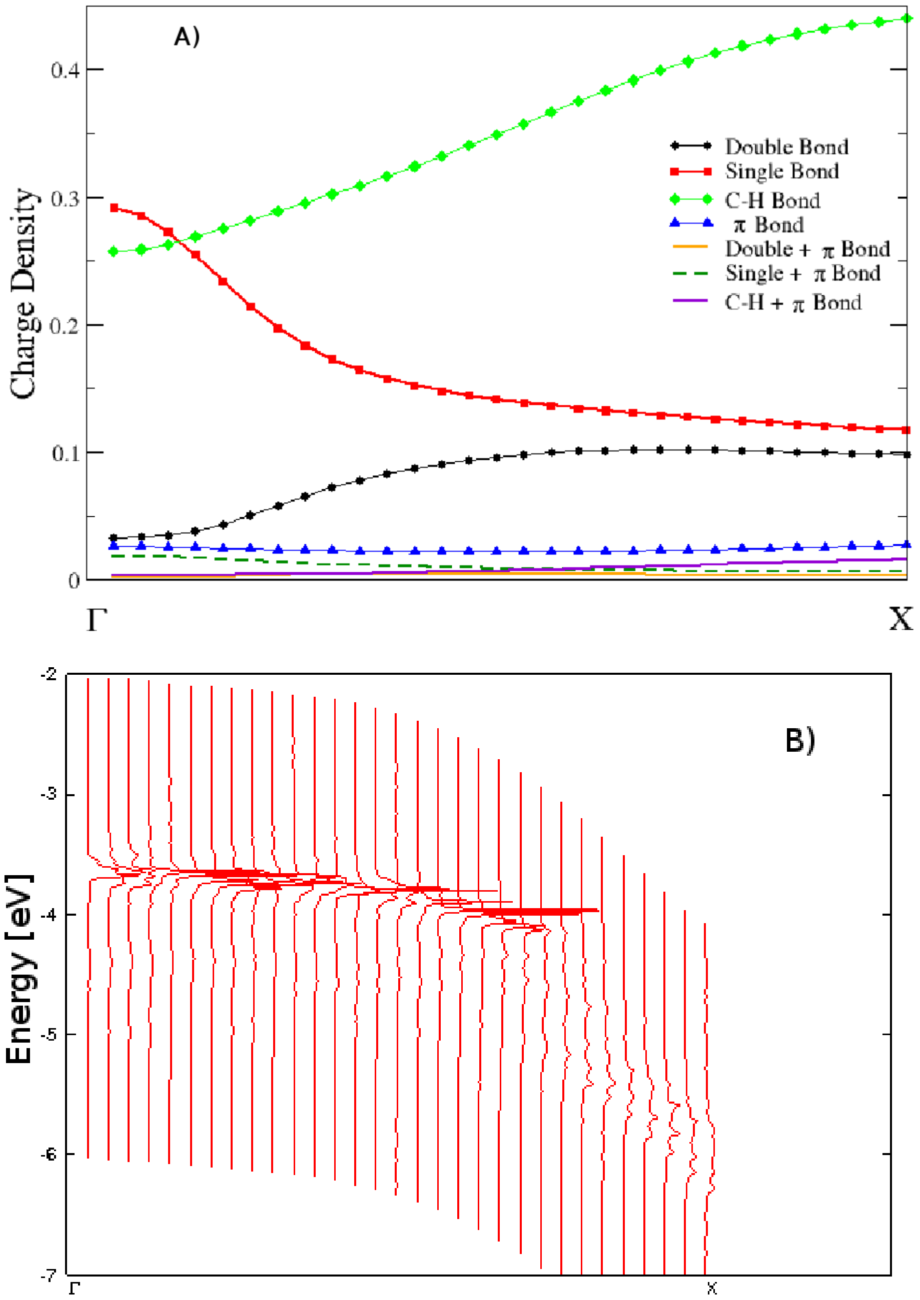

Figure 4.21: *Trans*-polyacetylene. Evolution of the charge distribution (top panel) and of the spectral functions (bottom panel) with the electronic states belonging to the 4^{th} band.

In Fig. 4.21 (A) it is illustrated the charge density evolution from Γ to X of the 4^{th} band. The charge distributed in the overlapping regions and belonging to the π-orbitals is constant and small. More generally the charge is more concentrated along the $C-H$ bond, leaving the 2^{nd} region lightly empty and partially filling the 1^{st} region. In this conditions the electron experiences the H zero point motion effect, which is larger than the C one. It causes the 4^{th} electronic band to completely disappear close to X. The spectral functions in fact evolve to strongly structured functions that cover a wide energy range.

The case of π orbitals is different. The electron is not affected by the zero point motion effect of the C atom, whose indetermination along the $\hat{z}$ direction is, in fact, the smallest one. Therefore in these states the electron behaves as a quasiparticle.

I also investigated the quasiparticle breakdown in terms of isotopic effects. The C and H atoms are replaced by equivalent atoms having an infinite mass. Such a strategy is equivalent to nullify the zero point motion effect and the consequent electron-phonon coupling at the zero temperature. In order to understand the role played by the two atomic species I used a uniform one dimensional grid of 10 $\mathbf{q}$ and the density optimized on a one dimensional $\mathbf{k}$ grid $10 \times 1 \times 1$ to calculate the phonons, while for the electron-phonon matrix elements I used 25 empty bands.

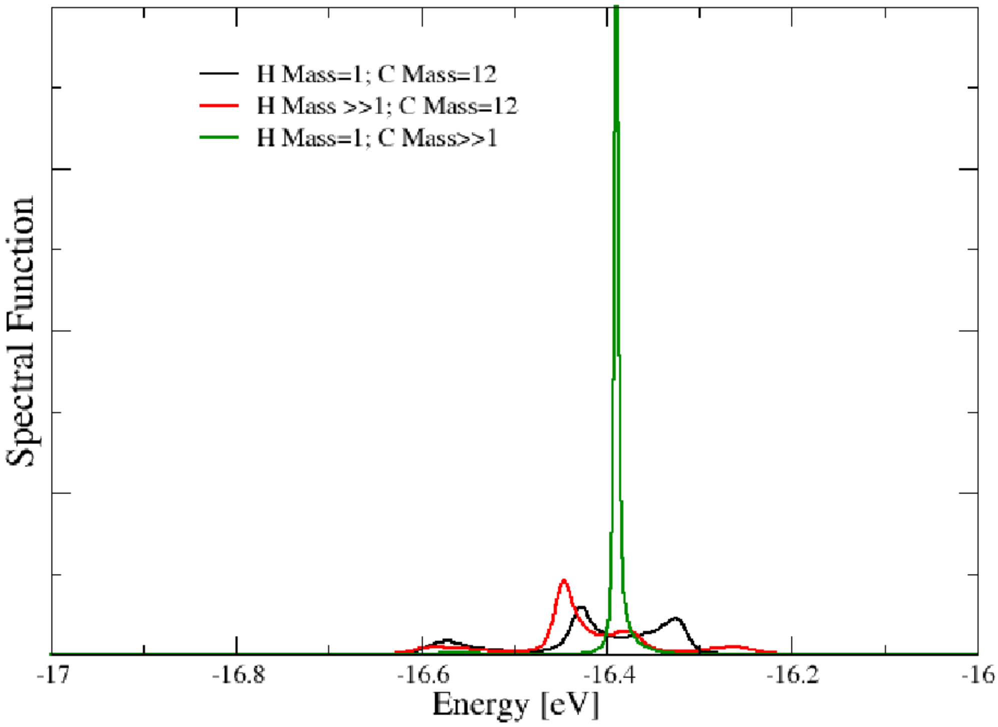

Figure 4.22: *Trans*-polyacetylene. Analysis of isotopic effects for state $| n = 1, \mathbf{k} = \Gamma\rangle$.

In Fig. 4.22 the spectral function for the $| n = 1, \mathbf{k} = \Gamma\rangle$ state is shown. When the carbon atom is replaced by a carbon with a huge mass, the only zero point motion effect of hydrogen renormalizes the electronic energy. While if the H atom is replaced by an hydrogen with a huge mass, the carbon zero point motion effect causes the breakdown of the quasiparticle picture. This analysis confirms what I showed before: the breakdown of the quasiparticle picture along the 1^{st} band, is carbon dictated. Indeed, the charge analysis showed that the charge density is localized along the carbon backbone.

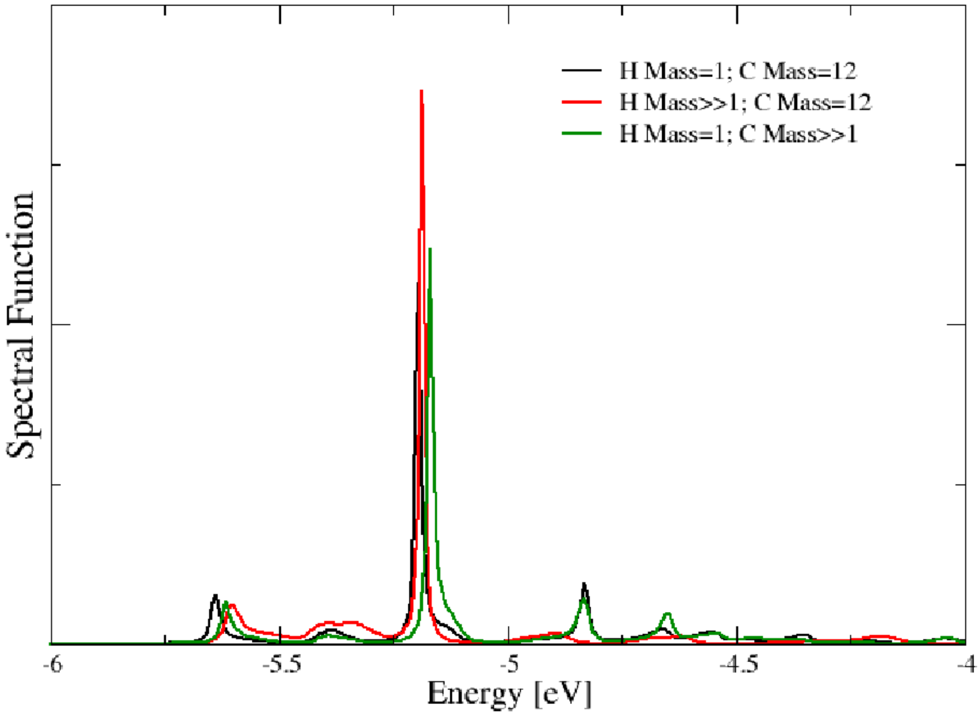

Figure 4.23: *Trans*-polyacetylene. Analysis of isotopic effects for state $\mid n=4, \mathbf{k}=0.4(\frac{2\pi}{a},0,0)\rangle$
.

In Fig. 4.23, instead, the spectral function for the $\mid n=1, \mathbf{k}=0.4(\frac{2\pi}{a},0,0)\rangle$ state is shown. Even this case confirms the previous analysis on the charge distribution. The quasiparticle breakdown of the 4^{th} band is both carbon and hydrogen dictated. Only replacing both atoms with equivalent atoms having huge masses, the spectral function reduces to a delta function centered at the bare energy of the considered electronic state.

In conclusion hydrogen alone is not able to cause the failure of the quasiparticle picture. quasiparticle breakdown in polymers is both Hydrogen and Carbon dictated.

Bibliography

[1] G.D. Mahan Many-Particle Physics (New York: Plenum) 1998

[2] R. D. Mattuck, *A guide to Feynman diagrams in the Many-Body problem*, McGraw-Hill, New York (1976)

Conclusions

The results presented in this thesis lead to a main conclusion: the frozen atoms approximation, commonly assumed in ab-initio calculations, is seriously broken in carbon based polymers.

This was already clear when I simulated the zero point motion effect by using a Gaussian random walker. Small atomic movements around the equilibrium positions produce great changes in the single particle electronic energies. The spectral function of each electronic level spreads over an energy range as large as $2\,eV$. Although this approach overestimates the zero point motion effect (atomic movements are chaotic and do not respect phonon symmetries) the link between the quantum fluctuations and the electronic levels is established.

To better investigate and confirm the strong electron-phonon coupling I performed an accurate study of the polaronic corrections in *trans*-polyacetylene and polyethylene within the HAC approach. Although it represents a well established approach, I readily realized that the HAC theory suffers of some limitations. The quasiparticle corrections, in fact, appear to be uncontrollably affected by serious numerical instabilities pointing to a complicate dependence on the energy of the self-energy.

I tried to cure the problem by releasing the adiabatic approximation on which the HAC approach is based. Nevertheless I showed that a straightforward application of the quasiparticle picture in the HAC approach leads to unphysical quasiparticle charges (the renormalization factors $Z_{n\mathbf{k}}$).

To trace back the motivations for the unphysical $Z_{n\mathbf{k}}$ factors to the frequency dependence of the electron-phonon self-energy I applied the quasiparticle concept within the more general many-body perturbation theory framework.

In this framework the unexpected oscillations of the $Z_{n\mathbf{k}}$ factors are ascribed to the closeness of the bare energy to the multiple and intense poles of the self-energy. This brought into question one of the basic condition of reliability of the quasiparticle picture. Indeed a structured self-energy near the bare energy can induce the electron to scatter with electrons and phonons. These real transitions represent the poles of the self-energy and can potentially lead to a complete dephasing of the electronic state.

Indeed the quasiparticle picture is definitely demonstrated to fail, when the spectral functions are analyzed. The first remarkable feature is that they span an energy range as large as $3\,eV$, confirming what was predicted by the Gaussian random walk analysis. Even if this represents the general trend, the analysis in terms of the Kohn–Sham orbitals reveals that the energy range is reduced if the charge is localized on the carbon backbone. On the contrary, the electron localized along the $C-H$ bond experiences a larger dephasing induced by the huge zero point motion effect of the hydrogen atom. Some spectral functions even overlap preventing to associate a single, well defined energy and a band index to the electrons. This is the breakdown of the band theory.

The second striking point is the multiple structures appearing at $T = 0\,K$. The formation of additional structures suggests to consider the electron-phonon interaction in an extended Fock space composed by electrons and phonons. By mapping the structures of the many-body spectral functions into the solution of an eigenvalue problem, I associated each structure to a particular polaronic state $\mid I_{\mathbf{k}}\rangle$.

Because of its non perturbative nature, each polaronic state represents a coherent packet of electron–phonon pairs. This coherence is clearly manifested by the cooperative dynamics of electrons and phonons participating in the polaronic packet, which results in a modified spatial distribution.

In the final polaronic wavefunction, in fact, electrons, originally localized on the $C-H$ bond, are spread along the polymer axis. Similarly atoms embodied in the polaronic state increase their spatial indetermination.

The resulting coupled electronic and atomic dynamics pave the way for new investigations in polymers and more in general in carbon based nanostructures. The cooperative dynamics of electrons and phonons in the polaronic states can have potential physical implications, as for example, an enhancement of the electronic mobility.

More generally the breakdown of the quasiparticle picture and of the band theory imposes a critical analysis of the previous results obtained using purely electronic theories.

Appendix

A.5 Statistical Mechanics in Occupation Number Formalism

The occupation number formalism is appropriate to deal with a system in which the particles number is not fixed. As a member of the *grand-canonical ensemble*, the system is immersed in a reservoir at T fixed, with which it exchanges particles and energy.

Let's suppose to know the Hamiltonian H and the state of the system $\mid \Psi_i\rangle$ that satisfies the equations:

$$H \mid \Psi_i\rangle = E_i \mid \Psi_i\rangle \text{ and } \sum_k c_k^\dagger c_k \mid \Psi_i\rangle = N_i \mid \Psi_i\rangle. \tag{A.38}$$

As N is not fixed, $\mid \Psi_i\rangle$ depends on N.

The probability that the system, as a member of an ensemble, is in the state $\mid \Psi_i\rangle$ with energy E_i and particle number N_i, is

$$\mathcal{P}_i = \frac{e^{-(\beta(E_i-\mu N_i))}}{\sum_i e^{-(\beta(E_i-\mu N_i))}} = \frac{\rho_i}{Z}, \tag{A.39}$$

where ρ_i is the *grand distribution function*, while Z is the *grand partition distribution.* Eq. (A.39) can also be written in terms of the *grand distribution operator* $\hat{\rho}$

$$\mathcal{P}_i = \frac{\langle\Psi_i \mid \hat{\rho} \mid \Psi_i\rangle}{\sum_i\langle\Psi_i \mid \hat{\rho} \mid \Psi_i\rangle}. \tag{A.40}$$

It's natural now to define the average value of any operator $\hat{\mathcal{O}}$ in the following way

$$\hat{\mathcal{O}} = \sum_i \langle\Psi_i \mid \hat{\mathcal{O}} \mid \Psi_i\rangle P_i = \frac{tr\hat{\mathcal{O}}\hat{\rho}}{tr\hat{\rho}}. \tag{A.41}$$

As the MB state vector $\mid \Psi_i\rangle$ is not known, Eq. (A.41) can be re-written using the property of the trace to be invariant under change of representation. The new basis is composed by the eigenstates of a non interacting system $\mid \Phi_i\rangle$

$$\hat{\mathcal{O}} = \frac{\sum_{i,p}\langle\Phi_i \mid \hat{\mathcal{O}} \mid \Phi_p\rangle\langle\Phi_p \mid \hat{\rho} \mid \Phi_i\rangle}{\sum_i\langle\Phi_i \mid \hat{\rho} \mid \Phi_i\rangle}. \tag{A.42}$$

Now we consider just a non-interacting system whose Hamiltonian and the state vector read

$$H_0 = \sum_k \epsilon_k c_k^\dagger c_k \quad \text{and} \quad \mid \Phi_i\rangle = \mid n_1^i, ..., n_k^i, ...\rangle \tag{A.43}$$

where n_k^i is the occupation number of the state k of the eigenstate $\mid \Phi_i\rangle$. The gran distribution function of the non interacting system is

$$\begin{aligned}
\rho_{i0} &= \langle\Phi_i \mid e^{-\beta(H-\mu N)} \mid \Phi_i\rangle \\
&= \langle n_1^i, ..., n_k^i, ... \mid e^{-\beta\sum_k(\epsilon_k-\mu)c_k^\dagger c_k} \mid n_1^i, ..., n_k^i, ...\rangle \\
&= \langle n_1^i, ..., n_k^i, ... \mid \prod_k e^{-\beta(\epsilon_k-\mu)c_k^\dagger c_k} \mid n_1^i, ..., n_k^i, ...\rangle \\
&= \prod_k e^{-\beta(\epsilon_k-\mu)n_k^i},
\end{aligned} \tag{A.44}$$

while the grand partition function may be written

$$\begin{aligned}
Z_0 = tr\rho_0 = \sum_i \rho_{i0} &= \sum_i\langle\Phi_i \mid \prod_k e^{-\beta(\epsilon_k-\mu)n_k^i} \mid \Phi_i\rangle \\
&= \sum_{n_1^i,...,n_k^i,...} \langle n_1^i, ..., n_k^i, ... \mid \prod_k e^{-\beta(\epsilon_k-\mu)n_k^i} \mid n_1^i, ..., n_k^i, ...\rangle \\
&= \sum_{n_1^i,...,n_k^i,...} \prod_k e^{-\beta(\epsilon_k-\mu)n_k^i} \\
&= 1 + e^{-\beta(\epsilon_1-\mu)} + e^{-\beta(\epsilon_2-\mu)} + ... + \\
&+ e^{-\beta(\epsilon_1-\mu)} \cdot e^{-\beta(\epsilon_2-\mu)} + ... \\
&= \prod_k \left[1 + e^{-\beta(\epsilon_k-\mu)}\right],
\end{aligned} \tag{A.45}$$

where we have used that $n_k = 0$ or 1.

Using Eqs. (A.44) and (A.45) it is possible to calculate the average value of operators for the non–interacting system. For example the occupation number in the state k of the non–interacting system can be easily calculated in this way

$$\begin{aligned}
\langle c_k^\dagger c_k \rangle_0 &= \sum_i \langle \Phi_i \mid c_k^\dagger c_k \prod_l e^{-\beta(\epsilon_l-\mu)n_l^i} \mid \Phi_i \rangle \\
&= \sum_{n_1^i,\ldots,n_k^i,\ldots} \langle n_1^i, \ldots, n_k^i, \ldots \mid c_k^\dagger c_k \mid n_1^i, \ldots, n_k^i, \ldots \rangle \cdot \prod_l \frac{e^{-\beta(\epsilon_l-\mu)n_l^i}}{1+e^{-\beta(\epsilon_l-\mu)}} \\
&= \frac{e^{-\beta(\epsilon_k-\mu)n_l^i}}{1+e^{-\beta(\epsilon_k-\mu)}} \cdot \underbrace{\sum_{\ldots,n_k^i,\ldots} \prod_{l\neq k} \frac{e^{-\beta(\epsilon_l-\mu)n_l^i}}{1+e^{-\beta(\epsilon_l-\mu)}}}_{1} \\
&= \frac{e^{-\beta(\epsilon_k-\mu)}}{1+e^{-\beta(\epsilon_k-\mu)}} \\
&= \frac{1}{e^{\beta(\epsilon_k-\mu)}+1}, \qquad \text{(A.46)}
\end{aligned}$$

where the only terms contributing to the sum are those for which

$$\langle \ldots, n_k^i, \ldots \mid c_k^\dagger c_k \mid \ldots, n_k^i, \ldots \rangle = 1 \;\; (\text{i.e. } n_k = 1). \qquad \text{(A.47)}$$

In conclusion we get the definition of the “hole” Fermi function distribution

$$\langle c_k^\dagger c_k \rangle_0 = f_k^-. \qquad \text{(A.48)}$$

The “particle” Fermi function distribution is as much as straightforward to obtain,

$$\begin{aligned}
\langle c_k c_k^\dagger \rangle_0 &= 1 - \langle c_k^\dagger c_k \rangle_0 \\
&= 1 - \frac{1}{e^{\beta(\epsilon_k-\mu)}+1} \\
&= \frac{1}{e^{-\beta(\epsilon_k-\mu)}+1} \\
&= f_k^+. \qquad \text{(A.49)}
\end{aligned}$$

The particle and the hole Fermi function distribution are shown in Fig. 24.

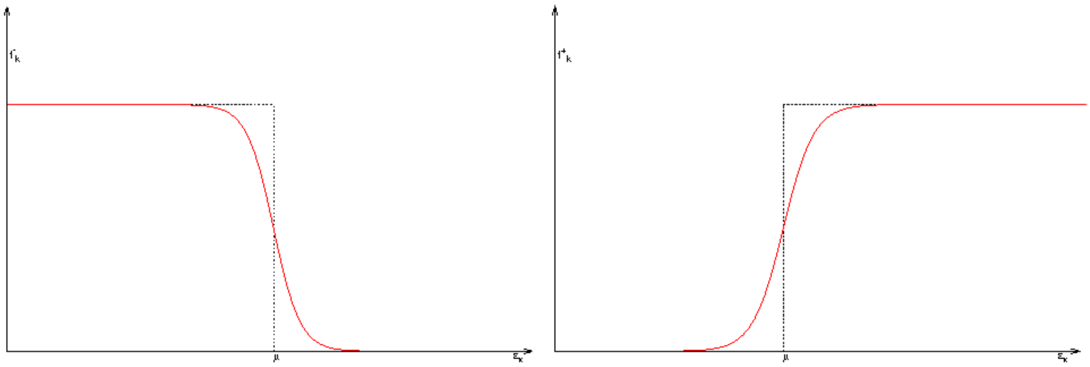

Figure 24: Statistical Factors for the particles (f^+) and holes (f^-).

Bibliography

[1] R. D. Mattuck, *A guide to Feynman diagrams in the Many-Body problem*, McGraw-Hill, New York (1976) p. 196-200.

Acknowledgements

Eccomi ad un altro grande traguardo.

Sono partita 3 anni fa potendo contare su un bagaglio di conoscenze, scientifiche e non, un po' più piccolo di adesso. Si é arricchito con il passare del tempo grazie a tante persone.

Andrea. Di te ammiro la tua esigenza, la precisione, l'ordine, la costanza, la determinazione e la pazienza. Ognuna di queste qualità, ha contribuito a rendere sempre proficuo il lavoro con te. Ti ringrazio per le volte che hai letto e poi riletto la tesi, permettendomi di andare sempre più a fondo nelle cose, e a cogliere ogni minimo dettaglio che mi é sfuggito. Ti ringrazio anche per i consigli che mi hai dato per ogni singola slide di ogni singolo seminario, per la pazienza con cui mi hai ascoltato ripetere tutti i seminari che ho fatto negli ultimi 5/6 mesi. I risultati naturalmente mi hanno dato una grande soddisfazione e spero di averne data altrettanta a te.

Rodolfo ed Olivia. Vi ringrazio invece per avermi permesso, a metà strada di cambiare rotta. Ringrazio Rodolfo inoltre per aver letto la mia tesi ed avermi dato ulteriori consigli.

Maurizia, Lucia, Elena. Ho condiviso tanti pranzi con voi, sono convinta già adesso che mi mancherete. Ricordo Elena e i suoi manicaretti succulenti, che brava!!! Lucia, ti ringrazio per le tante chiacchiere su film e libri, e per la pazienza con cui hai sopportato qualche sfuriata di troppo di alcune persone, magari per qualche nostra richiesta di rimborso. E Maurizia, ti ringrazio per la tua simpatia e la tua tenerezza con cui hai accompagnato le nostre pause caffè.

Adriano. Non hai mai fatto neanche un pranzo con noi!!! Mi ricorderò però perché spesso mi hai fatto sorridere con le tue idee di esperimenti sulle leggi del volo.

Margherita. Avremmo dovuto frequentarci di più. Ti ringrazio per la confidenza, e il sostegno psicologico. Ti auguro di trovare presto la tua strada.

Lungo questo cammino, si é affiancata una persona eccezionale, buona e molto curiosa, Claudio. Ho una frase che mi porto dentro e che riassume tutti i momenti che abbiamo condiviso in cui mi sono sentita travolta dalle infinite cose da imparare e capire: ”La conoscenza richiede tempo”. Ma per fortuna questi momenti sono solo una parte della storia. Quelli belli e di conoscenza personale riempiono e colorano le giornate.

La mia famiglia. Vi ringrazio perché ho vissuto ormai 30 anni della mia vita con voi.

Giulia. Ti ringrazio perché ci sei tu nella vita di mio fratello.

Pour finir, je remercie Xavier Blase pour avoir lu cette thèse.

A voi tutti, grazie.

Elena